UNIVERSIDADE DE LISBOA
FACULDADE DE CIÊNCIAS
DEPARTAMENTO DE FÍSICA

Optical Calibration of the SNO+ Experiment and Sensitivity Studies for the Neutrinoless Double Beta Decay

Ana Sofia Carpinteiro Inácio

Mestrado em Física
Física Nuclear e Partículas

Dissertação orientada por:
Professor Doutor José Carvalho Maneira
Doutora Gersende Prior

2017

Abstract

SNO+ is a large volume liquid scintillator experiment for neutrino physics located 2 km underground near Sudbury, Ontario, Canada. Its main physics goal is to search for the neutrinoless double beta decay of the isotope ^{130}Te. Neutrinoless double beta decay is a lepton number violating process that, if observed, could prove the Majorana nature of neutrinos, *i.e.*, that they are their own antiparticles, as well as allow the measurement of their effective mass.

The search for this rare process requires low backgrounds and enough precision to discriminate them. It also needs an optimized energy resolution, that is only accomplished by a full calibration of the detector. This includes an Optical Calibration, that is fundamental to characterize the propagation and collection of the optical photons created by physics events. The laserball is one of the light sources used, producing a pulsed, near-isotropic light distribution throughout the detector. Its data is used to obtain the parameters of an optical model, responsible for characterizing the response of the detector to light, through a χ^2 minimisation performed by the Optical Calibration Analysis software.

This thesis describes the Optical Calibration of the SNO+ detector, the laserball source, the statistical fit and its validation tools. It also discusses how changes in the optical parameters affect the energy scale and resolution of the neutrinoless double beta decay spectrum and the calculation of its half-life.

KEYWORDS
Neutrino Physics, Neutrinoless Double Beta Decay, Calibration

Resumo

Esta tese descreve a Calibração Óptica do detector SNO+ e os efeitos da óptica na sensibilidade para a procura do decaimento beta duplo sem neutrinos do isótopo ^{130}Te. SNO+ reutiliza o detector construído para a experiência SNO (1999-2006) para estudos de física de neutrinos, tais como a detecção de neutrinos solares, geo-neutrinos, neutrinos de reatores e de supernovas, assim como estudos de física exótica como o decaimento invisível de nucleões. No entanto, o objectivo principal da experiência é a procura do decaimento beta duplo sem neutrinos do ^{130}Te que, se observado, provaria a natureza de Majorana dos neutrinos, permitindo a medição da sua massa efetiva, e forneceria pistas relativamente ao problema da hierarquia das massas dos neutrinos. Para isso, SNO+ vai contar com uma massa de ^{130}Te da ordem dos 1330 kg, com os baixos fundos devido à sua localização subterrânea e a sua capacidade para os rejeitar, assim como uma resolução em energia optimizada. Esta última é garantida através de uma calibração detalhada do detector, incluindo a Calibração Óptica que é responsável por caracterizar a propagação e captura de luz no detector.

Eventos dentro do detector criam luz que é detectada por $\sim$9300 fotomultiplicadores (PMTs). A propagação dos fotões vai ser modificada durante a sua viagem até aos PMTs: vão ser dispersados e atenuados ao longo da distância percorrida, refractados e reflectidos ao atravessar de um meio para o outro, e a captura vai ser influenciada pelo ângulo sólido dos PMTs assim como pela sua eficiência e resposta angular. Para caracterizar todos estes efeitos, uma das fontes utilizada pela Calibração Óptica é uma esfera difusora de luz quase isotrópica chamada *laserball*. A relação entre a quantidade de luz directa detectada pelos PMTs e os efeitos ópticos do detector é dada pelo Modelo Óptico, que é um modelo parametrizado que também inclui as anisotropias na distribuição de luz da *laserball*. Os parâmetros do modelo são obtidos dos dados da *laserball*, a diferentes posições e comprimentos de onda, por um fit estatístico realizado pela ferramenta de software *Optical Calibration Analysis* (OCA).

A experiência SNO+ vai ter três fases diferentes: a Fase da Água, a decorrer durante a escrita desta tese, seguida da Fase de Cintilador Puro e da Fase de Adição de Telúrio, na qual se vai tentar observar o decaimento beta duplo sem neutrinos. A primeira fase da experiência é crucial para realizar uma Calibração Óptica detalhada do detector de modo a medir as respostas angulares dos PMTs e as atenuações do meios em que a luz se propaga. Enquanto não é obtido o conjunto completo de dados de *laserball* necessários para a calibração, têm sido usados dados de Monte Carlo e de SNO para testar e validar o funcionamento da OCA, assim como criar análises mais rápidas e simples para verificar a qualidade dos dados da *laserball* e para validar os parâmetros ópticos obtidos. Este é o caso da *Diagonal Scan Analysis*, que obtém os coeficientes de atenuação do meio contido dentro do reservatório de acrílico a partir de dados com a *laserball* em posições ao longo de uma diagonal do detector, e da *Laserball Asymmetry Analysis*, que caracteriza a distribuição angular da *laserball* através de dados com a *laserball* no centro do detector mas com diferentes

orientações.

Durante extensos testes com dados de Monte Carlo, a *Diagonal Scan Analysis* e a *Laserball Asymmetry Analysis* mostraram uma boa capacidade em reproduzir os parâmetros ópticos usados como input para simular os dados. No caso da *Laserball Asymmetry Analysis*, o bom desempenho desta ferramenta levou à adaptação da OCA para receber os parâmetros da distribuição angular da *laserball* como input para o fit, reduzindo o espaço de parâmetros do fit e o tempo necessário para este ser feito. Testes à OCA com dados de Monte Carlo também mostraram o seu bom desempenho em reproduzir os parâmetros ópticos usados como input nos dados simulados, enquanto que testes com dados de SNO validaram o funcionamento do fit com dados reais de *laserball*.

Desde o ínicio da Fase da Água de SNO+ já foram obtidos alguns dados com a *laserball*. Estes são importantes para realizar um conjunto de verificações, tais como verificar a estabilidade do detector e do laser, ajustar os parâmetros do laser e da *laserball* (como por exemplo a intensidade), criar e testar as ferramentas de verificação da qualidade dos dados e testar as ferramentas necessárias para preparar os dados antes de serem usados pelo fit da OCA. Algumas destas ferramentas já foram criadas e testadas com sucesso e continua em progresso o desenvolvimento das ferramentas de verificação da qualidade dos dados e dos testes com a intensidade do laser, que em breve resultarão no conjunto de dados completo para a Calibração Óptica.

A última parte desta tese foca-se nos efeitos que os parâmetros ópticos têm nos mecanismos de reconstrução de energia e, consequentemente, na sensibilidade para a procura do processo de decaimento beta duplo sem neutrinos. A motivação para estes estudos residiu no facto de os refletores em torno dos PMTs, usados para aumentar a captura de luz, se degradarem ao longo do tempo, resultando numa diminuição da resposta angular dos PMTs, assim como o facto das atenuações dos meios, em particular do cintilador, poderem mudar com o tempo. Uma questão importante surgiu: se os efeitos ópticos não forem bem caracterizados e controlados ao longo do tempo, qual será o impacto no estudos do decaimento beta duplo sem neutrinos?

Para responder a esta pergunta, foram simulados eventos de decaimento beta duplo sem neutrinos usando respostas angulares dos PMTs e comprimentos de atenuação escalados, assim como uma amostra de controlo que usou os parâmetros ópticos padrão, vindos da experiência SNO. Os resultados mostram que os parâmetros ópticos escalados, que não são tidos em consideração pelos mecanismos de reconstrução, induzem variações na escala e resolução em energia do espectro do decaimento beta duplo sem neutrinos. As variações na resolução em energia foram mais consideráveis no caso das respostas angulares escaladas, onde a resolução em energia relativa aumentou em comparação com a amostra de controlo. Isto significa que uma incorreta caracterização da resposta angular dos PMTs resulta na redução da capacidade de separar corretamente o pico do decaimento beta duplo sem neutrinos dos eventos de fundo. Por outro lado, escalar o comprimento de atenuação do cintilador afetou consideravelmente o valor da energia reconstruída dos eventos, resultado num desvio do pico em comparação com a amostra de controlo. A energia reconstruída é aproximadamente proporcional ao número de fotões detectados que, se o detector estiver bem calibrado, deve ser igual ao número de fotões gerados pelo evento. Assim, comprimentos de atenuação mais pequenos resultam numa menor energia reconstruída, pois mais fotões são absorvidos e desviados durante o seu caminho dentro do detector. Por outro lado, comprimentos de atenuação maiores resultam numa maior energia reconstruída porque mais fotões chegam até aos PMTs.

O tempo de meia-vida do decaimento beta duplo sem neutrinos do isótopo ^{130}Te é calculado a partir do número de eventos detectados dentro de uma Região de Interesse (ROI) que é determinada

por simulações de Monte Carlo. Um dos factores do cálculo é a eficiência da detecção do sinal, que é também determinada a partir de simulações detalhadas e corresponde ao número de eventos detectados no ROI a dividir pelo número total de eventos. As variações na energia causadas pelos parâmetros ópticos escalados afetam diretamente a eficiência e, consequentemente, a determinação do tempo de meia-vida. Para além disso, resultam num erro sistemático que se vai propagar para a incerteza do tempo de meia-vida.

Deste modo, uma Calibração Óptica detalhada é crucial para a experiência SNO+, de forma a garantir uma boa precisão e sensibilidade para atingir os objetivos de física e para obter medições e limites competitivos. Para além disso, calibrações frequentes permitem um controlo regular da resposta óptica do detector, garantido que os dados recolhidos ao longo do tempo são consistentes uns com os outros.

Acknowledgements

I would like to start by thanking my supervisors José Maneira and Gersende Prior. This journey started the day you gave me the opportunity to start working with the SNO+ LIP group. Your patience to teach me and help me, as well as your hard work and wisdom, have been a source of inspiration and an example. For that, thank you.

I would also like to thank the remaining members of the SNO+ LIP group, for all their helpful comments and suggestions throughout my work, and the members of the SNO+ Collaboration who have been following my work and, in particular, those who gathered the time and patience necessary to teach me how to operate the detector.

The acknowledgements wouldn't be complete without thanking my closest friends and my family: my parents, that supported since the beginning my interest in following Physics; Nuno and Paula, and in particular Francisco, who I hope one day will find in my work inspiration to follow his dreams.

Finally, I would like to thank Diogo for all his unconditional support during this whole journey.

I would like to acknowledge the financial support from the Portuguese Foundation for Science and Technology (FCT) through the research grant PTDC/FIS-NUC/0640/2014.

Contents

List of Tables

List of Figures

Acronyms

SM	Standard Model of Particle Physics
PMNS	Pontecorvo-Maki-Nakagawa-Sakata
NH	Normal neutrino mass Hierarchy
IH	Inverted neutrino mass Hierarchy
NME	Nuclear Matrix Element
PSF	Phase Space Factor
MSW	Mikheyev-Smirnov-Wolfenstein
pep	Proton-electron-proton fusion chain
CNO	Carbon-Nitrogen-Oxygen fusion cycle
PMT	Photomultiplier Tube
AV	Acrylic Vessel
DCR	Deck Clean Room
PSUP	PMT Support Structure
OWL	Outward Looking
OCA	Optical Calibration Analysis
MC	Monte Carlo
LB	Laserball
URM	Umbilical Retrieval Mechanism
DSA	Diagonal Scan Analysis
LAA	Laserball Asymmetry Analysis
FV	Fiducial Volume

Chapter 1

Introduction

"I have done something very bad today by proposing a particle that cannot be detected; it is something no theorist should ever do."
— Wolfgang Pauli

When Wolfgang Pauli postulated the neutrino, there was little hope that this particle would ever be detected and studied. Fortunately, due to the persistence of physicists and the advances in detection technologies, neutrino physics is nowadays one of the most active research areas in Particle Physics. Almost 90 years after its postulation and 60 years after its experimental observation, there are still several open questions relative to the properties of neutrinos and their nature that are opening doors to physics beyond the Standard Model of Particle Physics. The observation of the neutrino oscillation phenomena showed that neutrinos have mass, which is not predicted by the Standard Model. It is not known where the mass comes from or what its value is, and these questions are urging a new generation of neutrino physics experiments to find the answers.

This Chapter intends to briefly present the history of the neutrino, starting from its postulation and ending with the current open questions in neutrino physics. It will then focus on the neutrino mass, showing how one can infer the existence of a non-zero mass from the oscillation phenomena, and presenting the theories that explain its nature. The last part of this Chapter will focus on the theoretical and experimental aspects of the neutrinoless double beta decay, $0\nu\beta\beta$, one of the few processes that could help understanding the nature of the neutrino mass, and whose search is the main goal of the SNO+ experiment.

1.1 The Neutrino

In the early 1910s, the study of the beta decay provided the first physical evidence for the existence of neutrinos. The first nuclear models considered the beta decay as an electron, with a fixed energy, being ejected from a nucleus. The experimental observations showed that, instead, the electron had a continuous distribution of energies up to the Q-value[1] of the decay. Wolfgang Pauli proposed, in 1930, that there should be a third particle participating in the decay, carrying part of the decay energy. This new particle should be neutral, very light and have spin 1/2 [2].

Later, in 1934, Enrico Fermi incorporated the light neutral particle suggested by Pauli into his theory of the beta decay, naming it "neutrino". In his model, a beta decay corresponds to the

[1] Energy released in the decay, defined as the difference between the initial and final nuclear mass energies [1].

conversion of a neutron into a proton, with the emission of an electron and antineutrino:

$$n \rightarrow p + \bar{\nu}_e + e^-. \tag{1.1}$$

The experimental observation of the neutrino only happened 22 year later, in 1956, by the reactor-neutrino experiment developed by Clyde L. Cowan and Frederick Reines [3]. They took advantage of the large flux of antineutrinos produced by nuclear reactors to search for the inverse beta decay process:

$$\bar{\nu}_e + p \rightarrow n + e^+. \tag{1.2}$$

The estimated cross section for this reaction was of the order of 10^{-44} cm^2, so small that even with a calculated antineutrino flux of 5×10^{13} at the detector, Cowan and Reines could only see two or three events every hour. The experimental observation of neutrinos led to the attribution of the Nobel Prize in 1995 to Reines[2] [4].

Neutrinos were included in the Standard Model (SM) of particle physics as massless weakly interacting particles that carry no electric or colour charges, explaining their long penetration length in matter and the difficulty in their detection. With further experiments, it was verified that there are three neutrinos, ν_e, ν_μ and ν_τ, associated to each one of the charged leptons e^-, μ^- and τ^-. The three types are commonly identified as neutrino flavours and can be observed through interactions with their corresponding leptons.

In the years following the observation of neutrinos by Cowan and Reines, there was a boost in the number of neutrino experiments dedicated to their observation and characterization, using other sources besides reactors, such as the sun, cosmic rays interacting with the atmosphere and accelerators. In the 1960s, the Homestake experiment measured the flux of electron neutrinos arriving from the core of the Sun and found a value that was between one third and one half of the number predicted by the Standard Solar Model [5]. This discrepancy, which became known as the *Solar Neutrino Problem*, remained unresolved for thirty years. The hypothesis postulated was that the neutrino flavours had nonzero and slightly different masses, and during their path to Earth, they could oscillate between flavours. A deficit was also observed by atmospheric neutrino experiments. The oscillation phenomenon was confirmed by the Super-Kamiokande (SK) and SNO experiments in the late 90s and early 2000s, showing direct evidence of non-zero neutrino masses through their results [6, 7]. The results from SK showed a suppression in atmospheric neutrinos dependent on flavour and distance, and SNO demonstrated flavour transformation in solar neutrinos.

The observation of neutrino flavour oscillations and the implication that they have a non-zero mass made the SM an effective theory of an yet unknown theory beyond the SM, opening doors to new and more fundamental questions:

- What is the absolute value of the neutrino mass?
- Through what mechanism does the neutrino mass arise?
- Why is the neutrino mass so small when compared with other fermions?

Several theoretical efforts have been developed throughout time to explain the neutrino mass, but the answers to these questions depend on future experimental results.

[2] Clyde L. Cowan passed away in 1974.

1.2 Neutrino Mass and Flavour Mixing

The observation of neutrino flavour oscillations provided evidence that neutrinos have a non-zero mass, unlike what the SM predicts. It is then important to understand how one infers the existence of mass from the observation of this phenomenon.

In 1957, Bruno Pontecorvo developed the theory of neutrino oscillations between neutrino and anti-neutrino [8]. Later in 1962, Z. Maki, N. Nakagawa and S. Sakata applied this idea to the oscillation of neutrino flavours [9]. Each neutrino flavour state is a linear superposition of three neutrino mass states, each with a different mass:

$$|\nu_\alpha\rangle = \sum_{k=1}^{3} U^*_{\alpha k}|\nu_k\rangle, \quad \alpha = e, \mu, \tau. \tag{1.3}$$

The coefficients $U_{\alpha k}$ are elements of an unitary matrix U known as the Pontecorvo-Maki-Nakagawa-Sakata (PMNS) mixing matrix, which can be parametrised by three mixing angles, θ_{12}, θ_{23}, θ_{13} and a charge-parity (CP) phase δ_{CP}:

$$U = \begin{pmatrix} c_{12}c_{13} & s_{12}c_{13} & c_{13}e^{-i\delta_{CP}} \\ -s_{12}c_{23} - c_{12}s_{23}s_{13}e^{i\delta_{CP}} & c_{12}c_{23} - s_{12}s_{23}s_{13}e^{i\delta_{CP}} & s_{23}c_{13} \\ s_{12}s_{23} - c_{12}c_{23}s_{13}e^{i\delta_{CP}} & -c_{12}s_{23} - s_{12}c_{23}s_{13}e^{i\delta_{CP}} & c_{23}c_{13} \end{pmatrix}, \tag{1.4}$$

with $c_{ij} = cos\theta_{ij}$ and $s_{ij} = sin\theta_{ij}$. The general expression of the transition probability from an initial neutrino flavour state α to another flavour state β, as a function of the distance *L* travelled and neutrino energy E_ν, is:

$$P_{\nu_\alpha \to \nu_\beta}(L, E_\nu) = \sum_{k,j=1}^{3} U^*_{\alpha k} U_{\beta k} U_{\alpha j} U^*_{\beta j} exp\left(-i\frac{\Delta m^2_{kj} L}{2E_\nu}\right). \tag{1.5}$$

Equation 1.5 shows that the probability of flavour transition varies with the distance travelled *L* and the neutrino energy E_ν, and it is weighted by the elements of the PMNS matrix and the mass squared differences Δm^2_{kj}:

$$\Delta m^2_{21} = m^2_2 - m^2_1; \quad \Delta m^2_{31} = m^2_3 - m^2_1; \quad \Delta m^2_{32} = m^2_3 - m^2_2. \tag{1.6}$$

Only two of these mass differences are independent, because Δm^2_{31} can be expressed as $\Delta m^2_{31} = \Delta m^2_{32} + \Delta m^2_{21}$, and at least two of the masses should be different from zero.

From Equation 1.5 it is clear that the experimental measurements of neutrino oscillations imply massive[3] neutrinos, yielding precise information only on the values of the squared-mass differences but not on the absolute values of neutrino masses.

The SK and SNO experiments determined that the sign of Δm^2_{21} is positive from the analysis of solar data, meaning that $m^2_2 > m^2_1$. This was possible because these experiments were sensitive to the Mikheyev–Smirnov–Wolfenstein (MSW) effect that, in a medium with varying density such as the sun, enhances the neutrino flavour oscillations. However, it is unknown whether or not m_2 is heavier than m_3, which is known as the *Neutrino Mass Hierarchy Problem*. If m_2 is lighter than m_3, the hierarchy is said to be "normal", but if it is heavier the hierarchy is called "inverted"

[3] Massive, *i.e.* that have a non-zero mass.

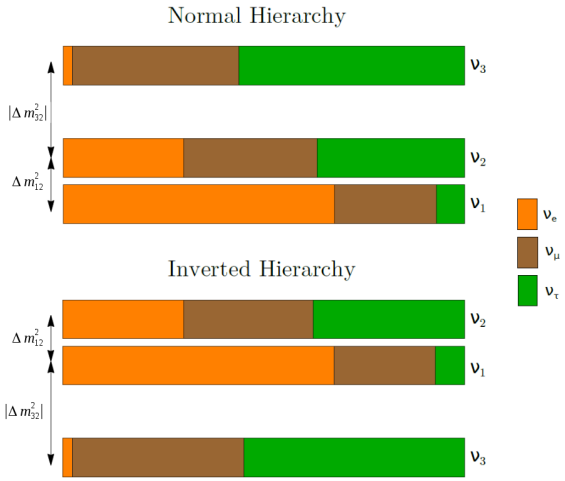

Figure 1.1: The two possibilities for the neutrino mass hierarchy: normal where $m_3 > m_2$ and inverted where $m_3 < m_2$. Modified figure from [10].

(Figure 1.1).

Bounds on the absolute value of the masses can be obtained from Cosmology, the study of kinematic effects of supernova neutrinos, the single beta decay and the neutrinoless double beta decay processes [10].

Current Values and Limits on the Neutrino Mixing Parameters and Masses

There has been a huge effort from neutrino experiments in improving their sensitivities to obtain more precise values of the neutrino oscillation parameters, as well as to improve the upper and lower bounds on the neutrino masses. Table 1.1 shows the most recent results of the 3ν oscillation parameters, from solar, reactor, atmospheric and accelerator neutrino experiments.

Table 1.1: Best-fit results of the global 3ν oscillation analysis, from solar, reactor, atmospheric and accelerator neutrino experiments [11, 12]. The CP violating phase is taken in the interval $\delta_{CP}/\pi \in [0, 2]$. The values of $sin^2\theta_{13}$, $sin^2\theta_{23}$, Δm^2_{32} and δ/π are presented for both the Normal Hierarchy (NH) and the Inverted Hierarchy (IH).

Parameter	Best Fit
$sin^2\theta_{12}$	0.297
$sin^2\theta_{13}$ (NH)	0.0215
$sin^2\theta_{13}$ (IH)	0.0216
$sin^2\theta_{23}$ (NH)	0.425
$sin^2\theta_{23}$ (IH)	0.589
Δm^2_{21}	7.37 $\times 10^{-5}$ eV^2
$\lvert\Delta m^2_{32}\rvert$ (NH)	2.44$\times 10^{-3}$ eV^2
$\lvert\Delta m^2_{32}\rvert$ (IH)	2.51$\times 10^{-3}$ eV^2
δ_{CP}/π (NH)	1.38
δ_{CP}/π (IH)	1.31

The values of the absolute neutrino masses are still unknown. Lower bounds are set by the oscillation data by zeroing the lightest m_i (for the NH, the lightest is m_1; for the IH, the lightest

is m_3):

$$(m_1, m_2, m_3) \geq \begin{cases} (0, \sqrt{\delta m^2}, \sqrt{|\Delta m^2| + \delta m^2/2}) & \text{(NH)} \\ (\sqrt{|\Delta m^2| - \delta m^2/2}, \sqrt{|\Delta m^2| + \delta m^2/2}, 0) & \text{(IH)} \end{cases} , \qquad (1.7)$$
$$\geq \begin{cases} (0, 0.86, 5.06) \times 10^{-2} \text{ eV} & \text{(NH)} \\ (4.97, 5.04, 0) \times 10^{-2} \text{ eV} & \text{(IH)} \end{cases}$$

where $\delta m^2 = m_2^2 - m_1^2 > 0$ and $\Delta m^2 = m_3^2 - (m_2^2 + m_1^2)/2$.

Upper bounds come from the effective neutrino mass $m_\beta = \sqrt{\sum_i |U_{ei}|^2 m_i^2}$ in the single β-decay, from the effective mass $m_{\beta\beta} = \left| \sum_{i=1,2,3} e^{i\xi_i} \left| U_{ei}^2 \right| m_i \right|$ in the neutrinoless double beta decay and from the total neutrino mass $\Sigma = m_1 + m_2 + m_3$ in Cosmology. Although not direct, in the last couple of years Cosmology has provided very stringent upper bounds, with different values depending on the cosmological model used. The most recent cosmological fit results are presented in [11], from where the lowest upper bound on Σ (2σ) is:

$$\Sigma < \begin{cases} 0.18 \text{ eV} & \text{(NH)} \\ 0.2 \text{ eV} & \text{(IH)} \end{cases} \qquad (1.8)$$

The KamLAND-Zen experiment has given the most constraining bounds on $m_{\beta\beta}$. By assuming the most favourable nuclear matrix elements for their calculations, $m_{\beta\beta} < 0.165$ eV [13].

The upper bounds from the single beta decay are weaker than the previous. From tritium beta decay experiments, $m_\beta < 2$ eV [12, 14].

1.2.1 Nature of the Neutrino Mass

Although the experimental observations imply that neutrinos have mass, the mechanism that gives rise to them is still unknown. There are two main theories that explain the nature of the neutrino mass: Dirac and Majorana. Both are here presented and discussed.

Dirac Neutrino Mass

In the Standard Model, neutrinos are included in the SU(2)$_L$×U(1)$_Y$ symmetry group, regarding electroweak interactions [15]. They are massless states described only by left-handed chiral fields $\nu_{\alpha L}$ that satisfy the Weyl equation, a variation of the Dirac equation for describing massless spin-1/2 particles,

$$i\gamma^\mu \partial_\mu \nu_{\alpha L} = 0 \, . \qquad (1.9)$$

A Dirac neutrino mass can be generated with the same Higgs mechanism that gives masses to quarks and charged leptons in the SM if one introduces the right-handed components $\nu_{\alpha R}$ of the neutrino fields ($\alpha = e, \mu, \tau$). These fields are called *sterile* because they do not participate in weak interactions (as well as strong and electromagnetic interactions); their only interaction is gravitational. Besides, they are invariant under the SM symmetries, making them fundamentally different from the fields of other elementary fermions.

In the natural extension with three right-handed neutrino fields, ν_{kR} ($k = e, \mu, \tau$), the Higgs-lepton Yukawa Lagrangian is:

$$\mathcal{L}_{H,L} = -\sum_{\alpha=e,\mu,\tau} \frac{y_\alpha^\ell v}{\sqrt{2}} \overline{\ell_\alpha} \ell_\alpha - \sum_{k=1}^{3} \frac{y_k^\nu v}{\sqrt{2}} \overline{\nu_k} \nu_k - \sum_{\alpha=e,\mu,\tau} \frac{y_\alpha^\ell v}{\sqrt{2}} \overline{\ell_\alpha} \ell_\alpha H - \sum_{k=1}^{3} \frac{y_k^\nu v}{\sqrt{2}} \overline{\nu_k} \nu_k H \,, \quad (1.10)$$

where ℓ_α are the Dirac charged lepton fields, ν_k are the Dirac neutrino fields, H is the Higgs field and y_α^ℓ and y_k^ν are, respectively, charged lepton and neutrino Yukawa couplings. Both lepton and neutrino fields are the sum of the right- and left-handed fields:

$$\ell_\alpha = \ell_{\alpha L} + \ell_{\alpha R} \quad (\alpha = e, \mu, \tau), \quad (1.11)$$

$$\nu_k = \nu_{kL} + \nu_{kR} \quad (k = 1, 2, 3). \quad (1.12)$$

The massive Dirac neutrinos couple to the Higgs field through the last term in Equation 1.10, where the neutrino masses are given by

$$m_k = \frac{y_k^\nu v}{\sqrt{2}} \quad (k = 1, 2, 3). \quad (1.13)$$

The neutrino masses obtained with this mechanism are proportional to the Higgs VEV v (vacuum expectation value), $\sim$ 246 GeV, as the masses of charged leptons and quarks. However, it is known that the masses of neutrinos are much smaller than those of the charged leptons and quarks, requiring very small values for the eigenvalues y_k^ν. This may be problematic since the SM does not account for their sizes. Besides, there is no evidence for the existence of right-handed neutrinos, making the Higgs mechanism unsatisfactory in explaining the neutrino masses and opening doors to new theories beyond the SM, one of which has been explored in detail in the last few years: the Majorana mass theory.

Majorana Neutrino Mass

In 1937, Ettore Majorana proposed a new form of the Dirac equation, in which all coefficients are real, that is completely symmetric with respect to particles and antiparticles. While it led to only formal improvements for charged fermions, it opened up a very important new possibility for neutral ones - they can be their own antiparticles [10, 15, 16]. This is achieved if the fermion field $\psi = \psi_L + \psi_R$ satisfies the Majorana condition

$$\psi = \psi^C \quad \text{with} \quad \psi^C = C\overline{\psi}^T, \; C = i\gamma^2\gamma^0 \,, \quad (1.14)$$

where ψ^C is the charge conjugated field and C is the charge conjugation operator. The Majorana theory reduces the four-component Dirac spinors into two-component spinors, requiring the left-handed and right-handed fields, ψ_L and ψ_R, to be related. The reduction from four to two degrees of freedom makes the Majorana theory simpler and more economical than the Dirac one.

The Majorana Lagrangian can be written as

$$\mathcal{L} = \frac{1}{2}\overline{\psi} i\gamma^\mu \partial_\mu \psi - \frac{M}{2}\overline{\psi}\psi \,. \quad (1.15)$$

The last term in Equation 1.15 is the mass term. This term is not invariant under $U(1)$ transformations, breaking electric charge conservation [16]. Since the electric charge should always be conserved, no charged particles can have a Majorana mass. Among the known elementary

fermions, only the neutrinos are neutral and, therefore, possible candidates to Majorana particles.

The lowest dimensional term that could generate a Majorana neutrino mass using SM model fields, and respecting the SM symmetries, is:

$$\mathcal{L}_5 = \frac{1}{2}\frac{g}{\mathcal{M}}(L^T_{\alpha L}\tau_2\Phi)C^\dagger(\Phi^T\tau_2 L_{\alpha L}) + h.c. \tag{1.16}$$

where τ_2 is the Pauli matrix, g is a dimensionless coupling coefficient and $\mathcal{M}$ is a constant with dimensions of mass [15]. $L_{\alpha L}$ is a SM lepton doublet for the generation α and Φ is the Higgs doublet. From this Lagrangian, the following Majorana mass is generated:

$$m = \frac{m_D^2}{\mathcal{M}}\ , \tag{1.17}$$

where m_D is a typical Dirac mass that can have the same order of magnitude as the charged lepton or quark mass of the same generation. $\mathcal{M}$ can then be made sufficiently large so that the neutrino mass scale is in accordance with the experimental limits. This is the so-called *seesaw mechanism*.

If neutrinos have a Majorana mass the seesaw mechanism predicts that, for each of the three neutrino generations, there is a very light neutrino with a mass much smaller than the other SM fermions and a very massive neutrino with $m_N \approx \mathcal{M}$. This mechanism, if proved that neutrinos have a Majorana mass, could explain the leptogenesis and thus the observed asymmetry between matter and anti-matter in the universe [17].

One experimental consequence of neutrinos being Majorana particles would be the possibility of observing the neutrinoless double beta decay, which is discussed in the next Section.

1.3 Neutrinoless Double-Beta Decay

Following the postulation of the neutrino and the development of the β-decay theory, M. Goeppert-Mayer suggested that nuclei could disintegrate via two simultaneous β-decays, accompanied by the emission of two electrons and two anti-neutrinos [18]:

$$(A, Z) \rightarrow (A, Z+2) + 2e^- + 2\bar{\nu}\ . \tag{1.18}$$

This process, now commonly called two neutrino double-beta decay, $2\nu\beta\beta$, was detected for the first time in 1950 at a geochemical experiment with ^{130}Te by M. Inghram and J. Reynolds, where they estimated an half-life for this process of $T_{1/2} = 1.4 \times 10^{21}$ [19].

The $2\nu\beta\beta$-decay is possible for some nuclei with even mass number A. These nuclei are divided into two mass parabolas, as illustrated by Figure 1.2, one for nuclei with odd numbers of protons and neutrons, placed above the other for nuclei with even numbers of protons and neutrons. Nuclei β-decay between the two parabolas to reach stability, *i.e.* the minimum mass value. Often, even-even nuclei on the parabola are left as being stable because the β decay to the odd-odd nucleus requires energy, not happening spontaneously, like the example of the ^{130}Te in Figure 1.2. Instead, ^{130}Te can disintegrate via a double beta decay to ^{130}Xe, the minimum of the even-even parabola. This type of decay is very rare, and that is reflected by the large half-lives that have been measured experimentally.

There are 35 naturally-occurring isotopes that can decay by $2\nu\beta\beta$-decay. However, there are only twelve different nuclei where this process has been observed experimentally [12]. They are

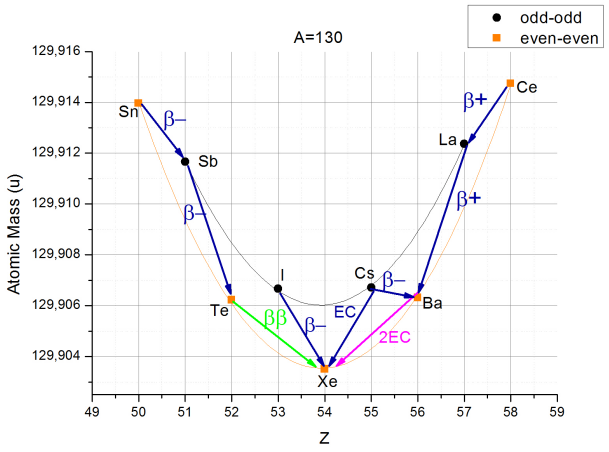

Figure 1.2: Mass parabola representation for A=130. For even A nuclei there are two mass parabolas, one for odd-odd nuclei placed above other for even-even nuclei. The nuclei on the left side decay via β^- and the ones on the right side decay via β^+.

shown in Table 1.2, along with their corresponding isotopic abundance, Q-value and measured half-lives.

Table 1.2: List of isotopes that have been observed experimentally to decay by $2\nu\beta\beta$-decay, along with their isotopic abundance, Q-value and measured half-lives [12].

Isotope	Isotopic Abundance (%)	$Q_{\beta\beta}$ [MeV]	$T^{1/2}(2\nu\beta\beta)$ [10^{21} yr]
^{48}Ca	0.187	4.263	$(6.4^{+0.7+1.2}_{-0.6-0.9})\times10^{-2}$ [20]
^{76}Ge	7.8	2.039	(1.926±0.095) [21]
^{78}Kr	0.36	2.848	$(9.2^{+5.5}_{-2.6}\pm1.3)$ [22]
^{82}Se	9.2	2.998	$(9.6 \pm 0.24\ ^{+0.67}_{-0.59})\times10^{-2}$ [23]
^{96}Zr	2.8	3.348	(2.35±0.14±0.16)×10^{-2} [24]
^{100}Mo	9.6	3.035	(6.93±0.04)×10^{-3} [25]
^{116}Cd	7.6	2.813	(2.74±0.04±0.18) [26]
^{128}Te	31.74	0.868	(7.7±0.4)×10^{3} [27]
^{130}Te	34.08	2.527	$(0.82 \pm 0.02 \pm 0.06)$ [28]
^{136}Xe	8.9	2.459	(2.165±0.016±0.059) [29]
^{150}Nd	5.6	3.371	$(9.34\pm0.22^{+0.62}_{-0.60})$ [30]
^{238}U	99.2745	1.144	(2.0±0.6) [31]

The possibility of neutrinos being Majorana particles results in a new possible disintegration process, the neutrinoless double beta decay, $0\nu\beta\beta$. Its observation is currently the most promising way to prove the Majorana nature of neutrinos. It consists of a nucleus decaying via two simultaneous beta decays with the emission of two electrons, but without the emission of neutrinos, as explicit in Equation 1.19. Figure 1.3 shows the Feynman diagram for this process.

$$(A, Z) \rightarrow (A, Z + 2) + 2e^- \ . \tag{1.19}$$

The $0\nu\beta\beta$ candidates are the isotopes that can decay by the $2\nu\beta\beta$-decay, listed in Table 1.2

An evident feature of this decay is the explicit violation of the lepton number conservation. The discovery of this decay would then demonstrate that the lepton number is not a symmetry in nature, supporting the theoretical picture that leptons played a part in the creation of the matter–

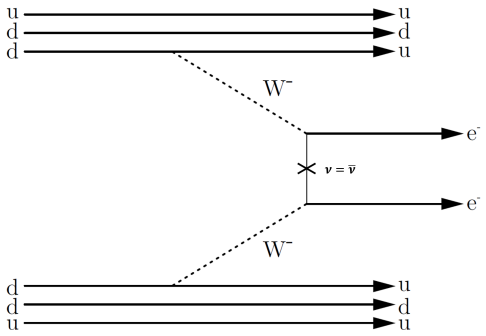

Figure 1.3: Feynman diagram of the $0\nu\beta\beta$ process.

antimatter asymmetry in the universe.

The effective Majorana mass of the electron neutrino participating in the $0\nu\beta\beta$ transition can be defined as

$$m_{\beta\beta} = \left| \sum_{i=1,2,3} e^{i\xi_i} \left| U_{ei}^2 \right| m_i \right| , \tag{1.20}$$

where U_{ei} are the coefficients of the PMNS mixing matrix, m_i are the neutrino mass states and ξ_i are Majorana phases.

Because $0\nu\beta\beta$ is a nuclear process, the transition has to be described taking into account the relevant aspects that concern nuclear structure and dynamics. The theoretical expression of the half-life of the process can be factorized as [10]:

$$\left[T_{0\nu}^{1/2} \right]^{-1} = G_{0\nu} |\mathcal{M}_{0\nu}|^2 \left| \frac{m_{\beta\beta}}{m_e} \right|^2 , \tag{1.21}$$

where $G_{0\nu}$ is the phase space factor (PSF) that describes the physics of the final emitted states, $\mathcal{M}_{0\nu}$ is the nuclear matrix element (NME), describing the energetic transition of the nucleus between its initial and final state, m_e is the electron mass and $m_{\beta\beta}$ is the effective Majorana mass. From this expression it is clear that if the half-life of the $0\nu\beta\beta$ process of a certain isotope is measured experimentally, one could in principle obtain a value for the effective Majorana mass of the electron neutrino.

Furthermore, a future value of $m_{\beta\beta}$, along with the oscillation parameters, can provide information about the mass hierarchy of the neutrinos. That is illustrated by Figure 1.4, where predictions of $m_{\beta\beta}$ for the NH and IH cases are shown as a function of the lightest neutrino mass, m_1 for NH and m_3 for IH. The horizontal bands show the combined experimental limits for the ^{76}Ge, ^{130}Te and ^{136}Xe isotopes, with the spread due to the theoretical uncertainties on the NMEs and PSF.

Experimentally, the searches for a $0\nu\beta\beta$ signal rely on the detection of the two emitted electrons. Because the energy of the recoiling nucleus is negligible, the sum of the kinetic energy of the two electrons should be equal to the Q-value of the transition (Figure 1.5). However, one of the main challenges is to distinguish the small number of electron pairs produced by this process from the large continuum of electron pairs produced through two neutrino double-beta decay, $2\nu\beta\beta$. In order to separate these two signals, experiments need to have a very good energy resolution.

Besides the experimental uncertainties, the determination of the effective Majorana mass also depends on the NMEs, provided by nuclear physics calculations. The main theoretical models used

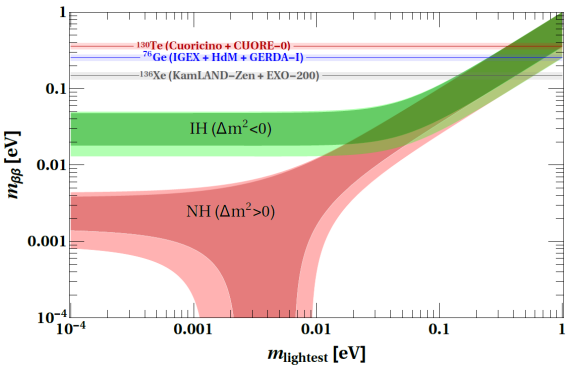

Figure 1.4: Predictions on $m_{\beta\beta}$ as a function of the lightest neutrino mass. The horizontal bands show the combined experimental limits for the ^{76}Ge, ^{130}Te and ^{136}Xe isotopes, with the spread due to the theoretical uncertainties on the NMEs and PSF. Figure from [10].

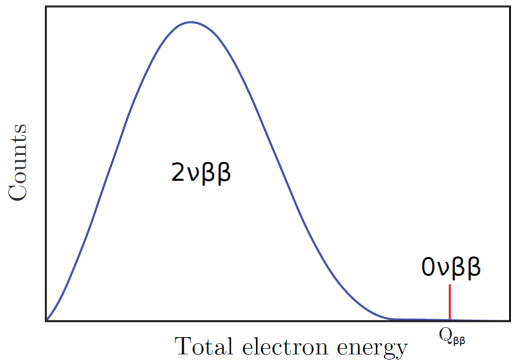

Figure 1.5: Schematic view of the $2\nu\beta\beta$ and $0\nu\beta\beta$ spectra. Figure from [10].

for the calculations are the ISM (*Interacting Shell Model*), QRPA (*Quasiparticle Random Phase Approximation*), IBM-2 (*Interacting Boson Model*), PHFB (*Projected Hartree-Fock Bogoliubov Method*) and EDF (*Energy Density Functional Method*). A review of these models can be found in [10].

The NMEs calculation is a difficult task because the ground and many excited states of open-shell nuclei with a complicated nuclear structure have to be considered. They are obtained by solving the Dirac equation for the wavefunctions of the many states considered in the local potential within the nucleus. The wavefunctions have a small overlap, inducing a large uncertainty in the Hamiltonian and hence in the NMEs. The uncertainties in the NMEs can go up to 20%, and are different depending of the nuclear model assumed [10].

1.3.1 Experimental Searches

The search for the $0\nu\beta\beta$-decay is a big challenge for experimental particle physics. Several aspects have to be considered in order to achieve the best sensitivity possible. The first one is the choice of the isotope, that has a series of criteria in order to optimize the background levels and energy resolution, while at the same time allowing the scalability of the experiment. The chosen isotope should have:

- A Q-value larger than ∼2.4 MeV, in order to neglect most of the low energy backgrounds, such as the natural gamma-radioactivity that has its end-point at 2.615 MeV;
- High isotopic abundance or possibility of enrichment, to allow having experiments with a

sufficiently large mass to probe in a reasonable time the extremely long half-lives predicted for the process;

Some of the isotopes in Table 1.2 that meet these requirements are commonly used to search for the $0\nu\beta\beta$-decay.

The characteristics of the detector itself also play an important role in the searches. It must have a good energy resolution, crucial to separate the $0\nu\beta\beta$ peak from other signals; it should be located underground, to be protected from cosmic rays, and should use radio-pure materials and shielding to protect against environmental radioactivity and, last but not least, must allow the use of a large isotope mass, in order to increase the rate of events. Most detectors use the calorimetric technique, in which the source is embedded in the detector itself. Some examples include Ge-diodes (GERDA experiment [32]), bolometers (CUORE experiment [33]), liquid and gaseous Xe Time Projection Chambers (TPCs) (EXO experiment [34]), and liquid scintillators loaded with the $0\nu\beta\beta$ isotope (KamLAND-Zen [13] and SNO+ [35] experiments). Other detectors use sources that are different from the detector (NEMO experiment [25]). While this technique may allow the use of different sources, it becomes more difficult to scale-up.

So far, no evidence for the existence of the $0\nu\beta\beta$ has been found. Hence, experimental results can only provide limits on the $0\nu\beta\beta$ half-life of some isotopes and, implicitly, on the value of $m_{\beta\beta}$. The half-life sensitivity of this process, $S^{0\nu}$, is defined as the maximum signal that could be hidden by background fluctuations at a given statistical confidence level and it depends on whether the experiment has backgrounds or is in "zero background"[4] conditions. With "zero background", the sensitivity is proportional to the exposure (mass M $\times$ time of measurement T) and the isotopic abundance η; with background, it is inversely proportional to the background level B and the energy resolution ΔE [10]:

$$S^{0\nu} \propto \epsilon\eta MT \qquad (\text{"zero background"}) , \tag{1.22}$$

$$S^{0\nu} \propto \epsilon\eta\sqrt{\frac{MT}{B\Delta E}} \qquad (\text{background limited}) , \tag{1.23}$$

where ϵ is the detection efficiency. For some experiments, the number of background counts *B* can have a contribution from backgrounds that scale with the mass of the experiment and backgrounds from constant sources [36, 37]. The basics for detecting this process are a large source mass, excellent energy resolution and an extremely low background in the $0\nu\beta\beta$ peak region.

Table 1.3 presents the characteristics of $0\nu\beta\beta$ experiments that have already published their results. It is worth noting that a subset of the Heidelberg-Moscow collaboration claimed to observe the $0\nu\beta\beta$ decay [38], but their results were not confirmed by other experiments and were later disproved by the GERDA experiment [39].

One of the future $0\nu\beta\beta$ experiments is SNO+, that will use 780 tonnes of liquid scintillator loaded with $\sim$1330 kg of ^{130}Te. The expected $0\nu\beta\beta$-decay signal of ^{130}Te and background spectrum for a five-year live-time of the detector is shown in Figure 1.6. The $0\nu\beta\beta$ signal shown is for a $m_{\beta\beta}$ of 200 meV, using the IBM-2 model for the calculation of the NMEs. The expected sensitivity for the half-life at 90% C.L. after 5 years is $S^{0\nu} = 1.96 \times 10^{26}$ years, corresponding to a $m_{\beta\beta}$ range of 38 to 92 meV[5].

[4] No background means that the background level is so low that the expected number of background events in the region of interest along the experiment life is of the order of unity [10].

[5] The range includes the $m_{\beta\beta}$ values estimated using the different NMEs.

Table 1.3: List of $0\nu\beta\beta$ experiments with published results. Information on the isotope used, the total mass, exposure and on the sensitivities are included.

Experiment	Isotope	Total Mass [kg]	Exposure [kg yr]	$S^{0\nu}$ (90% C.L.) [10^{25} yr]
Heidelberg-Moscow [38]	^{76}Ge	11.5 (^{enr}Ge)	50.5	1.55
IGEX [40]	^{76}Ge	8.1 (^{enr}Ge)	8.9	1.57
EXO-200 [34]	^{136}Xe	175 (^{enr}Xe)	100	1.1
KamLAND-Zen [13]	^{136}Xe	348 (^{enr}Xe)	504	10.7
GERDA I & II [?]	^{76}Ge	17.6 & 35.6 (^{enr}Ge)	21.6 & 100	5.3 (combined)
CUORE [?]	^{130}Te	206 (^{130}Te)	9.8	0.27
NEMO-3 [25]	^{100}Mo	6.9 (^{100}Mo)	34.3	0.11

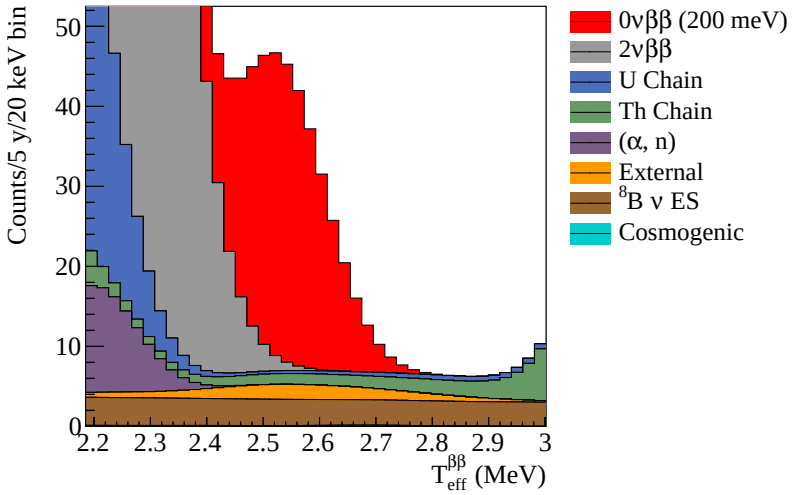

Figure 1.6: Expected $0\nu\beta\beta$ signal and background spectrum for a five-year live-time of the SNO+ experiment using 1330 kg of ^{130}Te and assuming an hypothetical effective Majorana Mass of 200 meV.

In order to achieve the expected sensitivity for the search of the $0\nu\beta\beta$-decay in SNO+, a detailed and accurate knowledge of the detector and its components is required. This is achieved by performing a full detector calibration, including the characterization of the optical properties of the detector, which is going to be the main topic of this thesis.

Chapter 2 provides a summary of the SNO+ detector and its experimental goals. Chapter 3 presents the *laserball*, the main Optical Calibration source, and shows how the optical response of the detector is characterized using its data through the Optical Model. It also presents the Optical Calibration Analysis (OCA), responsible for obtaining the optical parameters from the data. Chapter 4 focuses on the analysis of Optical Calibration data: it starts by presenting the tools developed to validate the results of the Optical Calibration Analysis, then it presents and discusses the tests to OCA using Monte Carlo and SNO data, and finally are presented the first results of laserball data from the SNO+ experiment. Chapter 5 discusses the effects of changes in the optical parameters on the $0\nu\beta\beta$-decay sensitivity and half-life. Chapter 6 concludes this thesis with a summary of the work presented and the main conclusions concerning the importance of the Optical Calibration for the achievement of the SNO+ physics goals.

Chapter 2

Overview of the SNO+ Detector

The SNO+ experiment consists of a large volume liquid scintillator detector located 2 km underground in Vale's Creighton Mine, Sudbury, Canada. The deep underground location, the high purity of the materials used and its large volume make SNO+ an ideally suited detector to study several aspects of neutrino physics.

2.1 Physics Goals

The main goal of SNO+ is the search for the neutrinoless double-beta decay ($0\nu\beta\beta$) of the ^{130}Te isotope [35]. The $0\nu\beta\beta$-decay is a rare nuclear process that, if observed, would prove the Majorana nature of the neutrinos, would demonstrate violation of the lepton number and would contribute to the measurement of the effective electron neutrino mass, as well as provide clues to solve the mass hierarchy problem. SNO+ will use a very large isotope mass, $\sim$1330 kg (loading of 0.5% by weight), and will rely on the low backgrounds due to the underground location and on the cleanliness of the detector constituents.

Other physics goals include measurements of geo-neutrinos, to help understanding the mechanisms for heat production in the Earth; reactor antineutrinos, whose measurements constrain the neutrino oscillation parameters; and neutrinos and antineutrinos coming from supernova explosions. Additionally, some exotic physics searches will be performed, concerning axion-like particles and invisible nucleon decay[1].

The depth of the detector and its radio-purity also provide the opportunity to measure low energy solar neutrinos, like pep and CNO neutrinos. The pep neutrinos are monoenergetic, with an energy of 1.44 MeV and have a very well predicted flux, with an uncertainty of 1.2%, constrained by the solar luminosity [42]. A precise measurement of the flux can probe the Mikheyev–Smirnov–Wolfenstein (MSW) effect of neutrino oscillations in matter. The measurements of the CNO neutrino flux could help understanding the distribution of elements heavier than helium in the Sun [43].

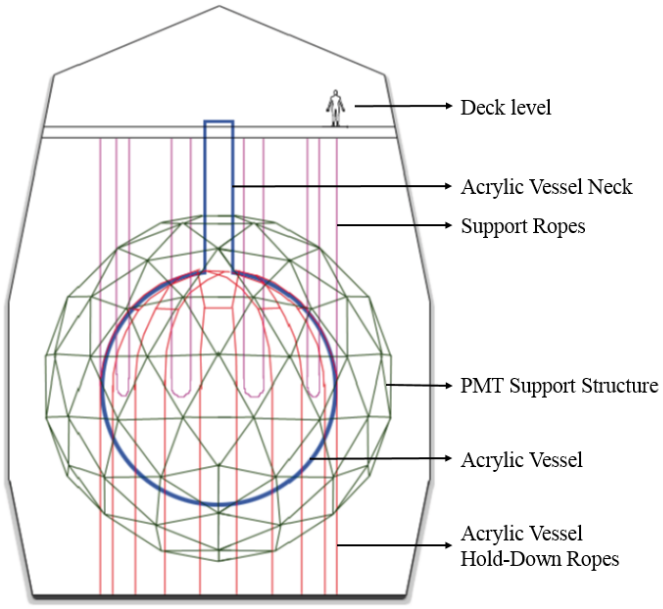

Figure 2.1: The SNO+ detector [35]. The 12 m acrylic vessel (in blue) is viewed by ∼9400 PMTs fixed in the 17.8 m diameter PSUP (green). The AV is held in place by a system of support ropes (purple) and hold-down ropes (red).

2.2 Structure of the Detector

The SNO+ experiment reuses most of the components of the Sudbury Neutrino Observatory detector (SNO) that operated from 1999 to 2006. The 2092 m underground location provides an efficient shield against cosmic muons, resulting in a muon rate of 63 muons per day through a 8.3 m radius circular area [44]. The detector consists of a spherical acrylic vessel (AV), with a thickness of 55 mm and 12 m in diameter, surrounded by a 17.8 m diameter geodesic steel structure that holds ∼9400 PMTs and other detector components, called PMT Support Structure (PSUP). These are inside a barrel shape cavity 22 m wide and 34 m high. A schematic diagram of the detector is shown in Figure 2.1.

The volume between the AV and the PSUP, as well as the rest of the cavity, will be filled with 7000 tonnes of ultra-pure water that provide a shield against the radioactivity from the instrumentation and surrounding rock. The detection medium inside the AV will change for the different data taking phases of the experiment [35]:

- Water Phase: the acrylic vessel will be filled with 905 tonnes of ultra-pure water, with the main goal of searching for exotic physics. A full calibration of the detector will be performed, as well as a characterization of the backgrounds.
- Pure Scintillator Phase: the acrylic vessel will be filled with 780 tonnes of LAB-PPO liquid scintillator, where solar, geo and reactor neutrinos will be measured.
- Te-loading Phase: 1.33 tonnes of ^{130}Te will be added to the liquid scintillator in order to search for the neutrinoless double beta decay process.

The PSUP is supported by cables connected to bolts on the deck of the cavity. The acrylic vessel is held in place by a net of support ropes and hold-down ropes. The hold-down ropes

[1]Invisible nucleon decay is any process that could cause a nucleon to decay to some mode which goes undetected, like for example n$\rightarrow \nu\nu\nu$ [41]. The disappearance of a nucleon from a nucleus results in an unstable daughter nucleus that will decay emitting gamma rays.

are an addition relative to SNO times, and their purpose is to cancel the buoyancy of the acrylic vessel when it is filled with the liquid scintillator (because the liquid scintillator has a smaller density than water). The acrylic vessel is connected to the deck level above the cavity through a cylindrical neck, from where deployable sources can be inserted to calibrate the detector.

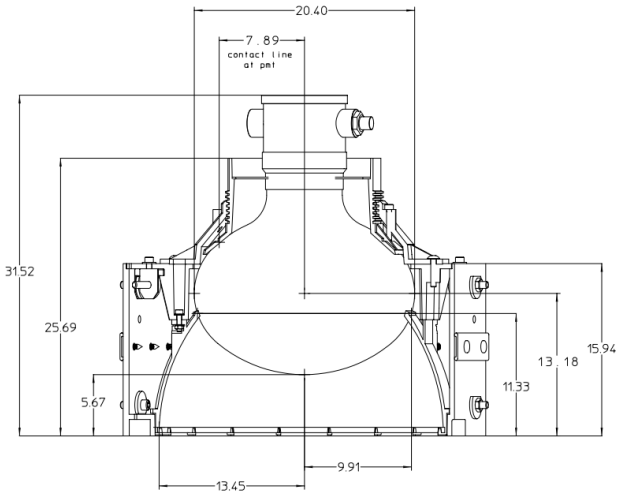

Figure 2.2: PMT and light-concentrator housing schema with dimensions, in cm. Figure from [45].

Almost all of the ∼9400 20.3 cm in diameter Hamamatsu R1408 PMTs are the same as used in SNO, except for some that were damaged and had to be fixed or replaced. From this number, approximately 9200 are looking inwards the PSUP, detecting the light created by particle interactions inside the AV. In addition, there are a few PMTs in the AV neck and about 90 outward looking PMTs (OWLs) located on the outer surface of the PSUP, used to detect light from external sources, such as cosmic muons.

The inward looking PMTs are surrounded by concave petal-like reflectors, formed into a Winston cone of 27 cm in diameter, referred to as concentrator. It redirect light onto the PMT face (Figure 2.2), increasing the effective photocathode coverage to about 59%. The light collection efficiency of the PMT and reflectors assembly (or *PMT Angular Response*) increases with the incident angle of light in the range of angles from 0° to 50°, but beyond this angle it rapidly drops off due to design constraints of the reflectors [46].

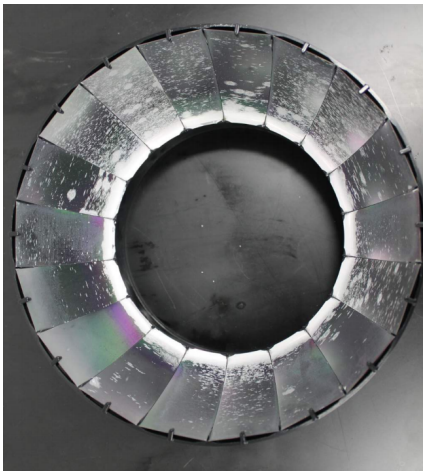

Figure 2.3: Degraded PMT reflectors used in SNO [47]. The white spots are areas of degraded reflectivity.

Because some of the PMTs are almost 20 years old, the reflectors have started to degrade over time, which results in a reduction of the overall collection efficiency. Figure 2.3 shows one example of a set of degraded reflectors from SNO. During the transition from SNO to SNO+ it is possible that the reflectors have degraded more than what was observed by the end of SNO. Therefore, it is crucial to characterize the PMT angular response in the Water Phase of SNO+ in order to account for these changes when characterizing the response of the detector.

2.3 Calibration Systems

The SNO+ detector will be calibrated using both optical and radioactive sources. The optical sources are used to verify the PMT response and to measure in-situ the optical properties of the detector media, while the radioactive sources are used to check the energy scale and resolution, the linearity of the response and to determine the systematic uncertainties and the efficiency of all reconstructed quantities (*i.e.* energy, position, direction). Additionally, a system of cameras placed in six equidistant positions on the PSUP will be used to monitor the position of the acrylic vessel and the hold-down rope system, and to triangulate the positions of the calibration sources inserted into the detector [35]. The whole calibration hardware has been designed to match the purity requirements of SNO+ and the need to have materials compatible with the liquid scintillator.

The radioactive sources (beta, gamma and neutron) considered are listed in Table 2.1, covering the range from 0.1 to 6 MeV.

Table 2.1: List of radioactive sources that are considered for use to calibrate the SNO+ detector, the particles emitted by each and their energy.

Source	Particle	Energy
AmBe	n, γ	2.2, 4.4 MeV
^{16}N	γ	6.1 MeV
^{24}Na	γ	2.7, 1.3 MeV
^{48}Sc	γ	1.0, 1.2, 1.3 MeV
^{57}Co	γ	122 keV
^{60}Co	γ	1.2, 1.4 MeV
^{90}Y	β	2.3 MeV

The optical calibration hardware consists of internally deployable sources and a system of optical fibers attached to the PSUP in fixed positions, as outlined by Figure 2.4 (b). The fibers send pulses from fast LEDs or lasers into the detector, allowing frequent calibrations of the PMTs response, time and gain, and to measure the scattering and attenuation lengths of the media. The deployable sources are a light diffusing sphere, commonly called *laserball*, responsible for characterizing the media attenuations and the PMT and reflector assembly response to light, and a Cherenkov source, used for PMT efficiency measurements.

The calibration sources are deployed into the detector using a source manipulator system illustrated in Figure 2.4 (a). The manipulator system is located in the Deck Clean Room (DCR), above the detector. Inside the AV, the sources are moved by a system of high-purity ropes in either a North/South or East/West plane (defined in Figure A.1), allowing the detector response to be measured as a function of the position in the AV. An Umbilical [2] is used to transmit power, light

[2]Multi-purpose cable containing optical fibers (for light transmission), thin coaxial gas tubing and four hook-up cables [48].

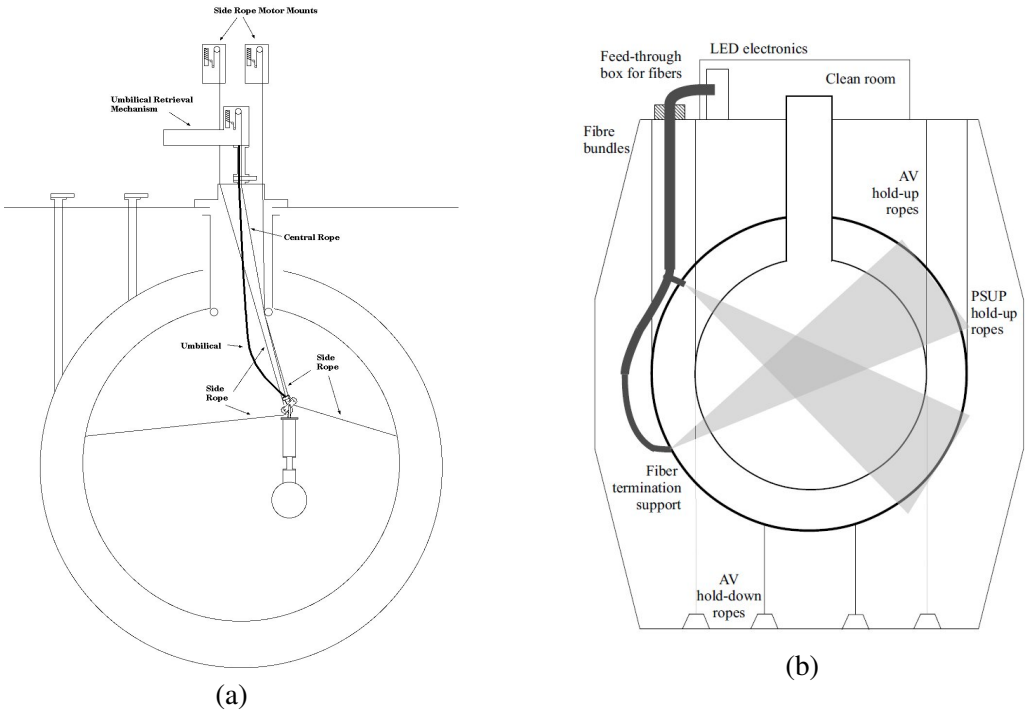

Figure 2.4: Cross sectional diagrams of the SNO+ detector. (a) shows the deployment of the laserball inside the acrylic vessel [48], and (b) shows the fibre system fixed on the PMT geodesic structure [49].

pulses and other signals to the source. The Umbilical is deployed from an Umbilical Retrieval Mechanism (URM), located in the DCR.

Chapter 3

Optical Calibration

When particles interact inside the SNO+ detector, they lose energy and create light that is detected by the PMTs. While travelling, the media attenuations, reflections and refractions will affect the propagation of the photons inside the detector. Furthermore, the intrinsic shape of the PMTs makes the collection of light dependent on the incidence angle of the incoming photons. This results in a decrease of the amount of light detected relative to the light produced, that will vary with the position inside the detector where the particles interacted, as illustrated by Figure 3.1. If the optical effects and detector properties changing the propagation of light are not taken into account in the physics analysis, or if they are incorrectly characterized, the energy and position reconstruction will give wrong results and SNO+ will lose its sensitivity for particle identification and background discrimination.

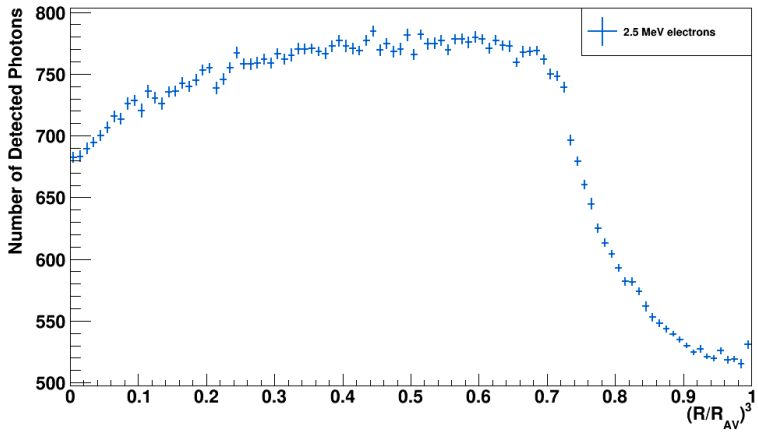

Figure 3.1: Number of photons detected as a function of the position inside the AV where 2.5 MeV electrons were generated. This result comes from a Monte Carlo simulation with electrons of constant energy that were generated randomly inside the AV volume. The changes in the light detected with the position are clearly visible.

Therefore, in order to understand the signals detected and to correctly associate them with the underlying physics processes, a precise knowledge of the detector optical properties is required. This is achieved with a detailed optical calibration using the laserball.

This Chapter will describe in more detail the laserball source and present the Optical Model that is used to characterize the light propagation and collection in the detector. It will also present OCA, the SNO+ software responsible for the analysis of laserball data and for extracting the model parameters.

3.1 The Laserball

The laserball is the main optical calibration source of the SNO+ experiment because it allows a full characterization of the detector response to light. It was designed to act as a point-like source of light with an isotropic emission throughout the detector volume [48]. A schema of the laserball is shown in Figure 3.2.

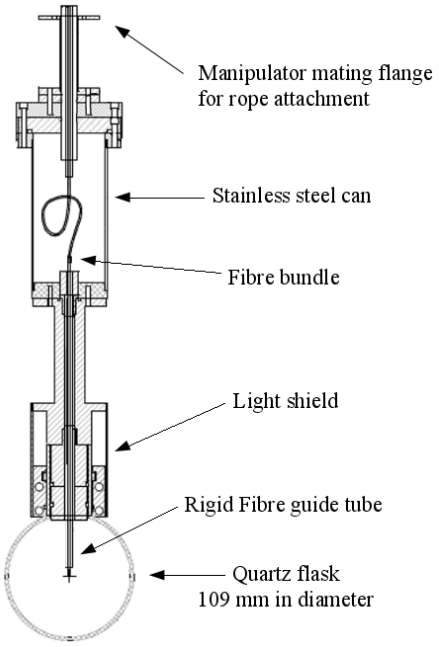

Figure 3.2: Schema of the SNO laserball that is going to be used during the SNO+ Water Phase Optical Calibration. Modified version from [48].

It consists of a quartz flask with 10.9 cm in diameter, filled with 2 g of small air-filled glass beads (50 μm in diameter) suspended in silicone gel. The beads are responsible for scattering the light that is injected into the flask through a fibre guide. The injected light comes from a nitrogen laser, located in the DCR, emitting pulses of light with a wavelength λ = 337 nm. Its typical rate is $\sim$40 Hz, and each time it sends a pulse, a photodiode close to it is partially illuminated, producing a square wave that sends a trigger signal to the data acquisition system. The laser contains a movable mirror that moves parallel to the light-beam, redirecting the beam into one of five resonators. The resonators contain dyes that change the peak wavelength of the original laser light:

- PBD dye, λ_{LB} = 369 nm
- BBQ dye, λ_{LB} = 385 nm
- Bis-MSB dye, λ_{LB} = 420 nm
- COUMARIN-450 dye, λ_{LB} = 446 nm
- COUMARIM-500 dye, λ_{LB} = 505 nm

These dyes are going to be used during the water phase and additional dyes are planned for the scintillator phase. A full description of the laser system is given in [48]. The flask is held by a stainless steel mounting hardware attached to a manipulator rope guide system that allows the

deployment and change of position of the source inside the detector. In the water phase of the SNO+ experiment, the optical calibration will make use of the last SNO laserball, and for the scintillator phase a redesigned laserball is being developed at the University of Sussex.

The optical calibration with the laserball is performed by collecting PMT data while the laserball is pulsing light at a fixed position, that can be central (in the center of the AV) or off-axis (away from the center of the AV). A set of data collected with the same position and wavelength settings is a *run*. A laserball *scan* is formed by many runs in different positions and wavelengths.

3.2 Optical Model

The Optical Model is essential to characterize the detector physical properties as a function of wavelength, position and direction [46]. It is a simplified model which uses geometrical optics and includes parameters such as the attenuations of the different media (water, acrylic, scintillator), the PMT responses and efficiencies, as well as parameters that quantify the intensity distribution of the laserball.

The model assumes that the detector can be well characterized by averaging some of its properties, such as considering that the media is homogeneous and isotropic and that the PMT response depends only on the incident angle of light. Furthermore, it only accounts for light coming directly from the source to a PMT. The direct light is identified by imposing a narrow time window on the data to identify the prompt light in each PMT, thus ignoring signals due to pre- and late-pulsing of the PMTs or reflections from the detector elements. This is illustrated by Figure 3.3, showing the time residual[1] distribution from a MC simulation of the laserball placed at the center of the AV.

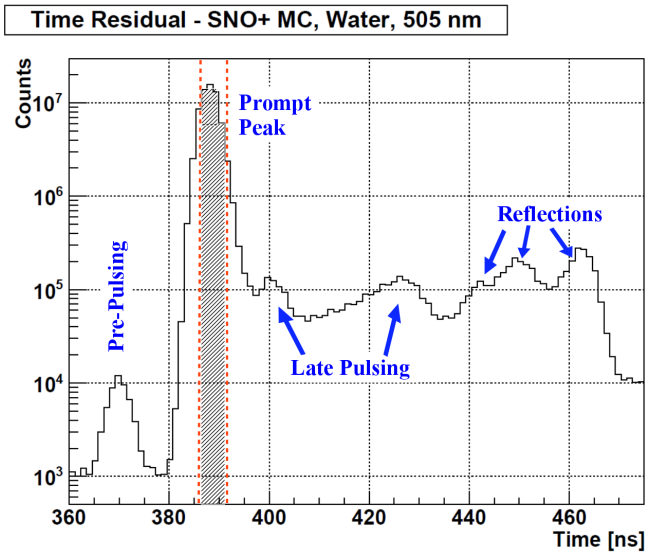

Figure 3.3: Time residual distribution in water at 505 nm from a MC simulation with the laserball placed in the center of the AV. Shown are the peaks due to direct light (prompt peak), pre- and late-pulsing, and reflections from the detector components. The two dashed red lines define the time window that is imposed on data to identify the prompt light in each PMT.

[1]The time residual of a PMT corresponds to the PMT hit time shifted by the time of flight, which is the time that light takes to travel from the source to the PMT.

The occupancy O_{ij} observed for a laserball run i by the PMT j is defined as:

$$O_{ij} = \frac{N_{ij}^{data}}{N_i^{pulses}} \, , \tag{3.1}$$

where N_i^{pulses} is the number of pulses emitted by the laserball and N_{ij}^{data} is the number of hits registered by the PMT *j*, within a time window[2] of ± 4 ns [50]. The optical model relates O_{ij} with the optical properties of the detector and the source as follows [51]:

$$O_{ij} = N_i \Omega_{ij} R_{ij} T_{ij} L_{ij} \epsilon_j e^{-(d_{ij}^a \alpha_a + d_{ij}^b \alpha_b + d_{ij}^c \alpha_c)} \, , \tag{3.2}$$

where the parameters are:

- N_i - number of photons emitted per pulse by the laserball in run *i*, and detected within a prompt timing window by all PMTs;
- Ω_{ij} - solid angle subtended by PMT *j* from the laserball position in run *i*. Calculated numerically based on the detector geometry and on the laserball and PMT positions;
- R_{ij} - PMT and reflector assembly angular response beyond the solid angle Ω_{ij}. This factor is parametrised as a function of the photon incident angle on the PMT surface;
- L_{ij} - laserball light distribution expressed as a function of the local angular coordinate frame of the laserball, *i.e.* $L_{ij}(\theta_{LB}, \phi_{LB})$;
- T_{ij} - Fresnel transmission coefficients for the media interfaces. Calculated analytically, based on the laserball and PMT positions;
- ϵ_j - absolute quantum efficiency of PMT *j* combining the overall PMT efficiency and electronics threshold effects (including the *quantum efficiency (QE)*, which refers to the wavelength-dependent probability of registering a hit);
- $d_{ij}^{a,b,c}$ - light path lengths through the media. Calculated analytically based on the detector geometry;
- $\alpha_{a,b,c}$ - attenuation coefficients for the optical media;

There are several terms in the model that can be calculated just by knowing the laserball and PMT positions: the solid angle, Ω_{ij}, the Fresnel transmission coefficients, T_{ij}, and the light path lengths in each medium. The remaining terms are extracted from laserball data through an optical calibration fit, that is going to be described in Section 3.3. A precise characterization of all these parameters is obtained by deploying the laserball at many locations in the detector for a different number of wavelengths.

The reason for including the laserball parameters (intensity, position, orientation and intensity distribution) in the model is because the laserball itself is not totally isotropic, as will be discussed in Subsection 3.2.3, and the source manipulator system has an associated uncertainty in the position that depends on the tension of the holding ropes and that varies with the position in the detector.

[2] Value for the water phase data. The timing window depends on the media. For scintillator, the value is going to be different, depending on future studies.

3.2.1 Media Attenuation

The attenuation coefficient characterizes how easily light propagates along a medium. It is the inverse of the attenuation length, $\alpha = \lambda_{att}^{-1}$, meaning that a medium with a large attenuation coefficient attenuates (or weakens) light quickly as it passes through, and a medium with a small attenuation coefficient is relatively transparent to light.

In general, the attenuation coefficient is related to the absorption and Rayleigh scattering coefficients through the expression:

$$\alpha_{attenuation} = \alpha_{absorption} + \alpha_{Rayleigh} \, . \tag{3.3}$$

Absorption happens when the full energy of a photon is transferred to the matter in the medium, whereas Rayleigh scattering corresponds to the (dominant) elastic scattering of the photons by particles in the medium with sizes smaller than the light wavelength.

Rayleigh scattering has a strong dependency on the wavelength of light, λ [52]:

$$\alpha_{Rayleigh} = \frac{8\pi^3}{3\lambda^4} \left[\frac{(n^2-1)(2n^2+0.8n)}{n^2+0.8n+1} \right]^2 k_B T \kappa_T \frac{6+3\delta}{6-7\delta} \, , \tag{3.4}$$

where *n* is the refractive index, *T* is the temperature, κ_T is the isothermal compressibility at temperature T and δ is a depolarisation factor. At a constant *T* and *n*, small wavelengths result in large scattering coefficients, whereas large wavelengths results in small scattering coefficients. The probability of a photon being scattered at an angle θ with respect to its original direction is:

$$P(\theta) \sim (1 + cos^2\theta) \, . \tag{3.5}$$

The attenuation measurement with the Optical Model only uses direct light reaching the PMTs, identified by the prompt time window. In principle, the Rayleigh scattering contributes to the attenuation by removing light from the prompt peak. However, there is a probability that light will be scattered forward and be included in it. This extra light will increase the attenuation length λ, thus decreasing the attenuation coefficient α. The forward-scattered light reduces the contribution of the Rayleigh scattering coefficient to the attenuation coefficient, leading to:

$$\alpha_{attenuation}^{prompt} = \alpha_{absorption} + k\alpha_{Rayleigh} \, . \tag{3.6}$$

This effect was studied in detail during the SNO experiment and the factor *k* was determined using detailed Monte Carlo simulations of the detector, yielding a value $k = 0.820 \pm 0.003$. For further details refer to [46]. Once there is a full set of SNO+ laserball data the contribution of the Rayleigh scattering to the prompt time window will be again studied.

3.2.2 PMT Angular Response

The PMT angular response is the combined efficiency of the PMT and reflector in collecting light with a given incident angle, θ_γ, relative to the normal incidence, $\theta_\gamma = 0$. The incident angle of light is defined as the angle to the normal of the entrance plane, shown in Figure 3.4 (a). Besides varying with θ_γ, this parameter is also wavelength dependent. Figure 3.4 (b) shows PMT angular responses that were obtained during the operation of the SNO experiment.

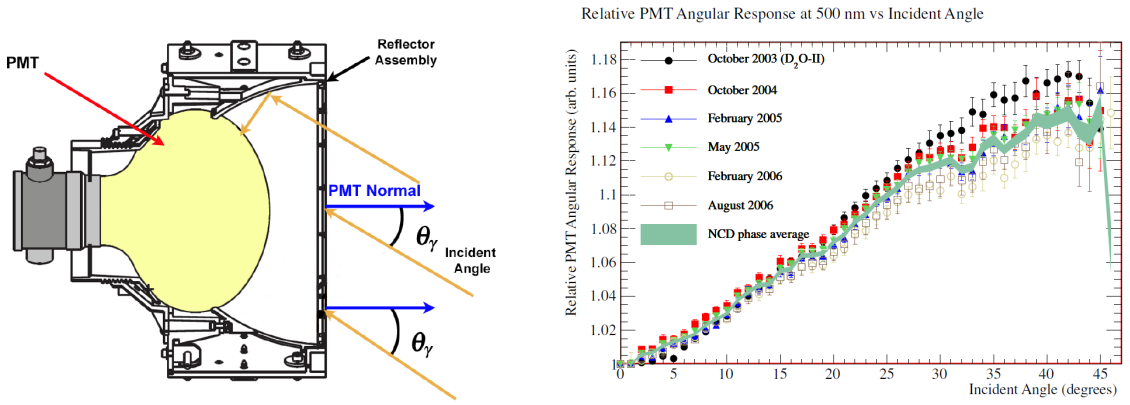

(a) (b)

Figure 3.4: (a) Schema of the PMT and reflector assembly with the definition of the normal of the entrance plane (Figure from [50]); (b) Relative PMT Angular Responses as a function of incident angle obtained during the operation of the SNO experiment (Figure from [51]).

The goal of the reflectors is to increase the effective area of the photocathode to maximize the number of photons detected, and to limit the angular acceptance of the PMTs so that they only see the central part of the detector. The effective coverage of the PMTs with reflectors is ∼60%, whereas without the reflectors it is around 34% [46]. As can be observed in Figure 3.4 (b), the PMT angular response increases with the incident angle almost linearly up to 30-40 degrees (depending on wavelength) and then starts decreasing. For the angles beyond 45 degrees, it is hard to characterize the PMT angular response with the laserball inside the AV because there are limitations on the positions that can be reached with the deployment system. However, those measurements could be accomplished by deploying the laserball outside the AV, which has been proposed for the Water Phase of the SNO+ experiment.

One interesting feature of Figure 3.4 (b) is to notice that the PMT Angular response decreased over a period of three years in SNO. That is because the reflectors were subject to degradation caused by the ultra-pure water used to fill the cavity. SNO+ uses the same reflectors as SNO, that are now ∼20 years old. In total, the reflectors have been submerged in ultra-pure water for almost ten years, three of them since the last laserball scan performed in SNO, in 2006. It is probable that they have degraded even more, and the last measured angular response from SNO no longer reflects the current one, that should be smaller. The rate and type of reflector degradation does not seem to follow a pattern between PMTs, making it very difficult to create a model that would characterize it with time.

It is then crucial to perform a detailed Optical Calibration in the Water Phase of SNO+ in order to understand how the PMT reflectors degraded over time and how much that affected the PMT angular response. If not, the physics data would be calibrated with parameters that no longer reflect the current status of the detector.

The measured PMT angular response is also important to tune the PMT models used in the Monte Carlo simulations of the detector: the 3D PMT Model and the Grey Disc Model. While the 3D model takes a series of complicated steps to be tuned, the Grey Disc Model uses the PMT Angular Response almost as a direct input. The Grey Disc is a simplified model of the PMT and concentrator in which they have been replaced by a disc with the same radius as the maximum radius of the composed PMT and concentrator volume. When a photon reaches the disc, instead of modelling all the photon interactions, the model assigns a reflection and absorption probability

to the contact point depending on incident angle and wavelength. The fact that the PMT Angular response is directly used in the Grey Disc Model makes it easier to check how variations in the response affect the reconstruction mechanisms.

3.2.3 Laserball Light Distribution

The laserball is designed to be an isotropic light source, but in practice its light distribution shows anisotropies, that need to be accounted for by the Optical Model. For instance, the mounting hardware that supports the flask introduces shadowing in the upper part of the detector, reducing the intensity of light emitted upwards relative to the one emitted downwards [50]. This variation is described by the laserball mask function, $P_4(cos\theta_{LB})$, which has the form:

$$P_4(cos\theta_{LB}) = 1 + \sum_{k=1}^{4} a_k (1 + cos\theta_{LB})^k \,. \tag{3.7}$$

The coefficients a_k are determined by the optical calibration fit and the variation of intensity is described around a fixed normalized value, a_0 = 1. The definition of this polynomial mask function of order four was established by prior studies in SNO [53].

Also, irregularities in the distribution of the glass beads inside the laserball flask lead to both $cos\theta_{LB}$ and ϕ_{LB} angular anisotropies in the light distribution, that can be characterized by two different functions [50]:

- The binned angular distribution, $H_{bin}(cos\theta_{LB}, \phi_{LB})$, illustrated by Figure 3.5, divides the laserball into 12 $\times$ 36 bins, giving a total of 432 free parameters in the optical model.

- The sinusoidal angular distribution, $H_{sin}(cos\theta_{LB}, \phi_{LB})$, splits the laserball into several $cos\theta_{LB}$ slices, typically 24, and for each of them the relative intensity is described as:

  $$H^k(\phi_{LB}) = 1 + A_k \, sin(\phi_{LB} + \delta_k), \quad k = [1, 24] \,, \tag{3.8}$$

  where A_k controls the amplitude of the anisotropy and δ_k gives a phase shift in ϕ_{LB}. The division into slices of $cos\theta_{LB}$ allows to break the dependency from the laserball polar angle θ_{LB}. This model requires a total of 48 parameters.

The total laserball light distribution $L(cos\theta_{LB}, \phi_{LB})$ is then a composite function given by the two-dimensional angular distribution $H(cos\theta_{LB}, \phi_{LB})$ multiplied by the mask function $P_4(cos\theta_{LB})$:

$$L(cos\theta_{LB}, \phi_{LB}) = H(cos\theta_{LB}, \phi_{LB}) \times P_4(cos\theta_{LB}) \,. \tag{3.9}$$

3.3 Optical Calibration Analysis

The Optical Calibration Analysis, OCA, is designed to characterize the optical response of the SNO+ detector with laserball data, by the extraction of the optical model parameters. For that, it uses the Occupancy-Ratio method that normalises the measured occupancies for a given run, O_{ij}^{data}, by dividing them by the values from a run with the laserball in the center of the detector,

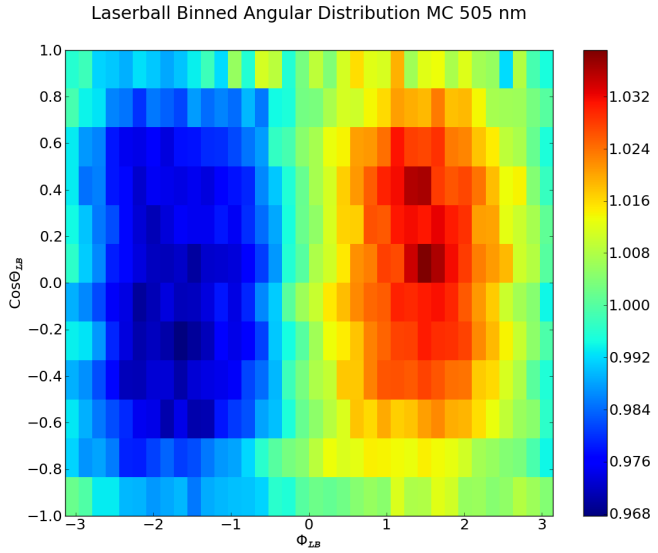

Figure 3.5: Laserball binned angular distribution from SNO+ MC data. The asymmetry of the emitted light is clearly visible, either in $cos\theta_{LB}$ and ϕ_{LB}. This distribution was obtained for a laserball scan at 505 nm.

O_{0j}^{data}:

$$OR_{ij}^{data} = \frac{O_{ij}^{data}}{O_{0j}^{data}} \,. \tag{3.10}$$

This occupancy ratio is then compared with a prediction based on the detector optical model:

$$OR_{ij}^{model} = \frac{O_{ij}^{model}}{O_{0j}^{model}} = \frac{N_i \Omega_{ij} R_{ij} T_{ij} L_{ij}}{N_0 \Omega_{0j} R_{0j} T_{0j} L_{0j}} exp\left(-\sum_k (d_{ij,k} - d_{0j,k}) \alpha_k \right) \,. \tag{3.11}$$

The advantage of the Occupancy-Ratio method is that it removes the ∼9400 PMT efficiencies, ϵ_j, from the analysis, constraining significantly the parameter space. The optical model parameters are then extracted by the minimisation of a χ^2 estimator over several iterations [50]:

$$\chi^2 = \sum_i^{\#Runs} \sum_j^{\#PMTs} \frac{(OR_{ij}^{data} - OR_{ij}^{model})^2}{\sigma_{stat,ij}^2 + \sigma_{PMT}^2(\theta_{\gamma,ij})} \,, \tag{3.12}$$

and the efficiencies of the PMTs are extracted separately after the fit is complete. The term $\sigma_{PMT}^2(\theta_{\gamma,ij})$ is a correction that accounts for a residual uncertainty in the PMT efficiency based on the incident angle of light, θ_γ. $\sigma_{stat,ij}^2 = \delta OR_{ij}^{data}$ is the uncertainty on the data occupancy ratio OR_{ij}^{data}:

$$\sigma_{stat,ij}^2 = \delta OR_{ij}^{data} = OR_{ij}^{data} \sqrt{\left(\frac{\delta O_{ij}^{data}}{O_{ij}^{data}} \right)^2 + \left(\frac{\delta O_{0j}^{data}}{O_{0j}^{data}} \right)^2} \,, \tag{3.13}$$

where δO_{ij}^{data} is the uncertainty of the measured occupancy. Looking at equation (3.1), this uncertainty is only due to the uncertainty in N_{ij}^{data}, because the number of pulses N_i^{pulses} is known exactly.

The minimisation of the χ^2 is a non-linear least squares problem that is solved using the Levenberg-Marquardt (LM) algorithm [54]. This algorithm is an adaptive technique that behaves

differently according to the distance to the minimum. It uses two methods: at large distances from the minimum it uses a gradient descent method and closer to the minimum it uses the Gauss-Newton method of minimisation which converges quicker.

The minimisation is performed over several iterations with a sequentially decreasing upper chi-square limits. After each minimisation, PMTs with a χ^2 larger than the new limit are removed from the sample.

OCA analyses the data from all laserball runs for each wavelength separately, extracting parameters for 6 wavelengths. The extracted optical parameters are later interpolated to other wavelengths using dedicated tools, in order to be used as inputs for the simulation and reconstruction algorithms.

3.3.1 Data Selection and Corrections

Before the χ^2 minimisation, several cuts to the data are performed:

- The channel hardware status of each PMT is checked to see if it was working during the run. Offline PMT channels, as well as low gain PMTs are excluded from the dataset. This number of excluded PMTs is variable;
- Only the inward looking PMTs, labelled as "Normal", are used in the fit. All the others, around 300, are excluded;
- PMTs whose optical paths cross a detector component, such as the ropes that hold the AV in place or the belly plates around the AV equator, will be shadowed by it and, consequently, will have lower occupancies. It is not yet possible to predict with enough accuracy the amount of shadowing that a detector component produces on a PMT, therefore PMTs in these conditions are excluded from the fit. For a run with the laserball in the center of the AV, this corresponds to excluding 37% of the PMTs, as illustrated by Figure 3.6.

After the cuts are performed, several corrections are applied to the occupancy, such as the solid angle, Ω, that is calculated numerically, and the Fresnel transmission coefficients, *T*, that are calculated analytically, as well as the multi photoelectron correction (MPE), which corrects for the PMT signals from multiple photoelectrons that were fired as a single hit. The multiple photoelectron signals underestimate the intensity of the laserball. The multiple photoelectron corrected occupancy, O_{ij}^{MPE}, can be determined by assuming that the true occupancy of a PMT is given by the mean of the Poisson distribution, ξ_{ij}[50].

$$\begin{aligned} Prob.(\geq 1\, Hit|O_{ij}^{data}) &= 1 - Prob.(0\, Hits|O_{ij}^{data}), \quad O_{ij}^{data} \sim Poisson(\xi_{ij}) \\ \Rightarrow O_{ij}^{data} &= 1 - \frac{(\xi_{ij})^0 e^{-\xi_{ij}}}{0!} = 1 - e^{-\xi_{ij}} \\ \Rightarrow \xi_{ij} &= -ln(1 - O_{ij}^{data}) = O_{ij}^{MPE}\,. \end{aligned} \tag{3.14}$$

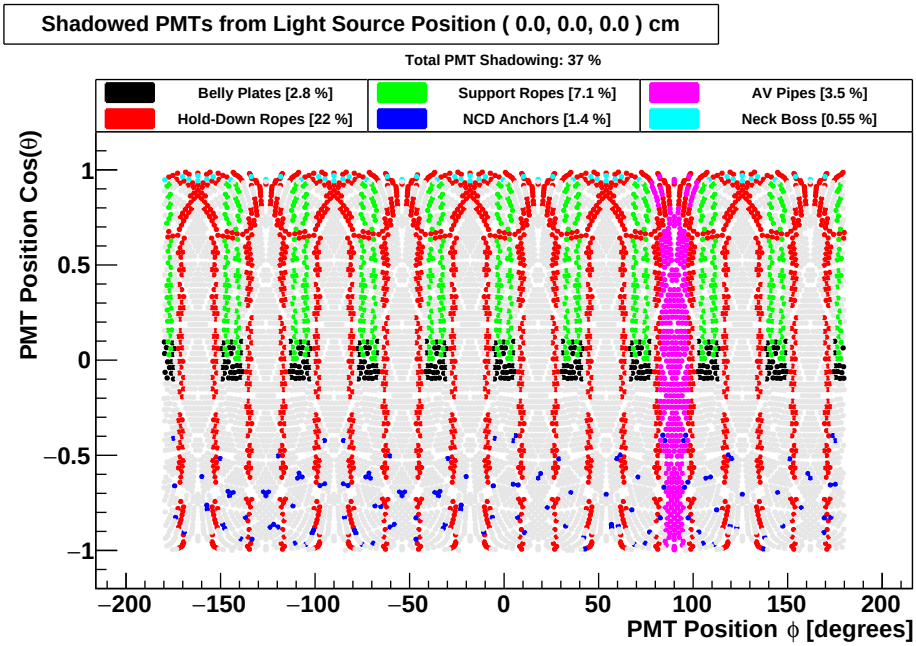

Figure 3.6: Shadowing Map of the SNO+ detector, considering the laserball placed in the center of the AV. The light grey circles represent PMTs that are not shadowed and each of the other colours represent shadowed PMTs with the identification of the shadowing source. The overall PMT shadowing in this example is 37%.

Chapter 4

Water Phase Optical Calibration: Preparation and First Results

The process of the Optical Calibration includes more than just the extraction of the optical parameters from the data. Before that can happen, it is necessary to prepare tools to check the data quality of the laserball runs, optimize the optical fit and create validation tools to corroborate the final results.

The Water Phase of the SNO+ experiment is crucial to both prepare and test the software tools and to measure optical parameters, such as the PMT angular responses, which will be more difficult to characterize in the following phases.

This Chapter presents and discusses the several analysis tools developed for the Optical Calibration and their results. It starts with two tools, the Diagonal Scan Analysis and the Laserball Asymmetry Analysis, that were adapted from SNO to SNO+ and improved using a series of tests. Their goal is to validate some of the optical parameters calculated by OCA. Next follows the results of the tests performed to the OCA software using MC and SNO data. These tests allowed the correction and improvement of some parts of the software, and validated the performance and results of the fit. Last but not least, this Chapter presents the results of the first laserball data from the SNO+ experiment. Although the data obtained was not yet enough to perform a full Optical Calibration, it was of extreme significance to test other tools intrinsic to the preparation of the laserball data for analysis, as well as to check the current status of the detector in terms of the optics.

4.1 Optics Validation Tools

The Optical Calibration Analysis, OCA, is a very complex fit responsible for extracting the Optical Model parameters from the laserball data. To validate its results, two simpler tools were developed: the Diagonal Scan Analysis, to obtain the attenuation of the medium inside the AV, and the Laserball Asymmetry Analysis, to characterize the laserball angular distribution. The simplicity and computational speed of these tools, when compared to OCA, also make them useful to check the quality of the laserball data when it is obtained.

4.1.1 Diagonal Scan Analysis

The Diagonal Scan Analysis was developed to obtain the attenuation of the medium inside the AV (water or scintillator) by using runs in which the laserball is placed along the $x = z$ and $x = -z$ diagonals of the detector[1]. In this analysis, two groups of PMTs around the intersection of the diagonal with the PSUP are chosen (Figure 4.1). The number of PMTs in each group is limited by imposing a maximum distance to the diagonal d, given by:

$$d = \sqrt{\frac{|\mathbf{x}_1 - \mathbf{x}_0|^2 \cdot |\mathbf{x}_2 - \mathbf{x}_1|^2 - \left[(\mathbf{x}_1 - \mathbf{x}_0) \cdot (\mathbf{x}_2 - \mathbf{x}_1)\right]^2}{|\mathbf{x}_2 - \mathbf{x}_1|^2}} , \tag{4.1}$$

where $\mathbf{x}_0$ is the PMT position vector, pointing from the center of the detector to the PMT, $\mathbf{x}_1$ is the vector representing the center of the detector, $\mathbf{x}_1 = (0, 0, 0)$, and $\mathbf{x}_2$ is the vector of the diagonal: for $x = z$, $\mathbf{x}_2 = (1, 0, 1)$ and for $x = -z$, $\mathbf{x}_2 = (1, 0, -1)$.

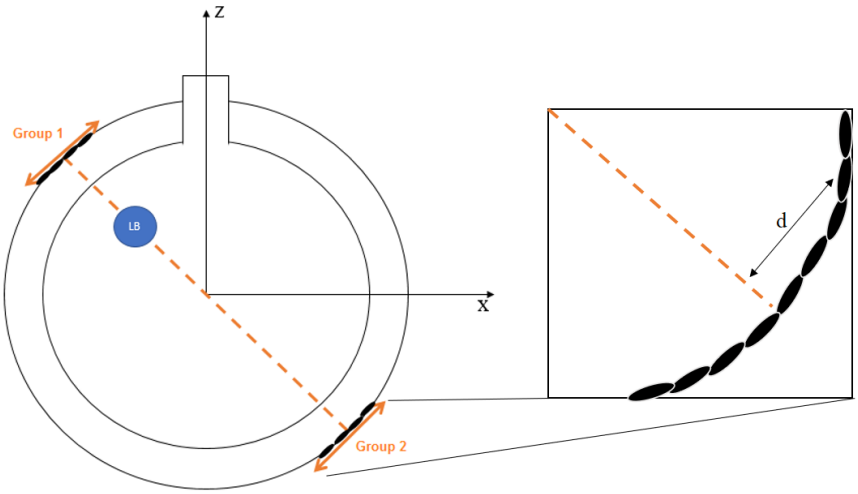

Figure 4.1: Diagonal Scan Analysis illustration, illustrating the laserball placed along one diagonal and the two groups of PMTs at each end of it.

The PMTs outside this distance from the diagonal are not used in the analysis. This PMT cut ensures that, as a first approximation, the incidence angle and the angular distribution of light does not change from PMT to PMT in the group (the photons striking the PMTs travel normal to the acrylic and the tubes). The ratio of occupancies between two opposite PMTs (one in each group) is:

$$\frac{O_1}{O_2} = \frac{N\Omega_1 R_1 T_1 L_1 \epsilon_1 e^{-(d_1^a \alpha_a + d_1^b \alpha_b + d_1^c \alpha_c)}}{N\Omega_2 R_2 T_2 L_2 \epsilon_2 e^{-(d_2^a \alpha_a + d_2^b \alpha_b + d_2^c \alpha_c)}} . \tag{4.2}$$

Because the PMTs are aligned, one can assume that the distance travelled by light in the acrylic and in the external water is the same for each side ($d_1^b = d_2^b$ and $d_1^c = d_2^c$), making the ratio of the last two exponential terms equal to one:

$$\frac{O_1}{O_2} = \frac{N\Omega_1 R_1 T_1 L_1 \epsilon_1 e^{-d_1^a \alpha_a}}{N\Omega_2 R_2 T_2 L_2 \epsilon_2 e^{-d_2^a \alpha_a}} = \frac{N\Omega_1 R_1 T_1 L_1 \epsilon_1}{N\Omega_2 R_2 T_2 L_2 \epsilon_2} e^{-(d_1^a - d_2^a)\alpha_a} . \tag{4.3}$$

[1]The $y = z$ and $y = -z$ diagonals are not used because the y axis is crossed by pipes connected to the AV, affecting the light paths of one of the PMT groups. Other types of scans, like horizontal and vertical, would not be useful because the equator of the AV has different optical properties, ropes attached all around, and because there is the neck on the top of the AV.

The ratio of the occupancies will, therefore, vary exponentially with the difference between the light paths inside the AV for each PMT, with a slope equal to the attenuation coefficient of the medium inside the acrylic vessel (water or scintillator). Because the solid angle and the Fresnel transmission coefficients can be calculated numerically, they can be used to correct the measured occupancy, leaving only, on the right side of the equation, a dependency on the angular response and efficiency of the PMTs and on the laserball light distribution, which can be considered as constants (first approximation).

$$\frac{O_1^{Corr}}{O_2^{Corr}} = \frac{O_1\Omega_2 T_2}{O_2\Omega_1 T_1} = \frac{NR_1L_1\epsilon_1}{NR_2L_2\epsilon_2} e^{-(d_1^a - d_2^a)\alpha_a} \,. \tag{4.4}$$

On the other hand, the product between the two occupancies should be constant. This happens because the multiplication of the exponentials leads to the sum of the distances travelled by light in each medium. The values of these sums give constant values: in the case of the acrylic and the exterior water, it is due to the assumption that light will travel the same distance for each side, and in the case of the interior of the acrylic vessel, the sum will be equal to the diameter of the vessel.

$$O_1^{Corr} O_2^{Corr} = \frac{O_1 O_2}{\Omega_1 T_1 \Omega_2 T_2} = N^2 R_1 L_1 \epsilon_1 R_2 L_2 \epsilon_2 e^{-(d_1^a\alpha_a + d_1^b\alpha_b + d_1^c\alpha_c)} e^{-(d_2^a\alpha_a + d_2^b\alpha_b + d_2^c\alpha_c)} \,. \tag{4.5}$$

The Diagonal Scan Analysis code was tested extensively using a MC set of diagonal laserball runs (Table 4.1), for five wavelengths: 337 nm, 369 nm, 385 nm, 420 nm and 505 nm; and considering the AV filled with water. The code creates groups of PMTs within a certain distance to the diagonal, then it makes pairs of aligned PMTs and calculates their occupancy ratio. For the same laserball position, the weighted arithmetic mean of the occupancy ratio and product are calculated for all pairs. The plot of these values in function of the mean value of the difference between the light path lengths for each PMT pair, $\langle d_1 - d_2 \rangle$, has the expected exponential shape, as can be seen in Figure 4.2. The fit of the data points gives the value of the attenuation length of the medium inside the AV (water in this case).

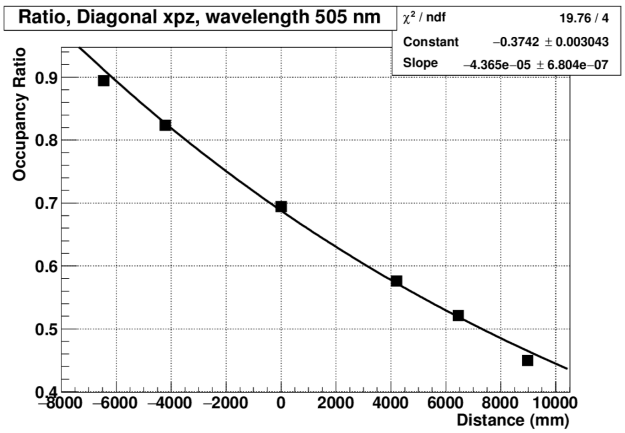

Figure 4.2: Occupancy ratio of PMTs from different runs as a function of the mean distance between their light paths. This was obtained for laserball runs at 505 nm along the $x = z$ axis, and using PMTs at a maximum of 1500 mm from the diagonal.

With the attenuation coefficients obtained from this analysis, several optimization tests were performed in order to choose the optimal value of the maximum distance of the PMTs to the

Table 4.1: List of laserball positions used by the Diagonal Scan Analysis, for the two detector diagonals x=z and x=-z, in mm.

x=z	x=-z
(-1500,0,-1500)	(-1500,0,1500)
(-2300,0,-2300)	(-2300,0,2300)
(-3200,0,-3200)	(1500,0,-1500)
(1500,0,1500)	(2300,0,-2300)
(2300,0,2300)	(3200,0,-3200)
(0,0,0)	(0,0,0)

diagonal, and also the optimal value of tolerance for the PMT shadowing cuts[2]. Figures 4.3 (a) and (b) show the water attenuation coefficients obtained in function of the laserball wavelength for the two different diagonals $x = +z$ and $x = -z$, respectively. The black curve represents the attenuation coefficient values used as the simulation input and the points represent the obtained results for maximum distances to the diagonal of 1000 mm (blue), 1500 mm (green) and 2000 mm (orange). From these results it can be observed and concluded that a maximum distance to the diagonal of 1500 mm reflects quite well the simulation input. Smaller values, for instance 1000 mm, will create smaller groups of PMTs, resulting in smaller statistics and in a worse estimate of the attenuation coefficients.

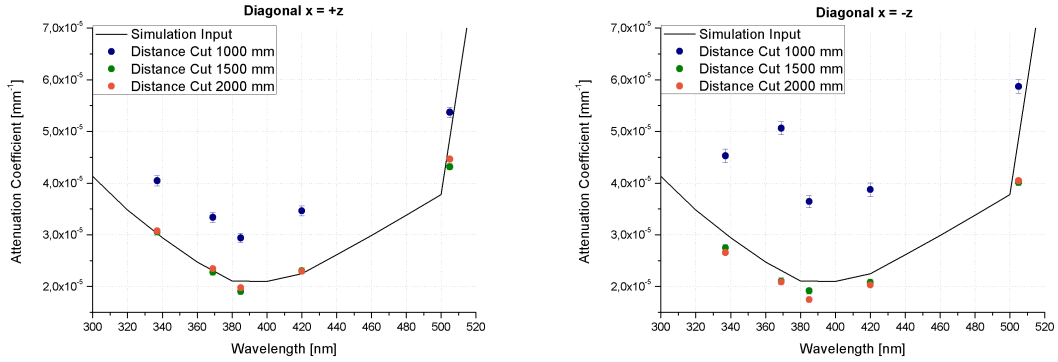

(a) (b)

Figure 4.3: Water attenuation coefficients in function of the wavelength for the diagonal $x = +z$ (a), and for the diagonal $x = -z$ (b), using the solid angle and Fresnel transmission coefficients as occupancy corrections. The black curve represents the attenuation coefficient values used as the simulation input and the points represent the obtained results for maximum distances to the diagonal of 1000 mm (blue), 1500 mm (green) and 2000 mm (orange).

It is also observed that the results between the two diagonals are slightly different. These differences were studied by implementing other corrections to the occupancy in the code, such as correcting by the PMT angular response and by the laserball mask function. The results, for a maximum distance to the diagonal of 1500 mm, with all these corrections are shown in Figure 4.4. It can be seen that the results reproduce well the simulation input. At 420 nm, for example, the relative difference between the $x = z$ and $x = -z$ results and the simulation input are around 15% and 6%, respectively.

[2]As was said previously, shadowed PMTs have smaller occupancies due to detector elements crossing their light paths. The reflections and refractions by these elements are hard to characterize. So, it is preferable to eliminate these PMTs from the analysis. The shadowing tolerance is a value by which the size of the shadowing element is increased, so that a more conservative cut of PMTs is done.

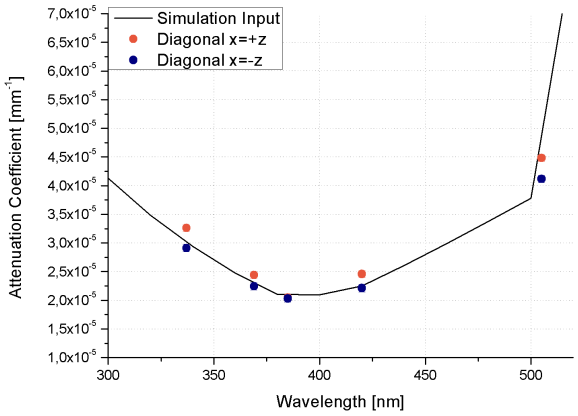

Figure 4.4: Water attenuation coefficients in function of the wavelength from the analysis of the diagonal x = +z (orange) and the diagonal x = -z (blue). These results use the solid angle, the Fresnel transmission coefficients, the PMT angular response and the LB mask function as corrections. The black curve represents the attenuation coefficient values used as the simulation input. The error bars are not visible due to their small size.

4.1.2 Laserball Asymmetry Analysis

The Laserball Asymmetry Analysis (LAA) was developed to characterize the light emission of the laserball, allowing a fast validation of its angular distribution. One of the standard requirements for the Optical Calibration plan is to obtain data with the laserball facing the four cardinal orientations: North (N), West (W), South (S) and East (E), described in Appendix A. This analysis makes use of these runs with different orientations to characterize the laserball asymmetry with the polar angle ϕ. The ratio of occupancies of the same PMT for two runs with the laserball in opposite directions is given by:

$$Ratio = \frac{O_{1j}}{O_{2j}} = \frac{N_1\,\Omega_{1j}\,R_{1j}\,T_{1j}\,L_{1j}\,\epsilon_j\,e^{-(\alpha_a d_a+\alpha_b d_b+\alpha_c d_c)}}{N_2\,\Omega_{2j}\,R_{2j}\,T_{2j}\,L_{2j}\,\epsilon_j\,e^{-(\alpha_a d_a+\alpha_b d_b+\alpha_c d_c)}}\,. \tag{4.6}$$

The exponentials, the solid angle Ω, the Fresnel transmission coefficient T, the PMT angular response R and the PMT efficiencies ϵ are the same for the two runs because the laserball is in the same position and the PMT j is the same for the two orientations. The ratio then becomes:

$$Ratio = \frac{N_1 \times L_{1j}}{N_2 \times L_{2j}} = \frac{N_1 \times L(cos\theta_{LB_j}, \phi_{LB_j} + \Phi_1)}{N_2 \times L(cos\theta_{LB_j}, \phi_{LB_j} + \Phi_2)}\,, \tag{4.7}$$

where Φ_1 and Φ_2 are the relative orientations of the laserball for the two runs. Expanding the angular distribution $L(cos\theta_{LB}, \phi_{LB})$, and using the fact that the laserball mask function, $P_4(cos\theta_{LB_j})$, is the same in the numerator and denominator, the ratio becomes:

$$Ratio = \frac{N_1 \times H(cos\theta_{LB_j}, \phi_{LB_j} + \Phi_1)}{N_2 \times H(cos\theta_{LB_j}, \phi_{LB_j} + \Phi_2)}\,. \tag{4.8}$$

Equation 4.8 shows that this method allows the characterization of the laserball angular distribution. In particular, it is useful to use the sinusoidal model of the angular distribution described in Section 3.2.3. The Laserball Asymmetry Analysis code uses the ratios of occupancies from runs with the laserball facing North over occupancies from runs with the laserball facing South, N/S, and ratios of occupancies from runs with the laserball facing West over occupancies from

runs with the laserball facing East, W/E.

Figure 4.5 shows the results obtained with this analysis, considering the laserball divided into six slices of $cos(\theta_{LB})$ and emitting at a wavelength of 505 nm. In order to validate the results, they were compared with the expected laserball asymmetry, calculated with the light distribution parameters used as the simulation input. The ratio N/S is presented in red squares, the ratio W/E in blue squares and the corresponding expected asymmetries are the lines with the same colour scheme. The ratio of occupancies is shown as a function of the photomultipliers azimuthal angle ϕ_{PMT}.

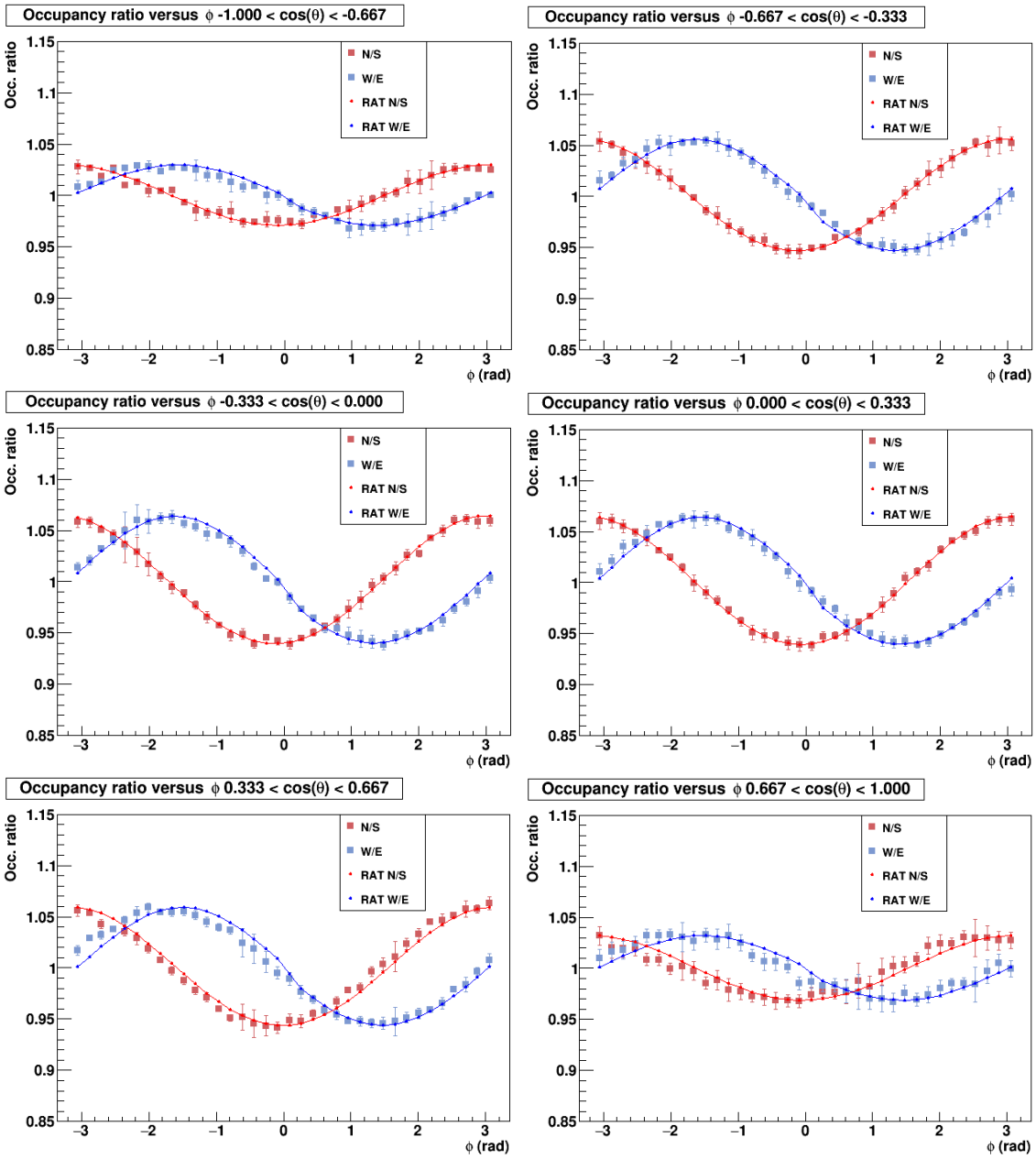

Figure 4.5: Laserball asymmetry in function of the angle ϕ_{PMT} for each of the six cos(θ_{LB}) slices (emitted wavelength of 505 nm). The ratios N/S and W/E are presented, respectively, in red and blue squares. The red and blue lines are the expected ratios from the simulation input.

The ratios have the expected sinusoidal shape from the angular distribution model and show a good agreement with the simulation input. From the results, it can be seen that for very large and

very small values of cos(θ) the laserball asymmetry is smaller than for the remaining slices. The slice -1<cos(θ)<-0.67 represents the bottom of the laserball and the corresponding results show that the intensity of light emitted by this slice is almost the same for the whole ϕ range. The slice 0.67<cos(θ)<1.0, corresponding to the top of the laserball, also shows a small asymmetry with ϕ but, in this case, it is necessary to take into account the shadowing created by the LB mounting hardware, which will affect the occupancy measured by the PMTs in the upper part of the PSUP.

The fact that the results obtained with this analysis showed a good agreement with the expected ratios motivated a step forward in this analysis: the extraction of the two parameters of the sinusoidal angular distribution $H_{sin}(cos\theta_{LB}, \phi_{LB})$, A_k and δ_k, by fitting the results with suitable functions. The fit of the results is described in Appendix B. The parameters from the fit were then compared with the simulation input. Figure 4.6 shows the obtained parameters, for runs with the laserball at 505 nm, as a function of 24 slices of cos(θ). The x-axis goes from slice number 0, corresponding to the cos(θ) range of -1.0 to -0.917, to slice number 23, corresponding to the cos(θ) range of 0.917 to 1.0. The full set of obtained parameters for all wavelengths is shown in Appendix B.

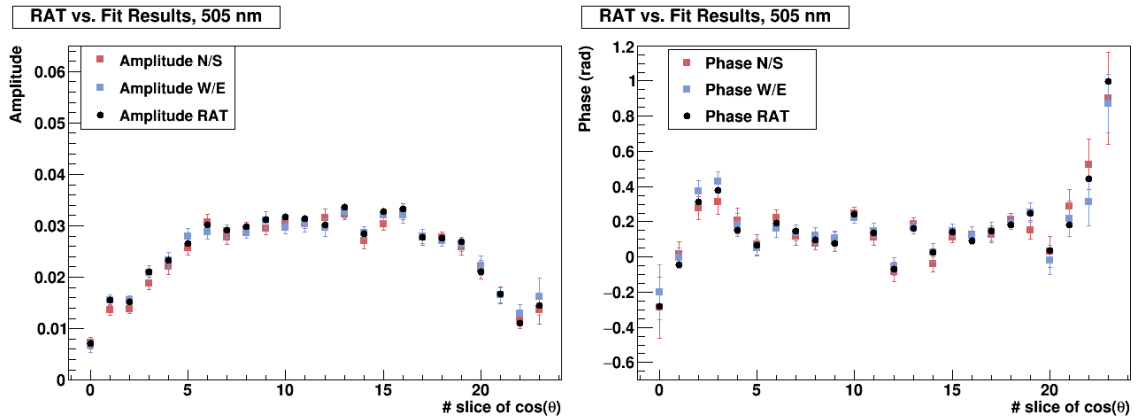

(a) (b)

Figure 4.6: (a) Amplitude and (b) Phase parameters from the N/S (red) and W/E (blue) ratios for each slice of cos(θ) and respective expected parameters from the simulation input.

A good agreement between the parameters obtained for the N/S (in red) and W/E (in blue) fits and the expected ones (in black) are observed. The obtained amplitudes differ from the simulation input by up to 7%, and the phases differ from the simulation input by up to 30%, where the largest differences are in the first and last slices, that correspond to the poles of the laserball. The first and last slices have smaller amplitude parameters than the remaining, meaning that for those slices the intensity of the light emitted will not vary that much with ϕ in comparison with other parts of the laserball. Besides, the phases of these slices show larger error bars, which are consistent with the low PMT statistics. This is caused by shadowing of the laserball mounting hardware in the case of the last slice (region with cos(θ) = 1) and due to the small amount of PMTs in the bottom of the detector in the case of the first slice (region with cos(θ) = -1).

The good performance and results of the Laserball Asymmetry Analysis led to the use of the obtained parameters as an input to OCA. This upgrade to OCA reduced the parameter space of the fit, decreasing its overall complexity. The number of free parameters in the fit went from around 190 per wavelength to ~140 parameters per wavelength, a reduction of almost 30%. OCA was tested with MC data, using the light distribution parameters of the LAA as input, and it was

verified that the computational time needed for the fit went from 75 minutes and 25 seconds to 68 minutes and 17 seconds, a reduction of the order of almost 10%.

4.2 OCA Fit with Monte Carlo and SNO Data

SNO+ has not collected yet all the laserball data required to perform a full Optical Calibration analysis. In the mean time, the OCA software has been tested and validated using both MC data and SNO laserball data. This has allowed to identify and correct problems, as well as to optimize its performance. This Section presents the results extracted by OCA for two sets of laserball scans:

- SNO Laserball Scan from October 2003, data in D2O

  Laser wavelengths [nm]: 337, 369, 385, 420, 505 and 620.

- SNO+ MC Laserball Scan from October 2015, data in H2O

  Laser wavelengths [nm]: 337, 369, 385, 420 and 505.

All the results are accompanied by their respective error bars, which include the statistical and the systematic uncertainties, both calculated by OCA. For more details about the systematic uncertainties, please refer to [46, 51, 50].

4.2.1 Media Attenuation Coefficients

The fitted values of the attenuation coefficients for the SNO heavy water and SNO+ MC light water are presented in Figures 4.7 and 4.8. Both coefficients are compared with the attenuation coefficient values calculated from Rayleigh scattering and absorption coefficients used by the SNO+ software, using Equation 3.6. The coefficients used by the SNO+ software are an average of the measurements made during the SNO experiment. Both the heavy water and light water attenuation coefficients are consistent with the values that are currently being used by the SNO+ software. The relative difference between the water attenuation results and the simulation input quantifies the precision of the OCA fit. At 420 nm, the relative difference between the fitted attenuation coefficient and the simulation input is 3%.

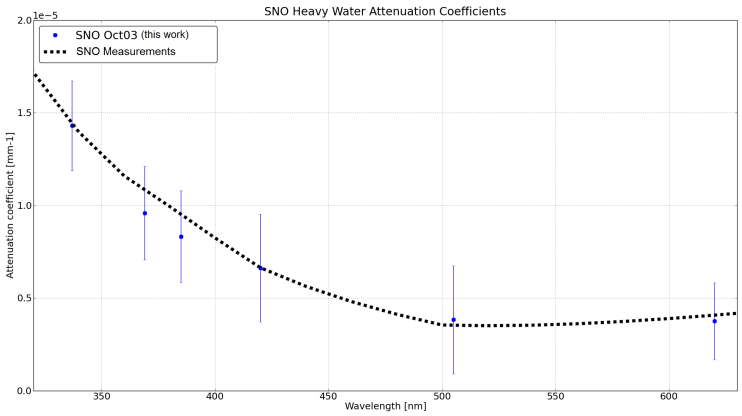

Figure 4.7: Fitted heavy water attenuation coefficients from the SNO data as a function of the laserball dye wavelength.

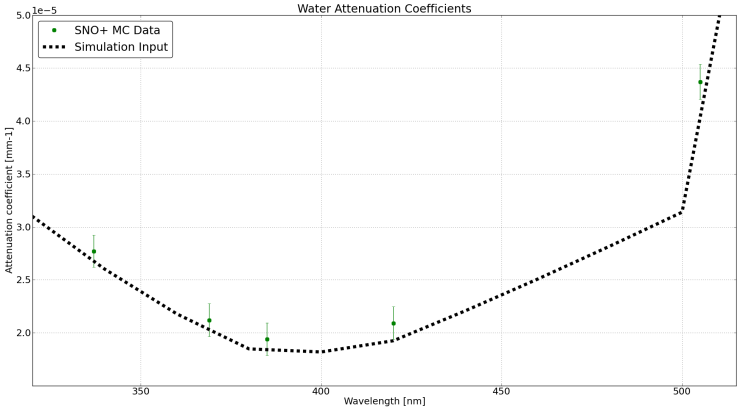

Figure 4.8: Fitted water attenuation coefficients from the SNO+ MC data as a function of the laserball dye wavelength.

The fitted external water attenuation coefficients for both laserball scans are shown in Figure 4.9. The large uncertainties reflect the narrow range of path lengths in the region between the AV and the PMTs. It is observed that the values coming from the SNO+ MC data are in very good agreement with the default values, used as the simulation input. This agreement validates the performance of the fit. The values from the SNO data are slightly deviated from the default values, however they agree within their uncertainties.

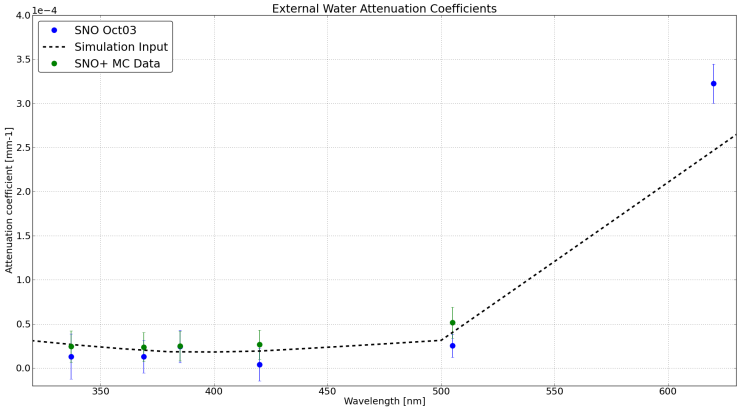

Figure 4.9: Fitted external water attenuation coefficients from the SNO and SNO+ MC data as a function of the laserball dye wavelength.

4.2.2 PMT Angular Response

The fitted relative PMT angular responses obtained from the SNO and SNO+ MC data are presented in Figures 4.10 and 4.11, for the available wavelengths. In both cases, the angular response varies with the light incident angle and with the wavelength. In the incident angle range between 0 and 30 degrees, the relative PMT angular response has a near-linear increase, with variations at higher incident angles. In the case of the SNO data, for incidence angles larger than $\sim$ 35 degrees, the response starts slowly decreasing. For the SNO+ MC data, the decrease is more significant for angles larger than $\sim$ 27 degrees.

The decrease of the PMT angular response at higher angles has to do with the intrinsic geometry of the PMT reflectors. There will be a limiting angle above which the light entering the PMT

and reflector assembly will be reflected back out, reducing the PMT response.

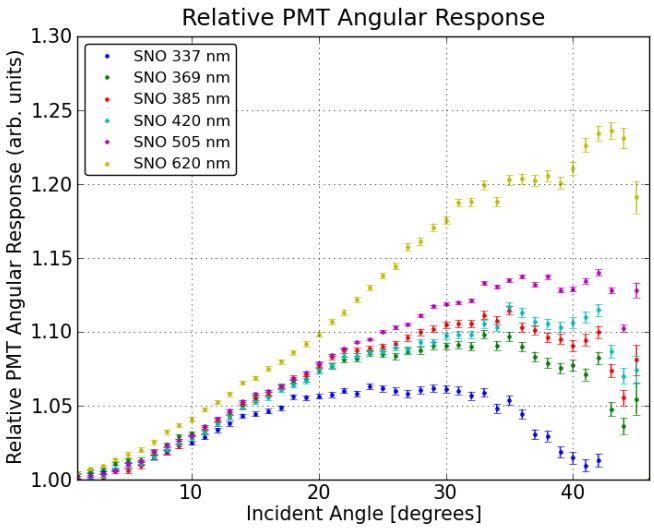

Figure 4.10: Fitted relative PMT angular response from the SNO data as a function of light incident angle, for the six available wavelengths.

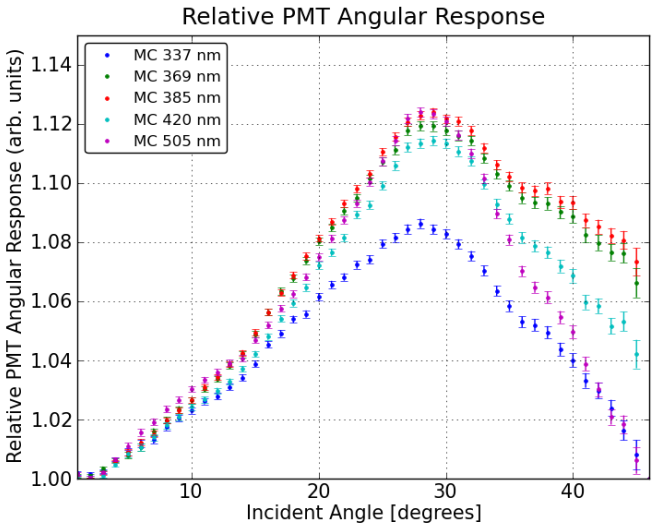

Figure 4.11: Fitted relative PMT angular response from the SNO+ MC data as a function of light incident angle, for the five simulated wavelengths.

4.2.3 Laserball Light Distribution

As discussed in Section 3.2.3, the total light distribution of the laserball, $L(cos\theta_{LB}, \phi_{LB})$, is given by the convolution of the angular distribution $H(cos\theta_{LB}, \phi_{LB})$ with the mask function $P_4(cos\theta_{LB})$.

The laserball mask function, $P_4(cos\theta_{LB})$, which describes the relative intensity of the laserball with θ_{LB}, was obtained for each wavelength of the two scans. The results from the SNO data are shown in Figure 4.12 (a) and the results from the SNO+ MC data are in Figure 4.12 (b). In both cases, the intensity decreases at high $cos\theta_{LB}$, as a result of the shadowing created by the mounting hardware.

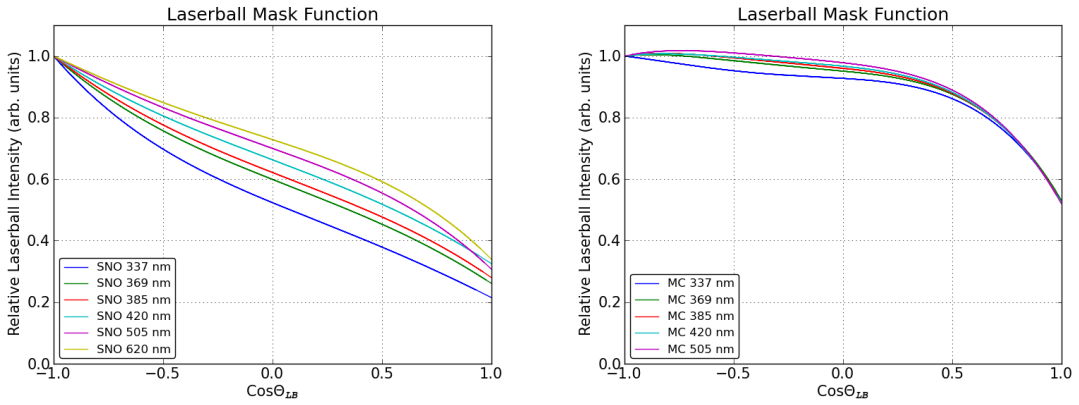

Figure 4.12: (a) Fitted laserball mask function from the (a) SNO data and the (b) SNO+ MC data as a function of $cos\theta_{LB}$.

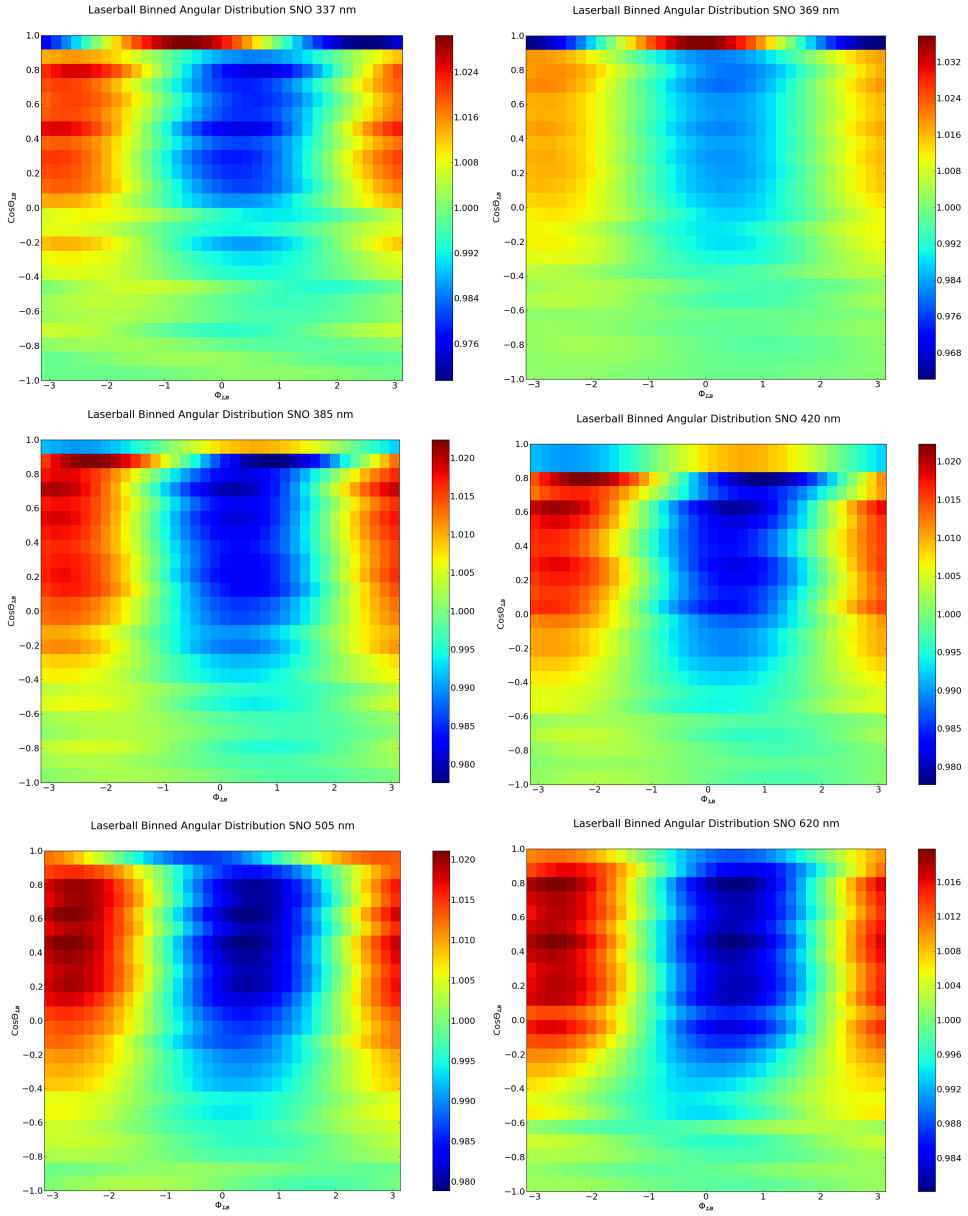

Figure 4.13: Fitted Laserball angular distributions from the SNO data. The distributions were fitted using the sinusoidal model.

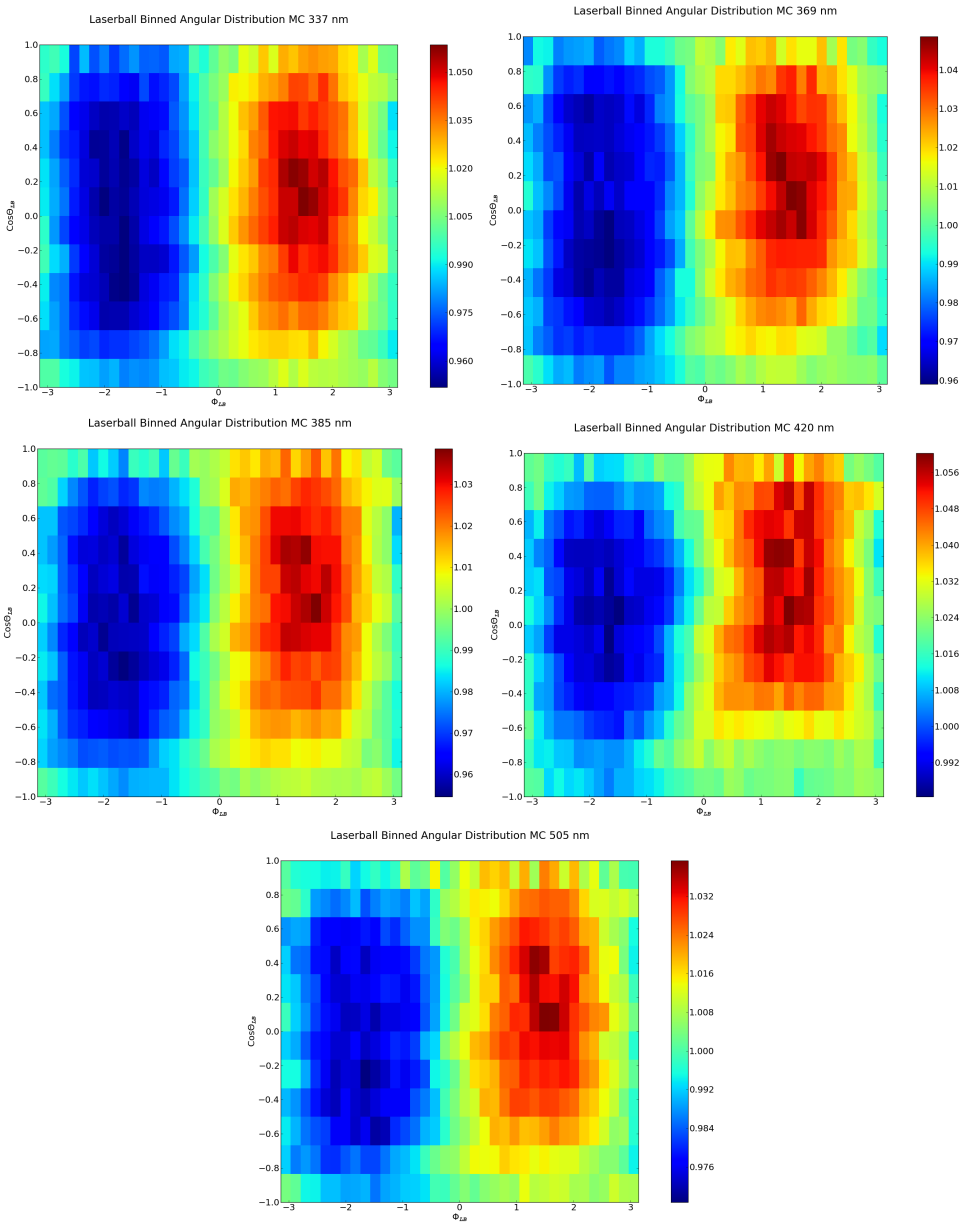

Figure 4.14: Fitted laserball angular distributions from the SNO+ MC data. The distributions were fitted using the sinusoidal model.

The fitted laserball angular distributions are presented in Figures 4.13 and 4.14, for all the wavelengths of each scan. The sinusoidal pattern in the light distribution with the polar angle ϕ_{LB} is clearly visible. In the results from the SNO data, the variation in the light intensity is of the order of 2-3%, whereas for the MC data it is of the order of 4-5%. Looking at Figure 4.13 is can be observed that, in October 2003, the bottom of the laserball had an homogeneous emission of light, with the anisotropies starting a little below its equator. On the other hand, the SNO+ MC results in 4.14, based on the laserball scan of 2006, show that the whole laserball surface was emitting anisotropically.

It is important to note that the angular distributions from the SNO data set have an artefact from the fitting procedure at $cos\theta_{LB} = 1$, because in this region the anisotropy is discontinuous [50].

The ability of the OCA fit to correctly characterize the laserball light distribution depends on

the inclusion of runs with the laserball in the center facing different directions. Using these runs allows to break possible correlations between the angular distribution and the mask function.

4.3 SNO+ Water Phase Laserball Data

The laserball was deployed for the first time in the SNO+ detector at the end of April 2017. The first runs obtained were not perfect: unfortunately, there were some issues with the manipulator hardware responsible for moving the laserball in x and y, and the laserball could only be moved up and down the z axis. Also, it was the first time since SNO that the laser was operated and there were some instabilities with the laser intensity that have been fixed in the meantime.

Even though the first laserball runs do not have the quality or the positions necessary for a full optical calibration, they are of extreme importance to check the status and stability of the detector and the laserball hardware, as well as for testing all the software tools that are needed to prepare the raw data to be analysed by OCA.

4.3.1 Stability of the Laser

One of the most basic checks that can be performed regarding the laserball data is to see if there are instabilities in the laser hardware. This is done by monitoring the evolution of the total number of hits registered by the PMTs throughout the run length. If the laser hardware is working correctly, the total number of hits should be constant. However, in some of the first laserball runs, this was not observed.

One example is shown in Figure 4.15, for an hour-long central laserball run at 420 nm. It shows the total number of hits detected as a function of the laserball event IDs, that are arranged in chronological order. Besides an overall decrease on the number of hits throughout the run length, one of the most visible features are three abrupt dips where the number of hits detected decreased considerably.

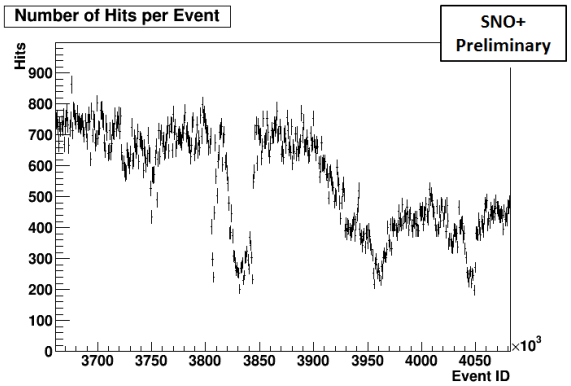

Figure 4.15: Total number of hits detected by the PMTs as a function of the laserball event IDs.

During the acquisition of this run, the calibration crew operating the laserball found problems with the photodiode responsible for producing the signal to trigger the data acquisition system. It was possible to confirm that this problem was causing the decrease in the number of detected hits by looking at the data, in particular the PMT hit time and its time of flight. The time of flight, t_{TOF}, is a constant for each PMT in a run: it is the average time that light takes to travel from the laserball to the PMT. The PMT hit time, t_{PMT}, is the time at which the PMT registered a

hit, relative to the time at which the trigger signal reached the data acquisition system. These two quantities are related to the instantaneous time of the event, $t_{residual}$, and the global time offset t_0, which is the time at which the laserball trigger signal arrives at the data acquisition system:

$$t_{residual} + t_0 = \frac{1}{N_{PMTs}} \sum_{j=0}^{N_{PMTs}} (t_{PMT,j} - t_{TOF,j}) \, . \tag{4.9}$$

$t_{residual} + t_0$ should be constant throughout a laserball run. Figure 4.16 shows that this was not the case during the run discussed. Throughout the run length, there were variations in the PMT hit times that, because the time of the laserball pulses and each PMT t_{TOF} are constants, were due to variations in the laserball trigger time. By comparing Figures 4.15 and 4.16 it is clearly visible that both exhibit the same pattern throughout the run length, leading to the conclusion that the misalignment of the laserball light with the trigger resulted in a smaller number of hits registered by the PMTs.

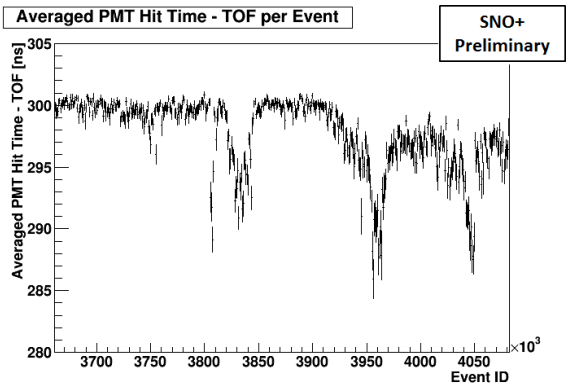

Figure 4.16: Averaged difference between the PMT time and time of flight as a function of the laserball event IDs.

These type of checks using the laserball data are very important and useful to give feedback to the calibration crew, so that problems like this can be dealt with and fixed more easily. After fixing the issues with the photodiode close to the laser, more stable runs were obtained. Figures 4.17 (a) and (b) show an example of an ∼1 hour-long stable run with the laserball at the center of the detector. It can be seen that, as expected, the number of detected hits and the times are constant throughout the run length.

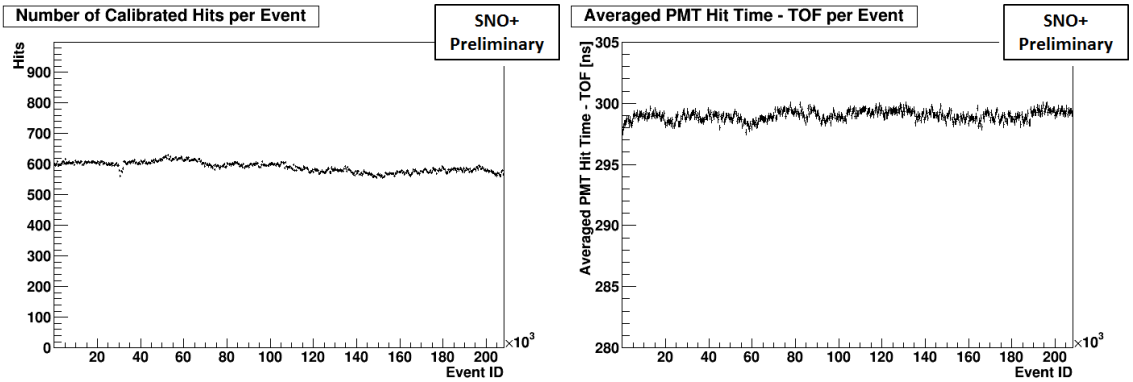

(a) (b)

Figure 4.17: (a) Total number of hits and (b) averaged difference between the PMT time and time of flight per event for a stable laserball run.

4.3.2 Data Processing and Quality

OCA and the optics validation tools do not use the raw data coming directly from the detector. The raw data has to be processed into *Summary Optical Calibration* (SOC) files. The SOC files contain the TAC (Time-Amplitude Conversion) and the charge data from the detector for every PMT hit registered during the run, ordered by PMT ID, as well as the source wavelength and position coming from the manipulator hardware. Furthermore, they include the time of flight from the source to each PMT, calculated numerically during the processing, and the occupancy of each PMT, obtained from the integration of the prompt peak of each individual TAC. During the processing, a dedicated algorithm, based on a χ^2 minimisation of the PMT hit time, reconstructs the source position based on the data. Comparing the reconstructed position with the real one coming from the manipulator is useful to both validate the performance of the algorithm as well as to identify eventual problems with the data.

Due to some issues with the manipulator hardware, it has not been possible yet to place the laserball in positions other that along the z axis. However, there are some runs with the laserball in different positions along this axis, and at a few different wavelengths. To analyse the runs, only the Normal type of PMTs (inward looking and with high gains) were selected. The following Figures and discussion are focused on two runs:

- Run 17375, laser at 505 nm, laserball position (0.0, -254.0, 25.0) mm
- Run 102564, laser at 337 nm, laserball position (0.0, -254.0, 5525.0) mm

The hole through which the laserball was inserted is 25.4 cm away from the center in the negative y axis, and because of the issues of the side ropes that move the laserball in x and y, it was not possible to place the laserball exactly in the center. The 2.5 cm in the z coordinate are due to a displacement of the center of the AV relative to the center of the PSUP.

Figure 4.18 shows the TAC histograms for all PMTs in the two runs. The peak due to prompt light is clearly visible for run 17375, centered around 160 ns. For run 102564 it is not possible to identify the prompt peak because the laserball is not in the center, therefore light will arrive at different times to each PMT position. Figures 4.19 and 4.20 show the prompt peak centroid and its width[3] for both runs as a function of PMT ID. It can be observed that, in the case of run 17375 with the laserball in the center, both values are consistent for all PMTs. However, in the case of run 102564, the PMTs have different values for the prompt peak centroid because the laserball is not in the center. The pattern observed is due to the arrangement of the PMTs in the detector.

The width of the prompt peak of each PMT is dominated by the *transit time spread*, which is the distribution of the times necessary for a photon to be converted into an electrical signal, which is $\sim$1.6 ns. A uniform width near this value across all PMTs for a central laserball run, like it is observed in Figure 4.20 (a), shows that the performance of the PMTs was as expected.

Integrating the TAC prompt peak for each PMT in a window of $\pm$4 ns around the peak centroid gives the occupancy of the PMT. The distributions of occupancies for these two runs are shown in Figure 4.21. It is possible to see that Figure 4.21 (a) presents a noticeable tail towards low occupancy values, that is mostly due to the lower occupancy measured by PMTs that are shadowed.

Figure 4.22 shows the calculated time of flight for each PMT. For run 17375, the values are almost uniform across all PMTs because, with the laserball placed close to the center of the de-

[3]These two quantities are calculated using a sliding-window method. It searches for the prompt peak by moving the 8 ns wide time window along the PMT time residual distribution until it finds a maximal number of hits.

tector, all photons travel approximately the same distance from the source to the PMTs, and thus the same amount of time. However, because the laserball was not exactly in the center, a small oscillatory-like pattern is observed in this plot. For run 102564, it is possible to see that the PMTs have a range of time of flight values between 15 ns and 75 ns. PMTs with a smaller value of time of flight are closer to the laserball, whereas the ones with a larger value are farther away from it.

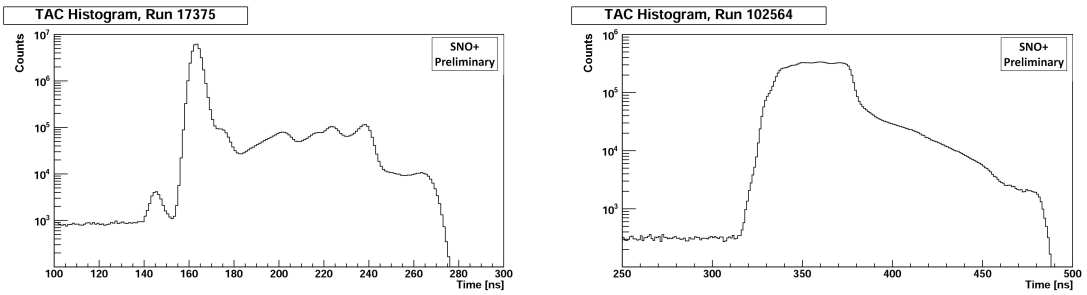

(a) (b)

Figure 4.18: TAC Histograms for runs (a) 17375 and (b) 102564.

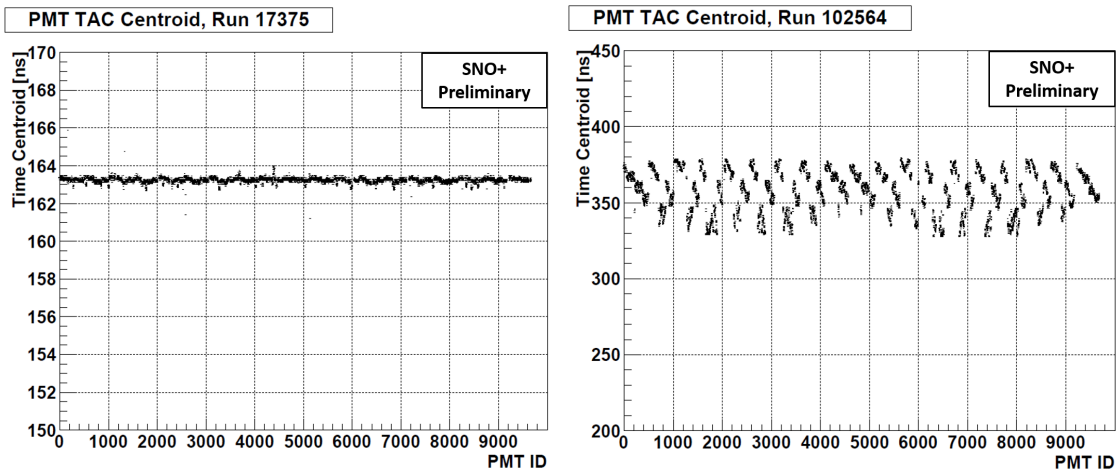

(a) (b)

Figure 4.19: Prompt peak centroid as a function of PMT ID for runs (a) 17375 and (b) 102564.

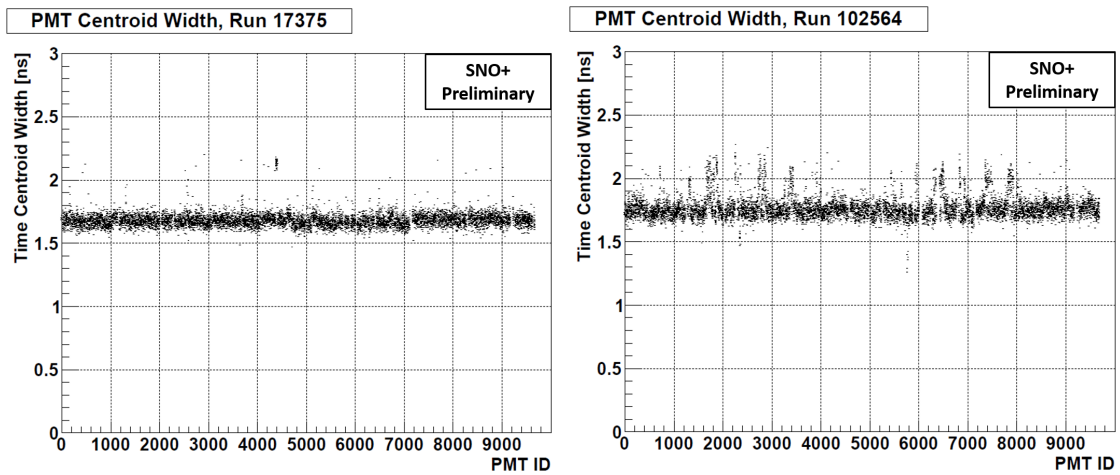

(a) (b)

Figure 4.20: Prompt peak width as a function of PMT ID for runs (a) 17375 and (b) 102564.

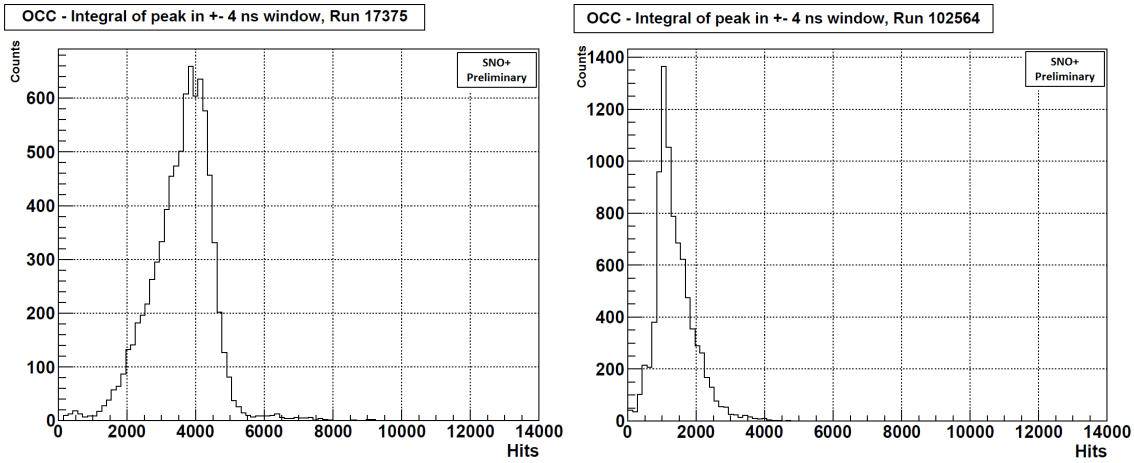

(a) (b)

Figure 4.21: Occupancy histograms for runs (a) 17375 and (b) 102564.

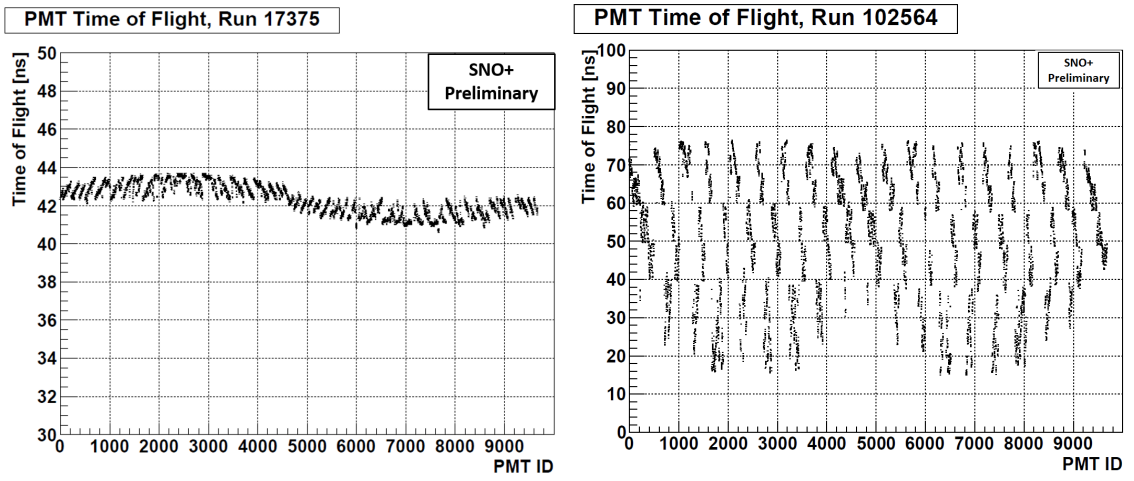

(a) (b)

Figure 4.22: Time of Flight of each PMT for runs (a) 17375 and (b) 102564.

Table 4.2 shows the results of the reconstructed laserball position, compared with the real position from the manipulator system. Run 17375 has reconstructed x and z coordinates that are in agreement with the real ones. The y coordinate is 3 cm away from the real one. The reconstructed laserball position for Run 102564 has a large difference from the real position, specially in the z coordinate, which is smaller by almost 1 meter. The y coordinate also shows an offset of 3 cm and x has an offset of 1 cm. Although the laserball position is harder to fit for positions far from the center, a difference of 1 meter between the fitted and real position suggests a possible problem with the fit algorithm. There is ongoing work to identify and understand possible issues with the laserball position fit for runs with the laserball away from the center. Besides, a full validation of the position fit requires more runs with the laserball in other positions.

Table 4.2: Reconstructed and manipulator laserball positions from the SOC files.

Run	Manipulator Position [mm]	Reconstructed Position [mm]	Statistical Uncertainty [mm]
17375	(0.0, -254.0, 25.0)	(0.25, -226.06, 23.40)	$\pm$ 4
102564	(0.0, -254.0, 5525.0)	(11.26, -224.37, 4385.18)	$\pm$ 5

Performing these checks to the laserball runs is, as shown, very important to ensure that only good quality data, *i.e.* with a stable detector and laserball, is used to perform the Optical Calibration. When the full set of optical calibration runs is obtained, these data quality checks are the first step towards a precise characterization of the optical properties of the SNO+ detector.

4.3.3 Shadowing Effects in the Detector

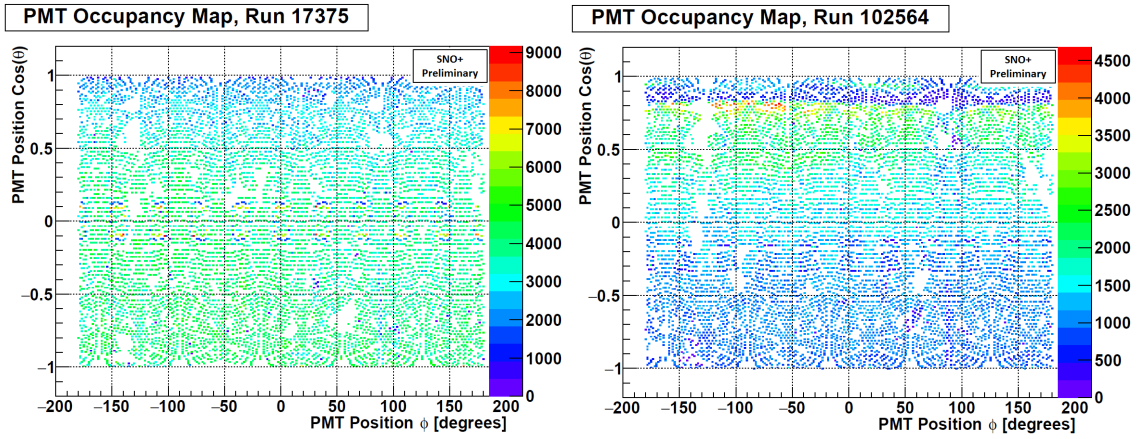

(a) (b)

Figure 4.23: PMT occupancy maps for runs (a) 17375 and (b) 102564.

Figure 4.23 shows PMT occupancy maps for the two laserball runs 17375 and 102564. Occupancy maps are a very useful tool to identify PMTs shadowed by detector elements, as well as to identify spatially PMTs with, for example, low occupancy that could be related to electronics problems. Figures 4.23 (a) and (b) give an insight of the shadowing elements inside the detector from the perspective of a run with the laserball in the center and a run with a laserball on the top of the PSUP, respectively.

Looking at Figure 4.23 (a), it is possible to observe a pattern of circles of PMTs with lower occupancy around the equator of the PSUP, $cos(\theta) = 0$. These are due to the belly plates where the ropes that hold the AV in place are attached. Inside the circles of low occupancy, some PMTs have very high occupancies that are due to refractions caused by the shape of the belly plates. It can also be observed that the PMTs on the top ($cos(\theta) = +1$) of the PSUP have a smaller occupancy than the ones on the bottom ($cos(\theta) = -1$), mostly due to the hold-down ropes.

Figure 4.23 (b) shows that the PMTs in the upper hemisphere have larger occupancies that the ones in the lower hemisphere, which is consistent with the laserball placed at an high z position. Another observation is that, in the region of $\phi = 90$ degrees, there are PMTs with lower occupancy due to pipes connected to the AV. Finally, around ($cos(\theta) = +0.9$), there is a band of shadowed PMTs due to the *neck boss* of the AV, which is the part connecting the neck to the acrylic vessel.

The Occupancy-Ratio method used by OCA, described in Section 3.3, requires a central laserball run to normalize the measured occupancies of a given run *i*. PMTs that are shadowed in the central run are eliminated from the fit as well as PMTs that are shadowed in run *i*. A PMT that is shadowed in the central run but not in run *i* is not going to be used in the analysis because it cannot be normalised. This reduces significantly the number of data points available for the fit, specially for laserball runs far from the center.

A possibility to reduce the number of data points that are thrown away from OCA due to

shadowing would be by combining two laserball runs, one central and other slightly deviated from the center, and use the combination of the two in the Occupancy-Ratio method normalization. To see what combination of laserball positions would allow to reduce the percentage of shadowing, three tests were done by combining a central laserball run with a run with the laserball along one of the three axis: *x*, *y*, *z*. Figures 4.24 (a), (b) and (c) show the results obtained. They show the percentage of shadowing in the detector for the combination of a central run with a run along each axis, as a function of the coordinate on the corresponding axis. PMTs that are shadowed in both runs are excluded, whereas PMTs that are shadowed in one run but not in the other are tagged as not shadowed.

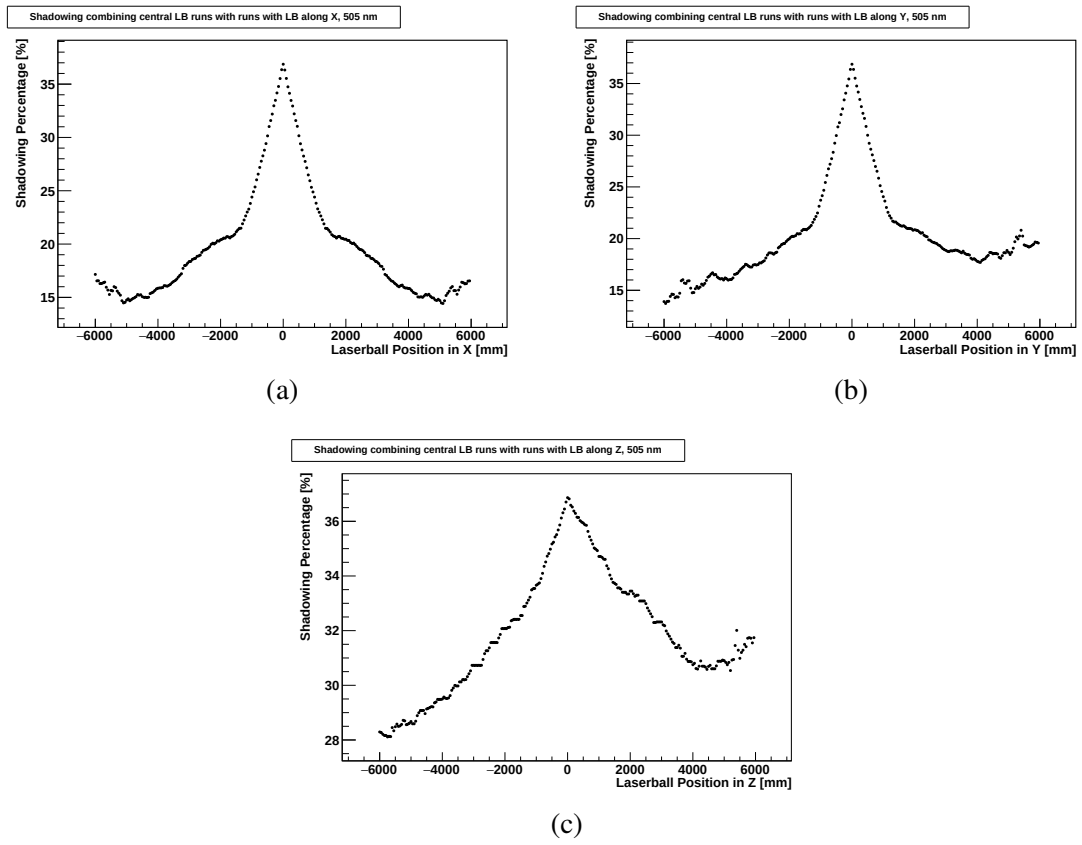

Figure 4.24: Percentage of shadowing in the detector for the combination of a central run with a run along along (a) the *x* axis, (b) the *y* axis and (c) the *z* axis, as a function of the coordinate on the corresponding axis.

It was concluded from this study that the shadowing percentage can be reduced when combining a central laserball run with a second with the laserball along the *x* axis. Having a second run with the laserball in ($\pm$1400, 0, 0) mm, which is still fairly close to the center, already helps reducing the overall shadowing percentage from $\sim$37% to 22%, which is closer to the value of 20% shadowing that the SNO experiment had. Runs with positions along the *y* axis are not able to fully reduce the shadowing contribution of the AV pipes, which is visible in the positive *y* side of Figure 4.24 (b).

Chapter 5

$0\nu\beta\beta$-Decay Sensitivity Studies

The SNO+ experiment main physics goal is the search for the $0\nu\beta\beta$-decay of the ^{130}Te isotope. When searching for the $0\nu\beta\beta$ peak around the Q-value of the decay, one of the main challenges will be to separate it from the intrinsic background induced by the tail of the $2\nu\beta\beta$-decay energy spectrum. This ability depends mostly on the energy resolution in the peak region, that is affected by the optical parameters, such as the attenuations and PMT angular responses.

Using wrong optical parameters for the physics analysis will make it difficult to observe a possible $0\nu\beta\beta$ peak and will affect the measurements of its half-life.

The present Chapter will discuss the effects of the PMT angular response and the scintillator attenuation on the energy resolution and scale of the $0\nu\beta\beta$-decay spectrum, as well as on the determination of its half-life. For simplicity, all the calculations throughout this Chapter assume "zero background" conditions.

5.1 Sensitivity to the $0\nu\beta\beta$ and $2\nu\beta\beta$-Decays

In the Te-Loading Phase of the SNO+ experiment, 0.5% loading by weight of natural tellurium will be added to the 780 tonnes of liquid scintillator inside the detector for the search of the $0\nu\beta\beta$-decay of ^{130}Te, corresponding to a total mass of natural tellurium of 3900 kg.

The 780 tonnes of liquid scintillator are distributed in the acrylic vessel and its neck. However, the physics searches only consider the amount inside the AV for the analysis, that corresponds to $\sim$770 tonnes of liquid scintillator with 3850 kg of natural tellurium[1].

^{130}Te has a natural abundance of 34.08%. Therefore, the amount of ^{130}Te loaded into the scintillator volume inside the AV is:

$$\begin{aligned} m(^{130}\text{Te in the AV}) &= 0.3408 \times m(\text{Te}) \\ &= 0.3408 \times 3850 \text{ kg} \\ &= 1312.08 \text{ kg} . \end{aligned} \tag{5.1}$$

The searches for the $0\nu\beta\beta$-decay will use a fiducial volume of 20%, meaning that the events happening beyond a radius R larger than 3.5 meters from the center of the AV are excluded. This

[1]These values were calculated by knowing the radius of the AV, 6 m, from which it was possible to calculate its volume, and by knowing the density of the liquid scintillator, $\rho = 0.863 - 5.88 \times 10^{-4} T$ (g/cm^3), where T is the temperature [55]. For this calculation, T was considered to be around 12^{o}C.

cut is used mostly to reduce the contribution from external backgrounds to the energy spectrum. The 20% FV will include a mass of ^{130}Te of:

$$\begin{aligned} m(^{130}\text{Te in 20\% FV}) &= 0.2 \times m(^{130}\text{Te in the AV}) \\ &= 0.2 \times 1312.08 \text{ kg} \\ &= 262.416 \text{ kg} , \end{aligned} \tag{5.2}$$

corresponding to a number of ^{130}Te nuclei, N_0, of:

$$\begin{aligned} N_0 = \frac{m(^{130}\text{Te in 20\% FV})}{m(^{130}\text{Te nucleus})} &= \frac{m(^{130}\text{Te in 20\% FV})}{(^{130}\text{Te Isotopic Mass}) \cdot 1.66054 \times 10^{-27} \text{ kg}} \\ &= \frac{262.416 \text{ kg}}{129.9062244 \cdot 1.66054 \times 10^{-27} \text{ kg}} \\ &= 1.216497 \times 10^{27} \text{ nuclei} . \end{aligned} \tag{5.3}$$

The number of ^{130}Te $2\nu\beta\beta$-decay events can be easily calculated because the half-life of this process has been measured experimentally [28]:

$$T_{2\nu}^{1/2} = (8.2 \pm 0.2\,(\text{stat}) \pm 0.6\,(\text{syst})) \times 10^{20} \text{ years} . \tag{5.4}$$

After t years of the beginning of the Te-loading phase, the number of $2\nu\beta\beta$ events is given by:

$$N^{2\nu\beta\beta}(t) = N_0 - N(t) , \tag{5.5}$$

where $N(t)$ is the number of nuclei that remain in the scintillator:

$$N(t) = N_0 exp(-t/\tau_{2\nu}) , \tag{5.6}$$

with $\tau^{2\nu} = T_{2\nu}^{1/2}/ln(2) = 1.183 \times 10^{21}$ years. In the limit where $t/\tau_{2\nu}$ tends to zero, the exponential in N(t) can be expanded as $exp(-t/\tau_{2\nu}) \approx 1 - \frac{t}{\tau_{2\nu}}$. With this approximation,

$$\begin{aligned} N^{2\nu\beta\beta}(t) &= N_0 - N(t) \\ &= N_0 - N_0 exp(-t/\tau_{2\nu}) \\ &= N_0(1 - exp(-t/\tau_{2\nu})) \\ &\approx N_0 \left(1 - 1 + \frac{t}{\tau_{2\nu}}\right) \\ &= N_0 \frac{t}{\tau_{2\nu}} . \end{aligned} \tag{5.7}$$

Table 5.1 shows the number of expected $2\nu\beta\beta$ events throughout the duration of the Te-loading phase of the SNO+ experiment.

Table 5.1: Expected number of $2\nu\beta\beta$-decay events in SNO+ in a 20% Fiducial Volume.

t	1 year	2 years	3 years	4 years	5 years
$N^{2\nu}$(t) events in 20% FV	1028315	2056630	3084945	4113260	5141575

The number of expected $0\nu\beta\beta$-decay events during this phase of the experiment depends on the process half-life, given by Equation 1.21:

$$N^{0\nu\beta\beta}(t) = N_0\, t\, ln(2)\, G_{0\nu}|\mathcal{M}_{0\nu}|^2 \left|\frac{m_{\beta\beta}}{m_e}\right|^2, \tag{5.8}$$

In the expression, the main unknown is the effective Majorana mass of the neutrinos, given by Equation 1.20. The phase space factor $G_{0\nu}$ and the nuclear matrix element $\mathcal{M}$ are obtained from the theory. The phase space factor has a value of $G_{0\nu} = 1.41 \times 10^{-14}\ y^{-1}$ for the ^{130}Te $0\nu\beta\beta$-decay [56]. In the case of the NMEs, there are several models for their calculation, each giving slightly different values. Table 5.2 lists some of the most used models, as well as the values that they predict for the NME of the ^{130}Te decay into two light Majorana neutrinos[2].

Table 5.2: Nuclear models used for the NME calculations of the ^{130}Te $0\nu\beta\beta$-decay, as well as their predictions for $\mathcal{M}$.

Nuclear Model	$\mathcal{M}$
IBM-2, Interacting Boson Model	4.03 [57]
ISM, Interacting Shell Model	2.06 [58]
QRPA, Quasiparticle Random Phase Approximation	3.94 [59]
PHFB, Projected Hartree-Fock-Bogoliubov Method	3.95 [60]
EDF, Energy Density Functional Method	4.98 [61]

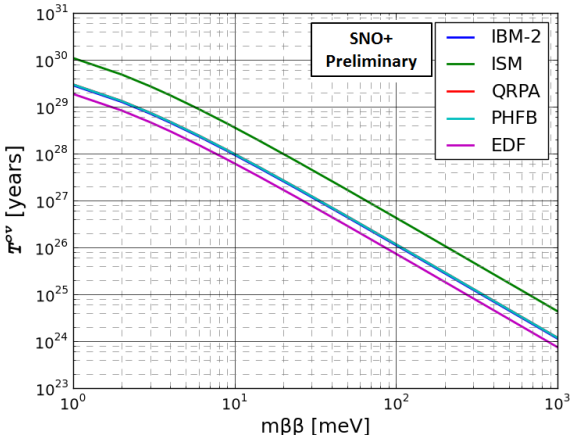

Figure 5.1: $0\nu\beta\beta$ half-life in function of the effective Majorana neutrino mass, for the five main models used for the NMEs calculations.

Figure 5.1 shows the half-life $T_{0\nu}^{1/2}$ of the ^{130}Te $0\nu\beta\beta$-decay, calculated using Equation 1.21, as a function of the effective Majorana neutrino mass, for the 5 different NMEs. It can be seen that, for the same effective mass, the different NMEs give different values for the half-life. Also, a smaller effective Majorana mass will result in a larger value for the half-life.

Figure 5.2 shows the expected number of $0\nu\beta\beta$-decay events as a function of $m_{\beta\beta}$, calculated using Equation 5.8, considering a live time of the detector of five years and 20% FV, as well as assuming no background. The red line represents the limit of one event after five years of detector exposure. It can be seen that for the same number of detected events, the different NMEs will result in different estimates for the effective Majorana mass.

[2]The values displayed on the table correspond to the axial-vector coupling constant g_A = 1.269.

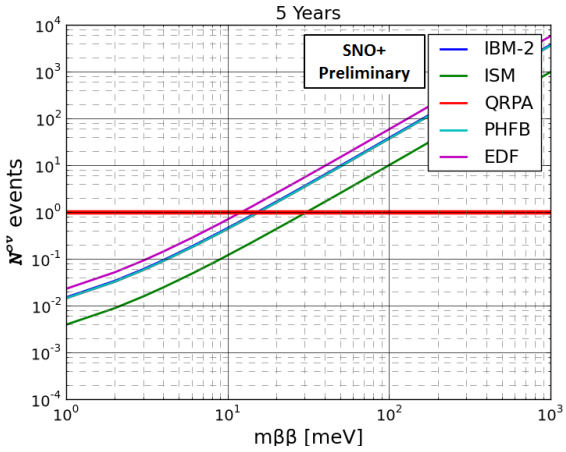

Figure 5.2: Expected number of $0\nu\beta\beta$-decay events, after 5 years of data taking in SNO+, in 20% FV, as a function of the effective Majorana neutrino mass, for the five main NME models.

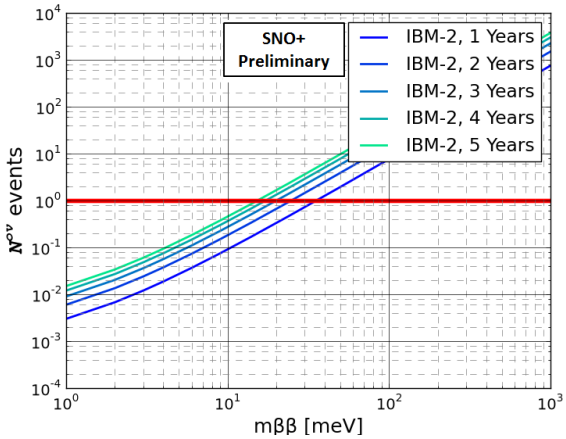

Figure 5.3: Expected number of $0\nu\beta\beta$-decay events in SNO+, in 20% FV, as a function of the effective Majorana neutrino mass, using the IBM-2 nuclear matrix element, for different detector live times.

The most commonly nuclear matrix element model used is the IBM-2. Figure 5.3 shows the evolution with time of the sensitivity of the SNO+ experiment to the effective Majorana mass for this NME. It is observed that the more the experiment collects data, the smaller is the value of the mass that it is sensitive to, assuming no backgrounds.

After 5 years of data taking, an effective Majorana mass of 200 meV corresponds to an half-life $T_{0\nu}^{1/2} = 2.85 \times 10^{25}$ years, resulting in around 150 expected $0\nu\beta\beta$-decay events in the FV. A smaller mass of 100 meV, in the same conditions, corresponds to an half-life $T_{0\nu}^{1/2} = 1.4 \times 10^{26}$ years, resulting in 37 expected events in the FV. These values were calculated using Equation 5.8 and using the IBM-2 NME value from Table 5.2.

The latest and more detailed SNO+ sensitivity studies resulted in a $m_{\beta\beta}$ range for the five years between 38 and 92 meV, using all the NMEs [62]. In the real conditions of the experiment, the small number of events associated with these small values of mass will only be possible to observe if the backgrounds are well known and reduced to a minimum. Besides, a very good energy resolution is also an important requirement, that is supported by Equation 1.23. The energy resolution and energy scale in the $0\nu\beta\beta$-decay peak region are affected by how well the optical properties of the detector are characterized. The following Sections will discuss the effects of

an imprecise optical calibration on the energy resolution and on the energy scale of the $0\nu\beta\beta$ energy spectrum, as well as the effects in the peak detection efficiency, that directly influences the estimates and uncertainty of the half-life.

5.2 $0\nu\beta\beta$-Decay Energy Spectrum Sensitivity to Optical Effects

The SNO+ detector is designed to measure the energy of the particles interacting inside the AV. The energy of monoenergetic particles or processes usually has the shape of a Gaussian-like peak due to fluctuations and uncertainties in the measurements. The width of the peak determines the capability to distinguish particles with different energies. Particles with energies closer than the energy resolution cannot be separated.

For instance, the ratio of counts due to $0\nu\beta\beta$ and due to $2\nu\beta\beta$ events in the peak region, $R_{0\nu/2\nu}$, is approximately [63]:

$$R_{0\nu/2\nu} \propto \left(\frac{Q_{\beta\beta}}{\Delta E}\right)^6 \frac{T_{2\nu}^{1/2}}{T_{0\nu}^{1/2}}\,, \tag{5.9}$$

where $Q_{\beta\beta}$ is the Q-value of the decay, ΔE is the energy resolution, and $T_{2\nu}^{1/2}$ and $T_{0\nu}^{1/2}$ are the half-lives of the two processes. This expression clearly indicates that a good energy resolution is crucial to overcome the background and to see a peak.

The energy resolution, ΔE is given by the full-width-at-half-maximum (FWHM) of the signal peak that, for a Gaussian distribution with standard deviation σ, is FWHM = 2.35σ.

The energy response of the detector depends on the optical properties such as the media attenuations and the PMT angular response. Thus they affect the energy resolution and the energy scale of the $0\nu\beta\beta$-decay. In this Section are presented the results of MC simulations of this process using scaled values of the scintillator attenuation and PMT angular responses. This intends to show how these two quantities, if not properly measured or accounted for in the physics analysis, affect the resolution and energy scale of the $0\nu\beta\beta$-decay signal.

5.2.1 PMT Angular Response Effects on the $0\nu\beta\beta$ Energy Spectrum

During the SNO experiment it was observed that, over a period of three years, the PMT angular response decreased by almost 2.5% at high incidence angles, for all measured wavelengths. This was due to the degradation of the reflectors around the PMT, caused by the ultra-pure water where they were immersed. More than 10 years passed since then, and the PMTs and reflectors have been inside ultra-pure water for at least three more years. It is then expected that their reflectors have degraded more and that the PMT angular response that is going to be measured in SNO+ has decreased.

If the current PMT angular response is not properly measured and accounted for to calibrate the detector, how will it affect the searches for the neutrinoless double beta decay?

To answer this question, Monte Carlo simulations of $0\nu\beta\beta$-decay events were performed using the PMT Grey Disc Model described in Section 3.2.2. One of the simulations used the default values of the PMT angular response, measured in SNO in 2006. Two others used scaled PMT angular responses to simulate aged and improved responses. In all of them, the same number of $0\nu\beta\beta$-decay events was generated randomly throughout the AV volume.

The scaling of the PMT angular responses was implemented by observing how the PMT angular responses changed with time in SNO. Looking at Figure 3.4 (b), it was observed that, at low incident angles, there was no difference between the PMT angular responses from 2003 and 2006, whereas at high incidence angles there were differences of around 2.5%. The decrease in the response with time showed an almost linear variation with the incident angle, as can be observed in Figure 5.4. Therefore, to scale the default PMT angular response in the SNO+ MC, two functions were defined to calculate the scaling factor for each incident angle:

$$f_- = 1 - 0.000714 \times \theta \quad [\theta \text{ in degrees}] \,, \tag{5.10}$$

$$f_+ = 1 + 0.000714 \times \theta \quad [\theta \text{ in degrees}] \,. \tag{5.11}$$

f_- was used to scale "down" the PMT angular response, in order to simulate an aged response. f_+ was used to scale "up" the default response and simulate an improved PMT angular response. Although it is not expected that the PMT response has improved, simulating the two situations allows to study the effects that an underestimated and overestimated angular response has on the final physics results.

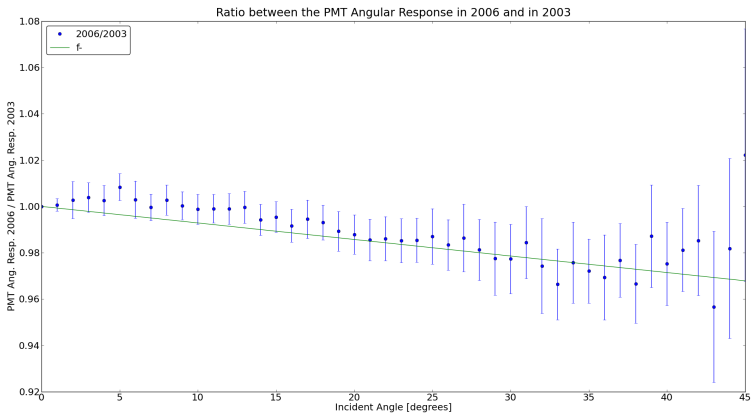

Figure 5.4: Ratio (in blue) of the PMT angular response measured in SNO in 2006 by the one measured in 2003. The ratio shows that, over the three years, there was a linear decrease in the PMT angular response with incident angle. The green line is the linear function, given by Equation 5.10, used to scale down the PMT angular responses for this study.

The reconstructed energy spectrum of the $0\nu\beta\beta$-decay was obtained from each simulation, using the fiducial volume cut of 20%. The spectra are compared in Figure 5.5: (a) compares the results using the aged PMT angular response with the ones using the default; (b) compares the results using the improved PMT angular response with the ones using the default. Both the results with the aged and improved parameters show a shift in the mean of the peak. Table 5.3 shows the values of the mean (E), energy resolution (ΔE) and relative energy resolution ($\Delta E/E$) of each peak, that were obtained by fitting them with a Gaussian function. Because both mean and energy resolution vary, the relative energy resolution is more suited to compare the three peaks. The relative energy resolutions of the simulations with the aged and improved PMT angular responses increased, but not substantially when comparing with the default results. As will be seen in Section 5.3, the most significant effect to the neutrinoless double beta decay searches is found to be the shift of the peak in energy.

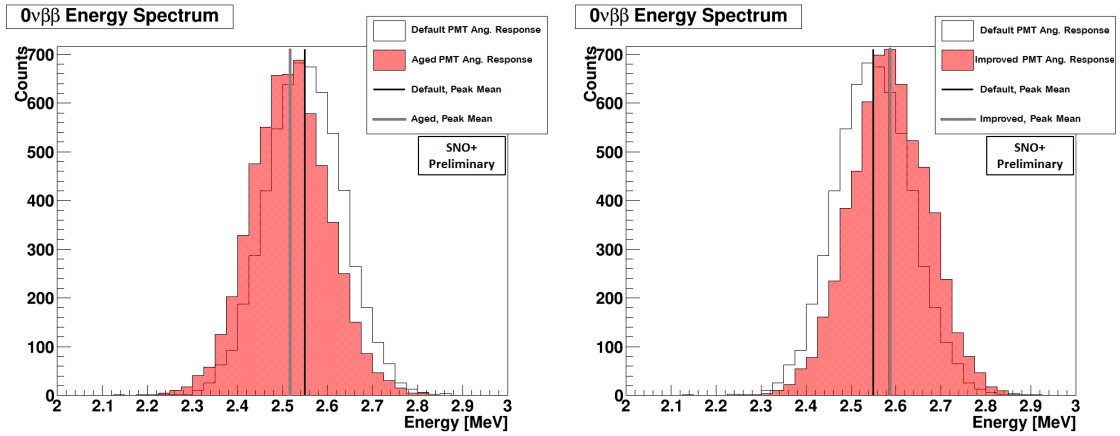

(a) (b)

Figure 5.5: $0\nu\beta\beta$ energy spectra from MC simulations using the default PMT angular response compared with (a) the energy spectrum from MC simulation with an aged PMT angular response and (b) an improved PMT angular response.

Table 5.3: Mean energy, energy resolution and relative energy resolution of the $0\nu\beta\beta$-decay energy spectra from the MC simulations with default and scaled PMT angular response parameters.

	Mean, E [MeV]	Energy Resolution, ΔE [MeV]	Relative Energy Resolution ($\Delta E/E$)
Default PMT Ang. Response	2.5487 ± 0.0007	0.198 ± 0.002	0.0777 ± 0.0008
Aged PMT Ang. Response	2.5155 ± 0.0008	0.197 ± 0.002	0.0783 ± 0.0008
Improved PMT Ang. Response	2.585 ± 0.001	0.202 ± 0.002	0.0781 ± 0.0008

5.2.2 Scintillator Attenuation Effects on the $0\nu\beta\beta$ Energy Spectrum

The detector media attenuation coefficients are a key optical parameter to describe the propagation of light. From the three media (water, acrylic and scintillator), the scintillator attenuation coefficients will be the most relevant for the $0\nu\beta\beta$-decay analysis because it is the medium where the events of interest will occur and, even taking into account the 20% FV, it is the medium where light will travel a greater distance. To understand how variations in the scintillator attenuation length affect the energy reconstruction mechanisms, several $0\nu\beta\beta$-decay MC simulations were performed with scaled attenuation lengths by a given percentage. Figures 5.6 (a) to (f) show the energy spectra obtained for scalings of 50%, 75%, 90%, 110%, 125% and 150%, respectively.

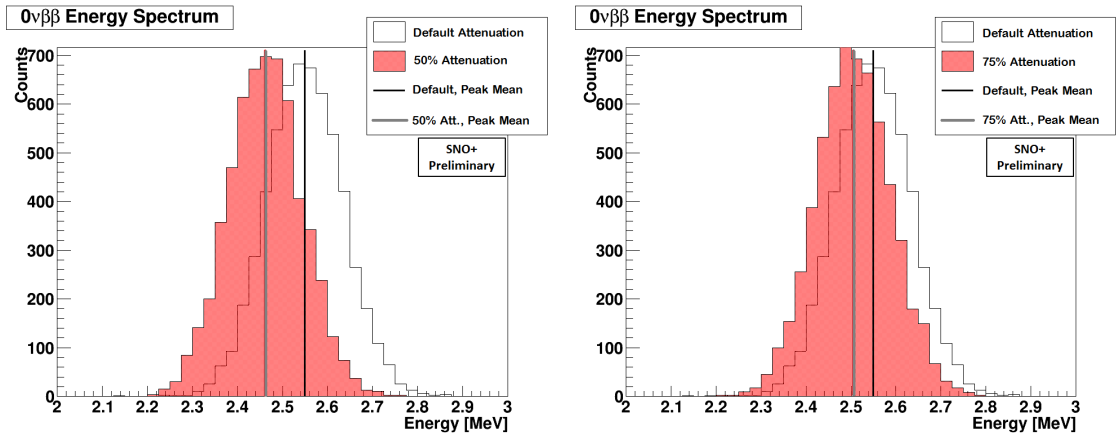

(a) (b)

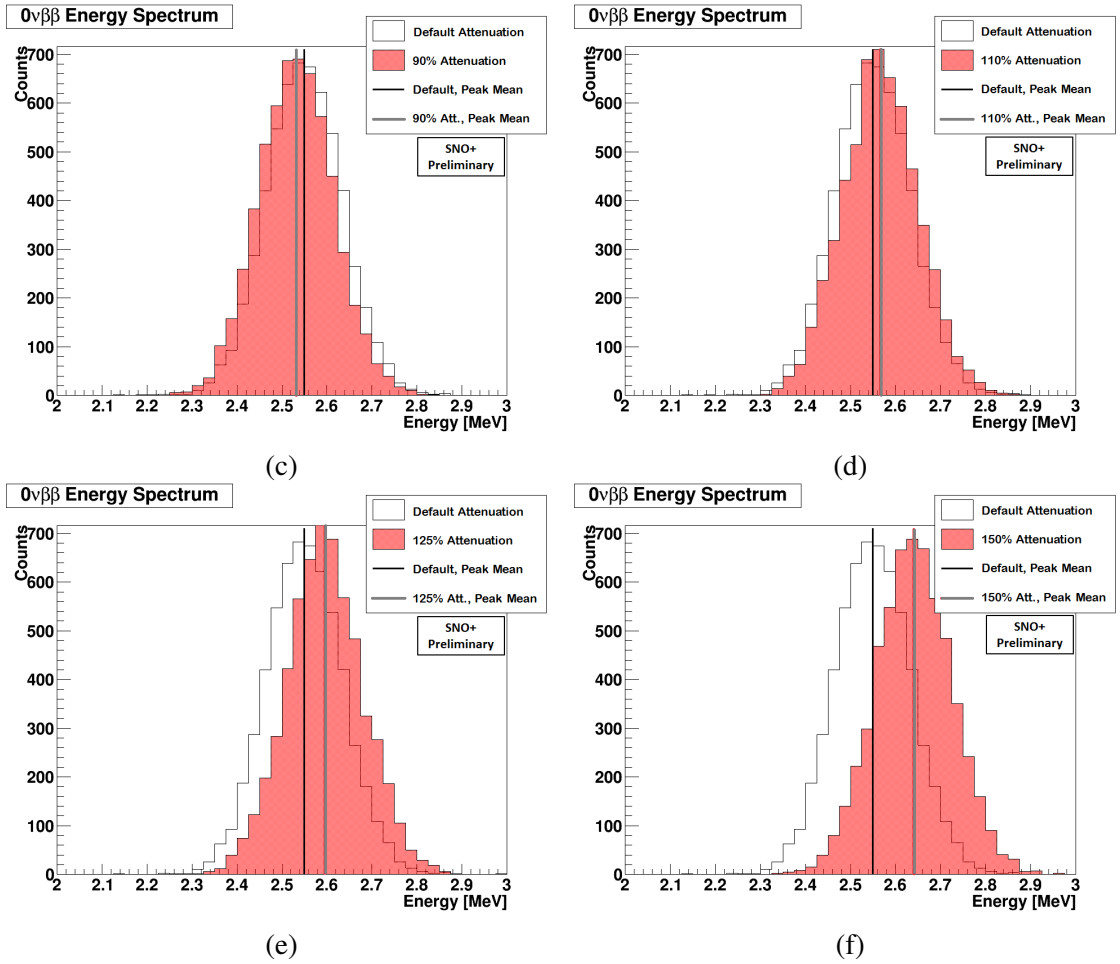

Figure 5.6: $0\nu\beta\beta$ energy spectra from MC simulations with scaled scintillator attenuation lengths (red), compared with the results from a MC simulation using the default attenuation lengths (black). The scaling percentages used were (a) 50%, (b) 75%, (c) 90%, (d) 110%, (e) 125% and (f) 150%.

The analysis reconstruction mechanisms are tuned using the parameters measured by the Optical Calibration. In this example, changes in the scintillator attenuation that are not taken into account during the reconstruction of the event will lead to a calculated energy that is different from the real. For instance, a smaller attenuation length, corresponding to a larger attenuation coefficient, means that more photons will be absorbed before reaching the PMTs. This results in a loss of information that leads to a smaller reconstructed energy, as can be observed in Figures 5.6 (a), (b) and (c). On the other hand, a larger attenuation length, corresponding to a smaller attenuation coefficient, will result in more photons reaching the PMTs, leading to a larger event energy calculated by the reconstruction mechanisms.

Table 5.4: Mean energy, energy resolution and relative energy resolution of the $0\nu\beta\beta$-decay energy spectra from the MC simulations with default and scaled scintillator attenuation lengths.

	Mean, E [MeV]	Energy Resolution, ΔE [MeV]	Relative Energy Resolution ($\Delta E/E$)
Default Attenuation	2.5487 ± 0.0007	0.198 ± 0.002	0.0777 ± 0.0008
50% Attenuation	2.4612 ± 0.0008	0.191 ± 0.002	0.0776 ± 0.0008
75% Attenuation	2.5045 ± 0.0007	0.194 ± 0.002	0.0775 ± 0.0008
90% Attenuation	2.5310 ± 0.0005	0.195 ± 0.001	0.0770 ± 0.0004
110% Attenuation	2.5661 ± 0.0009	0.200 ± 0.002	0.0779 ± 0.0008
125% Attenuation	2.593 ± 0.001	0.193 ± 0.002	0.0744 ± 0.0008
150% Attenuation	2.6402 ± 0.0009	0.198 ± 0.002	0.0750 ± 0.0008

Table 5.4 shows the values of the mean (E), energy resolution (ΔE) and relative energy resolution ($\Delta E/E$) of each peak, that were obtained by fitting them with a Gaussian. Although the shifts in energy are very clear, it can be observed that the changes in the attenuation of the scintillator do not affect considerably the energy resolution.

5.3 $0\nu\beta\beta$-Decay Half-life Sensitivity to Optical Effects

Assuming zero background conditions, the half-life of the ^{130}Te $0\nu\beta\beta$-decay can be calculated from the number of detected events inside the FV, *S*, in an energy window between 0.5σ to 1.5σ around the Gaussian signal peak, known as the Region of Interest (ROI) [35]:

$$S = \epsilon \cdot N_{130} \cdot ln2 \cdot \frac{t}{T_{0\nu}^{1/2}} \, , \tag{5.12}$$

where ϵ is the signal detection efficiency, N_{130} is the number of ^{130}Te atoms in the FV and *t* is the detector live time. Rewriting the expression in terms of $T_{0\nu}^{1/2}$:

$$T_{0\nu}^{1/2} = \epsilon \cdot N_{130} \cdot ln2 \cdot \frac{t}{S} \, . \tag{5.13}$$

The signal detection efficiency ϵ is determined by detailed MC simulations of the $0\nu\beta\beta$-decay peak, that require a precise knowledge of the detector geometry and materials, and that are tuned using the parameters coming from the Optical Calibration. It is the fraction of simulated events in the FV detected within the ROI window with respect to the total number of simulated events in the FV:

$$\epsilon = \frac{N_{ROI,FV}}{N_{total,FV}} \, . \tag{5.14}$$

The previous Sections showed that changes in the PMT angular responses and scintillator attenuation lead to shifts in the energy and resolution of the $0\nu\beta\beta$-decay signal. These shifts will then vary the number of events inside the ROI, changing the detection efficiency and affecting the determination of $T_{0\nu}^{1/2}$.

Using the results of the MC simulations with the default optical parameters, measured at the end of the SNO experiment in 2006, it was possible to define the ROI energy window. The energy spectrum peak was fitted with a Gaussian function, giving values for the mean μ = 2.5487 MeV and standard deviation σ = 0.084, resulting in:

$$\begin{aligned} \mu - 0.5\sigma < ROI < \mu + 1.5\sigma \, , \\ 2.5066 \text{ MeV} < ROI < 2.6751 \text{ MeV} \, . \end{aligned} \tag{5.15}$$

The signal detection efficiencies were then calculated using this energy window for the MC simulations with the default optical parameters and with the scaled PMT angular responses (aged and improved) and scintillator attenuations (50%, 75%, 90%, 110%, 125% and 150%). Figures 5.7, 5.8 and 5.9 show, respectively, the energy spectra and ROI limits (red lines) for the different simulations. Table 5.5 presents the obtained efficiencies for the simulations with default and scaled optical parameters. It is observed that the efficiency of the data with parameters scaled up (improved PMT response, 110% Attenuation, 125% Attenuation and 150% Attenuation) increases relative to the default, whereas the efficiency of the data with parameters scaled down decreases.

These changes in the efficiency are mostly due to the energy shift caused by an incorrect reconstruction of the energy of the events.

Table 5.5: $0\nu\beta\beta$ signal detection efficiencies ϵ, for a fixed ROI, from MC simulations with default and scaled optical parameters. $|\epsilon_{default} - \epsilon|$ is the deviation of the efficiency from MC data with the scaled parameters relative to the efficiency from the default MC data.

	ϵ	$\epsilon_{default} - \epsilon$	$(\epsilon_{default} - \epsilon)/\epsilon_{default}$
Default Optical Parameters	0.62 ± 0.01		
Improved PMT Angular Response	0.67 ± 0.01	-0.05 ± 0.02	-0.08 ± 0.03
Aged PMT Angular Response	0.52 ± 0.01	0.10 ± 0.02	0.16 ± 0.03
Attenuation 50%	0.28 ± 0.01	0.34 ± 0.02	0.55 ± 0.03
Attenuation 75%	0.47 ± 0.01	0.15 ± 0.02	0.24 ± 0.03
Attenuation 90%	0.57 ± 0.01	0.05 ± 0.02	0.08 ± 0.03
Attenuation 110%	0.66 ± 0.01	-0.04 ± 0.02	-0.06 ± 0.03
Attenuation 125%	0.69 ± 0.01	-0.07 ± 0.02	-0.11 ± 0.03
Attenuation 150%	0.60 ± 0.01	-0.02 ± 0.02	-0.03 ± 0.03

It can be observed that shifts in the optical parameters that are not accounted for by the energy reconstruction mechanisms lead to signal detection efficiencies that differ up to 55% from the default one. A larger efficiency will overestimate the value of the half-life, whereas a small efficiency will underestimate it. The difference between the default signal detection efficiency and the one obtained using the scaled optical parameters represents the accuracy of ϵ_{scaled}, and because it is different from zero it will result in a systematic error that will affect the uncertainty of the ^{130}Te $0\nu\beta\beta$ half-life.

The uncertainty of the half-life, $\sigma(T_{0\nu}^{1/2})$, propagates as follows:

$$\sigma(T_{0\nu}^{1/2}) = ln2\sqrt{|N_{130}\frac{t}{S}|^2\sigma^2(\epsilon) + |\epsilon\frac{t}{S}|^2\sigma^2(N_{130}) + |\epsilon N_{130}\frac{t}{S^2}|^2\sigma^2(S)}\,, \tag{5.16}$$

considering that there is no uncertainty in the determination of the detector live time. $\sigma(\epsilon)$ is the signal detection efficiency uncertainty, $\sigma(S) = \sqrt{S}$ is the uncertainty in the number of detected events within the ROI and $\sigma(N_{130})$ is the uncertainty in the number of ^{130}Te atoms. The latter is directly related to the uncertainty in defining the fiducial volume, V_F, because

$$\begin{aligned} N_{130} &= \frac{m(^{130}\text{Te in 20\% FV})}{m(^{130}\text{Te nucleus})} \\ &= \frac{m(^{130}\text{Te in the AV})}{m(^{130}\text{Te nucleus})}\frac{V_F}{V_{AV}}\,, \end{aligned} \tag{5.17}$$

assuming that there is no uncertainty in the values of the masses and of the AV volume, whose radius is 6 m. The uncertainty in V_F comes from the uncertainty in the reconstructed position from the fit:

$$V_F = \frac{4}{3}\pi|\vec{r}|^3\,, \tag{5.18}$$

$$\sigma(V_F) = 4\pi|\vec{r}|^2\sigma(\vec{r})\,. \tag{5.19}$$

Therefore,

$$\sigma(N_{130}) = \frac{m(^{130}\text{Te in the AV})}{m(^{130}\text{Te nucleus})}\frac{4\pi|\vec{r}|^2}{V_{AV}}\sigma(\vec{r})\,. \tag{5.20}$$

The weight that the systematic uncertainty of the signal detection efficiency has on the half-life uncertainty can be quantified with an hypothetical example: one can consider that after a live time of 5 years there are 30 $0\nu\beta\beta$ events detected within the ROI for a FV with *r* = 3.5 m, that correspond to $m_{\beta\beta} \approx 114$ meV, calculated with Equation 5.8 and using the IBM-2 NME value of Table 5.2. This example calculation will use the signal detection efficiency from the simulation with default parameters, $\epsilon = 0.62$, and the systematic uncertainty caused by the aged PMT angular response, $\sigma(\epsilon) = 0.10$. The uncertainty in the number of ^{130}Te atoms, in this example, will be calculated with Equation 5.20 using a position uncertainty of 5 cm and of 2 cm.

Table 5.6 shows the values of ϵ, N_{130} and S used in this example, along with their uncertainties (for N_{130}, the two uncertainties due to $\sigma(\vec{r})$ = 2 and 5 cm) and their contributions to the ^{130}Te $0\nu\beta\beta$-decay half-life uncertainty squared:

$$\sigma^2(T_{0\nu}^{1/2}) = A + B + C\,, \tag{5.21}$$

$$\begin{aligned} A &= ln^2 2\,|N_{130}\frac{t}{S}|^2\,\sigma^2(\epsilon) \\ B &= ln^2 2\,|\epsilon\frac{t}{S}|^2\,\sigma^2(N_{130}) \\ C &= ln^2 2\,|\epsilon N_{130}\frac{t}{S^2}\,|^2\sigma^2(S) \end{aligned} \tag{5.22}$$

Table 5.6: Signal Detection Efficiency, ϵ, number of ^{130}Te atoms in the FV volume, N_{130} and number of detected events in the ROI, *S*, used in the example described in the text, along with their uncertainties and their contributions to the ^{130}Te $0\nu\beta\beta$-decay half-life uncertainty squared, showed in Equations 5.21 and 5.22.

	Value	σ	Contribution to $\sigma^2(T_{0\nu}^{1/2})$ $\left[\times 10^{54}\text{years}^2\right]$
ϵ	0.62	0.10	A = 0.000198
N_{130}	1.216497×10^{27}	0.087×10^{27} ($\sigma(\vec{r})$ = 2 cm)	B = 0.000039
N_{130}	1.216497×10^{27}	0.22×10^{27} ($\sigma(\vec{r})$ = 5 cm)	B = 0.000248
S	30	$\sqrt{30}$	C = 0.000253

Looking at the values obtained, it can be concluded that the contributions to $\sigma^2(T_{0\nu}^{1/2})$ are of the same order of magnitude, except for the example with a position uncertainty of 2 cm, which is an order of magnitude smaller. It is observed that the term due to the statistical uncertainty, C, has the biggest contribution to $\sigma^2(T_{0\nu}^{1/2})$.

Using the values of this example, the calculated half-life and its total uncertainty is:

$$T_{0\nu}^{1/2} = 8.71 \times 10^{25}\text{ years } \pm \begin{cases} 2.21 \times 10^{25}\text{ years}, & \text{if } \sigma(\vec{r}) = 2\text{ cm} \\ 2.64 \times 10^{25}\text{ years}, & \text{if } \sigma(\vec{r}) = 5\text{ cm} \end{cases} \tag{5.23}$$

Table 5.7 shows the total half-life uncertainty, $\sigma(T_{0\nu}^{1/2})$, and the squared root of the different contributions to the total uncertainty expressed as a fraction of the calculated $T_{1/2}^{0\nu}$, for the cases of 2 cm and of 5 cm position uncertainty. In the case where $\sigma(\vec{r})$ = 2 cm, the total half-life uncertainty percentage is 25%, and that value has 16% contribution from the term concerning the signal detection efficiency uncertainty, 7% from the term concerning the position uncertainty and 18% from the statistical term of the number of detected events. For the case where $\sigma(\vec{r})$ = 5 cm, the total uncertainty increases to 30%, and the contribution from the term concerning the position uncertainty increases to 18%.

Table 5.7: Total half-life uncertainty and different contributions expressed as a fraction of the calculated $T_{0\nu}^{1/2}$, for the cases of 2 cm and of 5 cm position uncertainty.

	Case $\sigma(\vec{r})$ = 2 cm	Case $\sigma(\vec{r})$ = 5 cm
$\frac{\sigma(T_{0\nu}^{1/2})}{T_{0\nu}^{1/2}}$	0.25	0.30
$\frac{\sqrt{A}}{T_{0\nu}^{1/2}} = \frac{\sigma(\epsilon)}{\epsilon}$	0.16	0.16
$\frac{\sqrt{B}}{T_{0\nu}^{1/2}} = \frac{\sigma(N_{130})}{N_{130}}$	0.07	0.18
$\frac{\sqrt{C}}{T_{0\nu}^{1/2}} = \frac{\sigma(S)}{S}$	0.18	0.18

In this example, the statistical uncertainty and the signal detection efficiency systematic error due to the optics are very similar. Improving the value of the statistical uncertainty, *i.e.* reducing it, would require a much larger isotope mass and much more than 5 years of exposure. These conditions are difficult to achieve. However, the systematic error due to the optics can be reduced if a detailed Optical Calibration is performed. Assuming an extreme case where $\sigma(\epsilon) = 0$, the overall half-life uncertainty decreases by 23%, assuming a position uncertainty of 2 cm. This means that a good characterization of the detector optical response, in this example, can improve by up to 23% the half-life uncertainty.

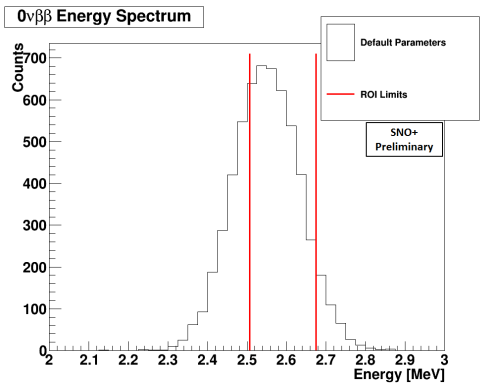

Figure 5.7: $0\nu\beta\beta$-decay energy spectrum from a MC simulation using the default optical parameters, obtained at the end of the SNO experiment in 2006. The red lines represent the ROI limits.

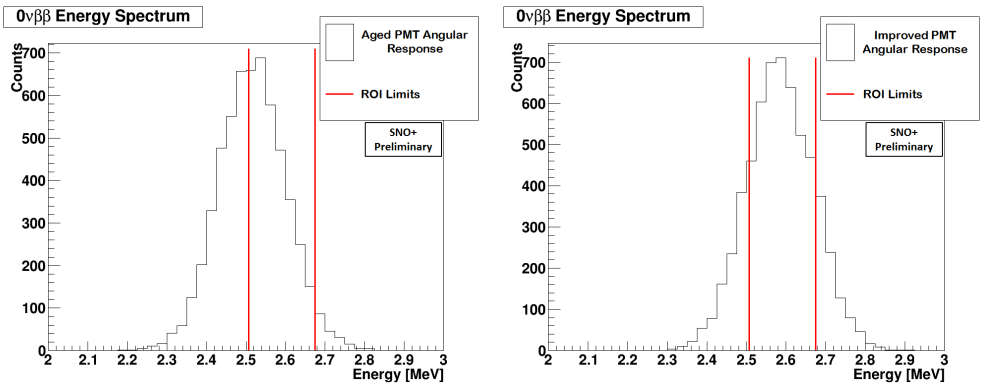

(a) (b)

Figure 5.8: $0\nu\beta\beta$-decay energy spectra from MC simulations using (a) aged and (b) improved PMT angular response parameters. The red lines represent the ROI limits.

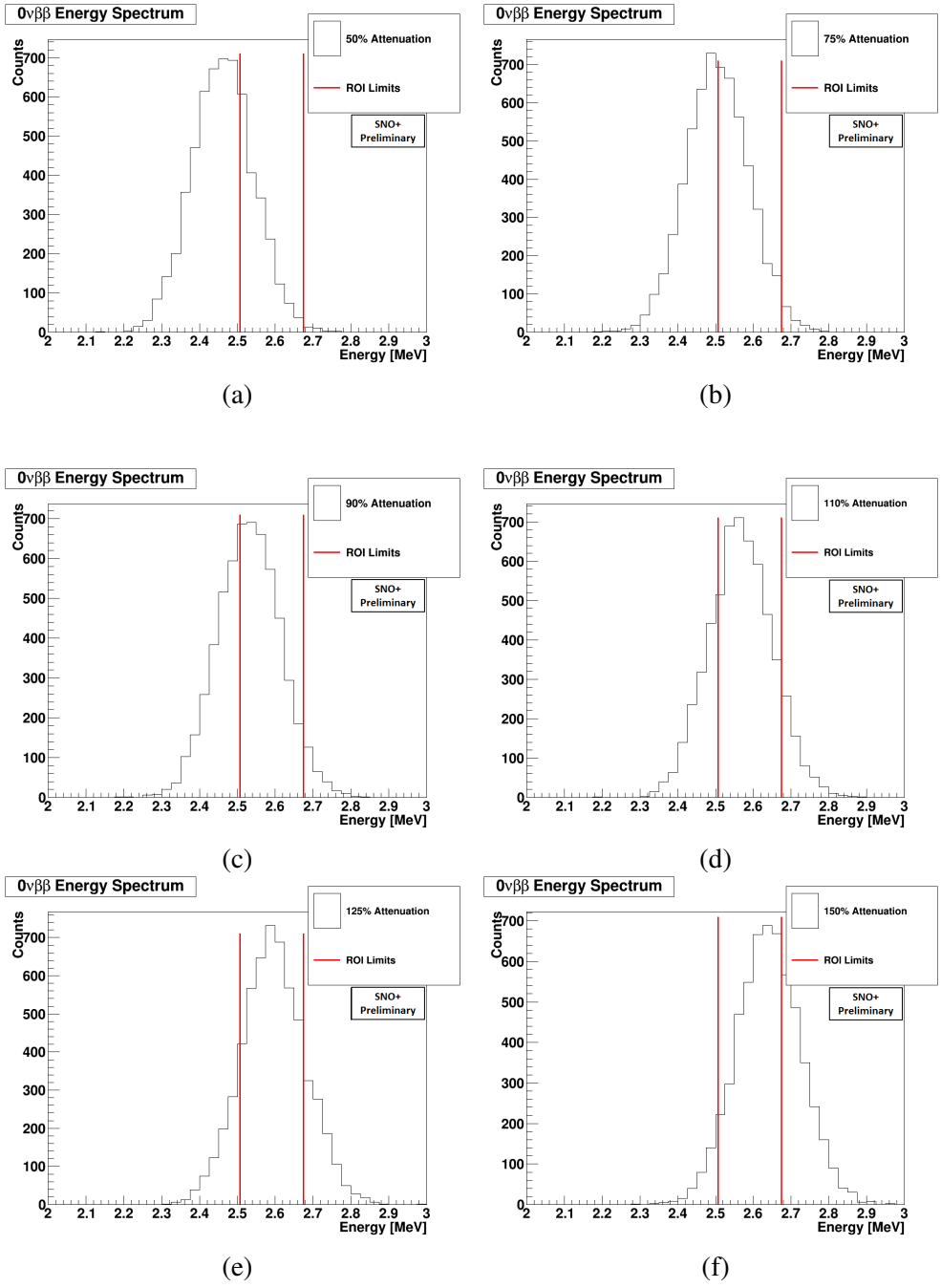

Figure 5.9: $0\nu\beta\beta$-decay energy spectra from MC simulations using attenuation lengths scaled by (a) 50%, (b) 75%, (c) 90%, (d) 110%, (e) 125% and (f) 150%. The red lines represent the ROI limits.

Quantifying the systematic uncertainty caused by the optical effects and comparing it with the statistical uncertainty is only possible for a given number of $0\nu\beta\beta$ events and, by consequence, a fixed value of $m_{\beta\beta}$. This study was performed considering 30 candidate $0\nu\beta\beta$-decay events, that correspond to $m_{\beta\beta} \approx 114$ meV. It is important to note that other values of $m_{\beta\beta}$ would affect differently the contributions to the overall half-life uncertainty.

This simplified study in "zero background" conditions shows, in a pessimistic perspective, how not performing an Optical Calibration of the SNO+ detector would affect the $0\nu\beta\beta$-decay half-life measurement and its uncertainty. Ideally, a full treatment including all the backgrounds is needed to truly understand how changes in the optics of the detector affect the $0\nu\beta\beta$-decay searches. The work in this thesis provides the foundation to perform more detailed studies in the

upcoming months.

Fortunately, the SNO+ experiment will count with detailed Optical Calibrations throughout its three phases, as well as Electronics, PMT and Energy Calibrations using other techniques. This will ensure an optimal quality of the physics results and aim for the best sensitivity to the $0\nu\beta\beta$-decay possible.

Chapter 6

Conclusions

This thesis describes the Optical Calibration of the SNO+ detector and the effects of the optics on the sensitivity for the search of the neutrinoless double beta decay of the isotope ^{130}Te. SNO+ reuses the detector of the SNO experiment (1999-2006) for neutrino physics studies, such as the detection of solar, reactor, supernova and geo neutrinos, as well as searches for exotic physics such as invisible nucleon decay modes. However, the main goal of the SNO+ experiment is the search for the neutrinoless double beta decay of ^{130}Te that, if observed, would prove the Majorana nature of neutrinos, allowing the measurement of their effective mass, and provide clues regarding the neutrino mass hierarchy problem. For that, SNO+ will count with a large mass of ^{130}Te, of the order of 1330 kg, with its ability for background discrimination and rejection, as well as an optimized energy resolution. This requires a complete and detailed detector calibration, including an Optical Calibration that is responsible to characterize the propagation and collection of light in the detector.

Events inside the detector create light that is detected by $\sim$9300 photomultiplier tubes (PMTs). The propagation of the photons will change during their path towards the PMTs: they will be scattered and attenuated over the distance travelled, refracted and reflected when crossing from one medium to the other, and their collection will be influenced by the solid angle of each PMT as well as their efficiency and angular response. To characterize all these effects, one of the sources used for the Optical Calibration is a near-isotropic light diffusing sphere called *laserball*. The relation between the amount of direct light detected by the PMTs and these optical effects is given by the Optical Model, which is a parametrized model that also accounts for the anisotropies in the light distribution of the laserball. The model parameters are obtained from laserball data, at different positions and wavelengths, by a statistical fit performed by the Optical Calibration Analysis (OCA) software.

The Water Phase of the SNO+ experiment is, at the time of the writing of this thesis, ongoing, and it will be followed by a Pure Scintillator Phase and the Te-loading Phase where the searches for the neutrinoless double beta decay will be performed. The current phase is crucial to perform a detailed Optical Calibration of the detector in order to measure the PMT angular responses and media attenuations. While there is not a full set of laserball data, Monte Carlo and SNO data have been used to test and validate the Optical Calibration Analysis software, as well as to create faster and less complex tools to check the quality of the laserball data and to validate the optical parameters obtained. That is the case of the Diagonal Scan Analysis, measuring the attenuation coefficients of the medium inside the acrylic vessel from runs with the laserball along one detector diagonal, and the Laserball Asymmetry Analysis, characterizing the angular distribution of the

laserball using runs with the laserball placed at the center with different orientations.

Through extensive tests with Monte Carlo data, the Diagonal Scan Analysis and the Laserball Asymmetry Analysis showed a good capability in reproducing the optical parameters used as input in the simulated data. The Diagonal Scan Analysis demonstrated an accuracy between 6 and 15%, at 420 nm, in extracting the attenuation coefficients. In the case of the Laserball Asymmetry Analysis, the good performance of this tool led to adapting OCA to receive the laserball angular distribution parameters as an input for the fit, reducing the overall parameter space and the time necessary to perform the full fit. Testing OCA with Monte Carlo data also showed its good performance in obtaining the input parameters of the simulated data. The extracted water attenuation coefficients differed from the simulation input by only 3%, at 420 nm. On the other hand, tests with SNO data validated the performance of the fit using real laserball data.

Since the beginning of the SNO+ Water Phase a few laserball runs have been acquired. The first laserball data is important for a number of checks: detector and laser stability, tune the laser and laserball settings (such as the intensity), create and test laserball data quality tools as well as test the software tools that prepare the laserball data to be used by OCA. So far, the data quality tools helped to identify problems with the laser hardware, providing useful feedback to the crew operating the laserball. Testing the software that processes the laserball data allowed to identify a possible bug in the laserball position fit algorithm, that will now be investigated and corrected. The ongoing work concerning the data quality and the software tests is crucial to identify other possible problems before there is a full set of Optical Calibration data.

The first SNO+ laserball runs also gave an insight of the shadowing inside the detector. A large number of PMTs is excluded from the OCA fit due to shadowing, $\sim 37\%$. With a simple study, it was shown that this percentage can be reduced to 22% by combining two runs for the occupancy normalisation, one with the laserball at the center of the AV and other at ($\pm$1400, 0, 0) mm.

The last part of this thesis focused on the effects that the optical parameters have on the energy reconstruction mechanisms and, consequently, on the sensitivity for the neutrinoless double beta decay searches. The motivation for these studies were the fact that the reflectors around the PMTs, used to increase the collection of light, have been degrading with time, resulting in a decrease of the PMT angular response, and the fact that the media attenuations, in particular the scintillator attenuation, may change with time. An important question arises from this: if these optical effects are not well characterized and monitored over time, what are their impact on the neutrinoless double beta decay searches?

To answer this question, neutrinoless double beta decay events were simulated using scaled PMT angular responses and scintillator attenuation lengths, as well as a control sample using the optical parameters that are used by default by the Monte Carlo simulations until the full Optical Calibration is performed. It was shown that the scaled optical parameters, that were not taken into account by the reconstruction mechanisms, induced shifts in the energy of the neutrinoless double beta decay peak. These shifts affect directly the signal detection efficiency, that is one of the weighting factors of the ^{130}Te neutrinoless double beta decay half-life calculation.

The peak shifts due to the optical parameters results in a systematic error for the signal detection efficiency that will propagate into the half-life uncertainty. The way the systematic error affects the overall uncertainty depends on how much statistics the measurement has. For the same detector exposure, the number of detected events highly depends on the $0\nu\beta\beta$ rate and, by consequence, the value of the effective Majorana neutrino mass. Using a simplified example, for an effective Majorana neutrino mass of 114 meV, it was shown that this systematic error can be of the

order of the statistical uncertainty. However, it can be reduced by performing a detailed Optical Calibration of the detector, improving the overall half-life uncertainty by up to $\sim$23%.

Given the above, the deployment of the laserball and the Optical Calibration are critical for the SNO+ experiment in order to ensure a good precision and sensitivity to accomplish the physics goals and to obtain competitive measurements and limits. Also, a repeated deployment of the laserball will allow a regular monitoring of the optical response of the detector, ensuring that the data collected over time is consistent with one another.

Appendix A

Laserball Orientation

When interpreting laserball data, it is useful to define the coordinate systems of the detector (Figure A.1) and of the laserball (Figure A.2). The detector coordinate system has its origin at the center of the AV, with the z-axis pointing in the vertical direction from the bottom of the cavity to the top. The xy plane points in the four PSUP cardinal directions[1]: North (+y), East (+x), South (-y) and West (-x).

The laserball coordinate system also has its z-axis defined in the vertical direction. The hardware slot, where the manipulator ropes are attached, defines the positive x axis. It is aligned with the detector coordinate system according to the following convention [65]:

- ϕ_{LB} = 0: detector East (+x);
- ϕ_{LB} = π/2: detector North (+y);
- ϕ_{LB} = $\pm\pi$: detector West (-x);
- ϕ_{LB} = -π/2: detector South (-y);

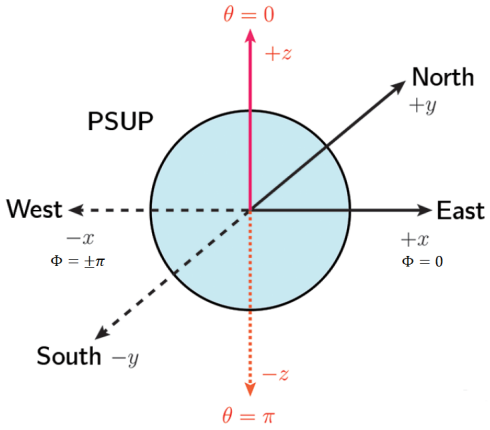

Figure A.1: PSUP coordinate system. [50]

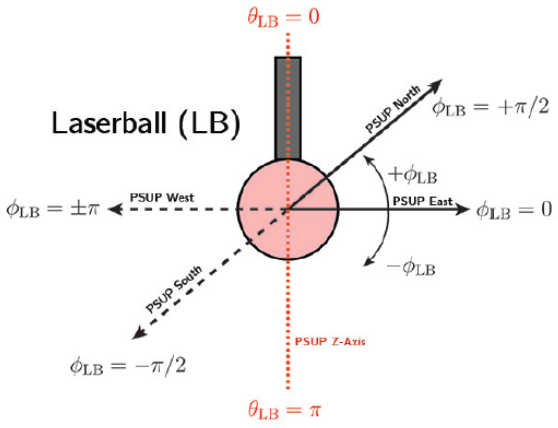

Figure A.2: Laserball coordinate system. [65]

Given the spherical symmetry shared by the PSUP and the laserball, observations in the PMTs hits at a given PMT position give information on the relative intensity of the laserball in (cosθ_{LB},ϕ_{LB}) $\equiv$(cosθ_{PMT},ϕ_{PMT}). The two sets of polar coordinates are coincident if the laserball is facing the East direction (aligned with the PSUP). When it is rotated, the angle ϕ_{LB} will no longer be coincident with ϕ_{PMT} and, in order to correctly interpret the data, it is important to

[1]The true North is -49.6° from the PSUP North. [64]

understand how they are related. In summary, the relations between ϕ_{LB} and ϕ_{PMT} for the four possible laserball orientations, illustrated in Figure A.3, are:

- LB facing East: $\phi^E_{LB} = \phi_{PMT}$
- LB facing North: $\phi^N_{LB} = \phi_{PMT} - \frac{\pi}{2}$
- LB facing West: $\phi^W_{LB} = \phi_{PMT} \pm \pi$
- LB facing South: $\phi^S_{LB} = \phi_{PMT} + \frac{\pi}{2}$

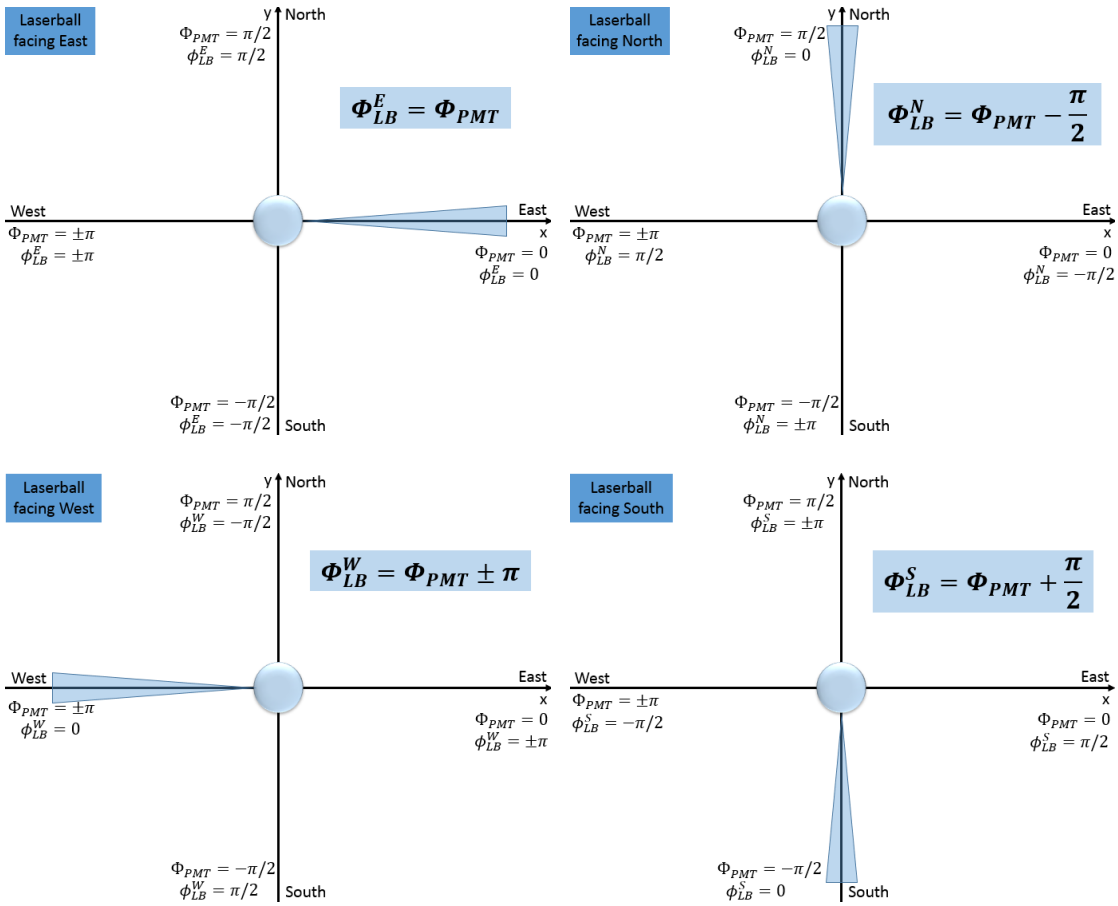

Figure A.3: Relation between the laserball ϕ_{LB} angle and the PMT ϕ_{PMT} angle for the four possible laserball orientations.

Appendix B

Laserball Asymmetry Analysis: Fitting the Results

Fitting the results of the Laserball Asymmetry Analysis allows to obtain the amplitudes A_k and phases δ_k of the laserball sinusoidal angular distribution model, $H_{sin}(cos\theta_{LB}, \phi_{LB})$, described in Section 3.2.3. For each slice of cos(θ), the ratio of occupancies from runs with opposite directions is going to be equal to the ratio of two sinusoidal functions with different ϕ angles, according to the orientation of the laserball:

$$\frac{N_k}{S_k} = \frac{f_N^k(\phi_{LB}^N)}{f_S^k(\phi_{LB}^S)} = \frac{1 + A_k\, sin(\phi_{LB}^N + \delta_k)}{1 + A_k\, sin(\phi_{LB}^S + \delta_k)}\,. \tag{B.1}$$

ϕ_{LB}^N and ϕ_{LB}^S can be expressed in terms of the fixed PMT coordinate system through the following relations:

$$\phi_{LB}^N = \phi_{PMT} - \pi/2\,, \tag{B.2}$$

$$\phi_{LB}^S = \phi_{PMT} + \pi/2\,, \tag{B.3}$$

illustrated and described in Appendix A.

Using these relations, the N/S ratio can be written as:

$$\begin{aligned} \frac{N_k}{S_k} &= \frac{1 + A_k\, sin(\phi_{PMT} - \pi/2 + \delta_k)}{1 + A_k\, sin(\phi_{PMT} + \pi/2 + \delta_k)} \\ &= \frac{1 - A_k\, cos(\phi_{PMT} + \delta_k)}{1 + A_k\, cos(\phi_{PMT} + \delta_k)} \\ &= \frac{2}{1 + A_k\, cos(\phi_{PMT} + \delta_k)} - 1\,. \end{aligned} \tag{B.4}$$

Analogously, for the ratio W/E:

$$\begin{aligned} \frac{W_k}{E_k} = \frac{f_W^k(\phi_{LB}^W)}{f_E^k(\phi_{LB}^E)} &= \frac{1 + A_k\, sin(\phi_{LB}^W + \delta_k)}{1 + A_k\, sin(\phi_{LB}^E + \delta_k)} \\ &= \frac{1 - A_k\, sin(\phi_{PMT} + \delta_k)}{1 + A_k\, sin(\phi_{PMT} + \delta_k)} \\ &= \frac{2}{1 + A_k\, sin(\phi_{PMT} + \delta_k)} - 1\,, \end{aligned} \tag{B.5}$$

with $\phi^W_{LB} = \phi_{PMT} \pm \pi$ and $\phi^E_{LB} = \phi_{PMT}$.

The final expressions of N_k/S_k and W_k/E_k were used to fit the corresponding ratios, for each k slice, and it was possible to obtain the sinusoidal model parameters from it, as shown by the example in Figure B.1.

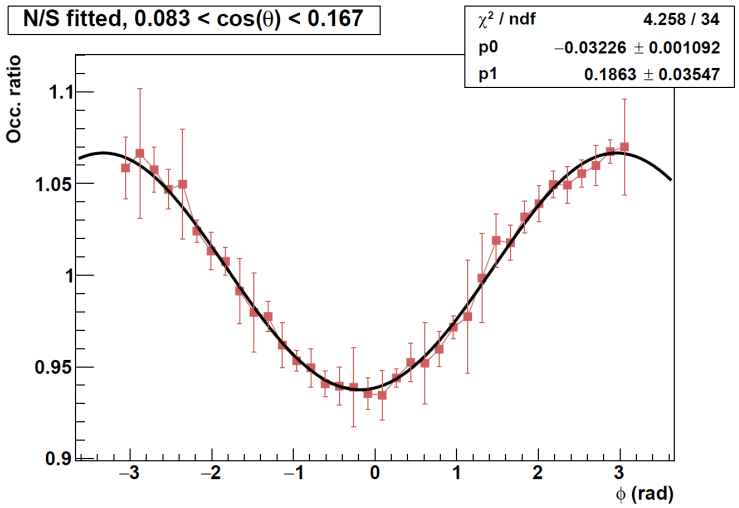

Figure B.1: Fit of the N/S ratio in function of ϕ.

The full set of results obtained for the amplitudes and the phases is shown in Figures B.2 and B.3, respectively.

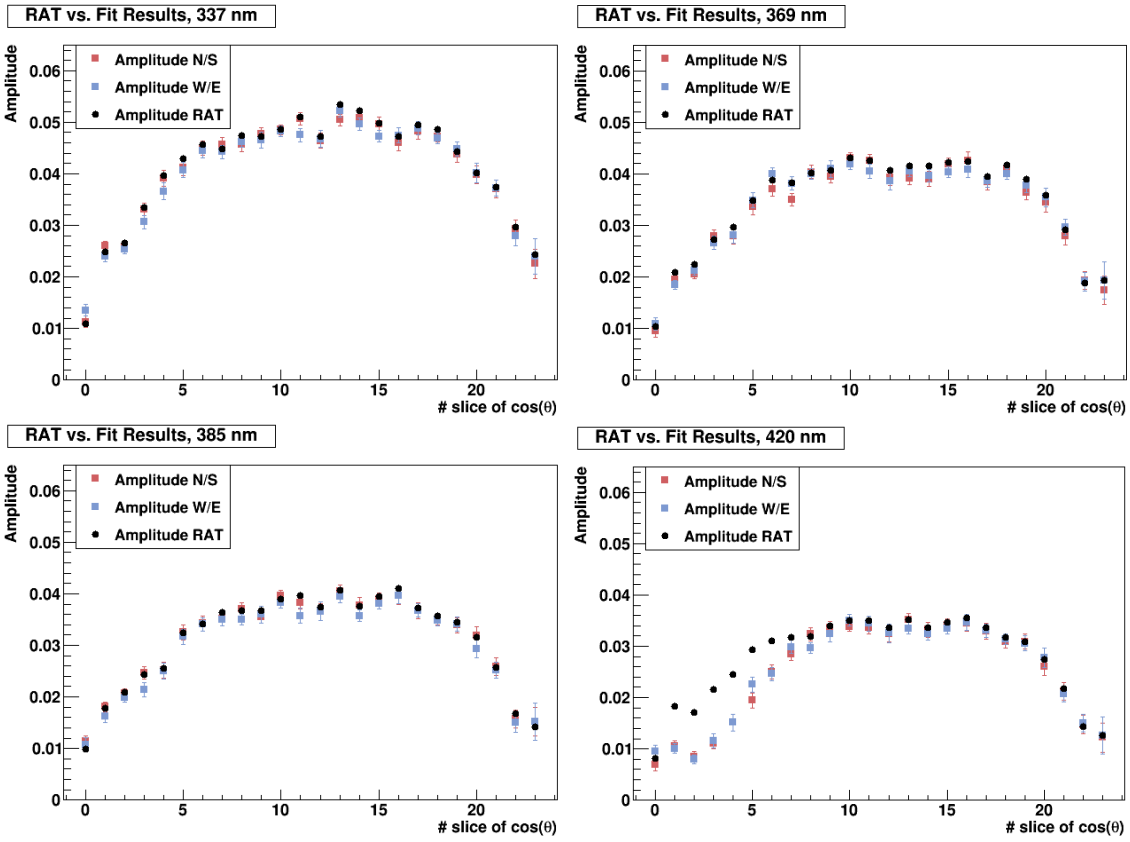

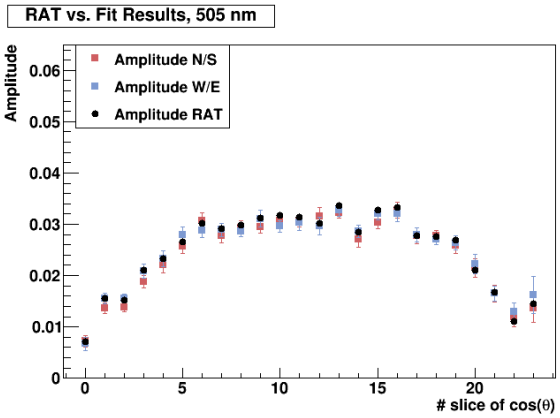

Figure B.2: Amplitudes from the N/S (red) and W/E (blue) ratios and from the simulation input (black) for each slice of cos(θ).

A good agreement between the amplitude results of the N/S (in red) and W/E (in blue) fits and the expected values (in black) can be observed in Figure B.2. Only the graph for the wavelength of 420 nm shows some discrepancies between the results obtained and the expected for the first seven slices of cos(θ). This issue will be further investigated once there is real calibration data. It is visible that the amplitude decreases with wavelength, meaning that for the wavelength of 505 nm the laserball will have a smaller azimuthal asymmetry than for the wavelength of 337 nm.

There is also a good agreement with respect to the phase parameters, in Figure B.3, between the results from the N/S fit (in red) and W/E fit (in blue) and the expected values (in black).

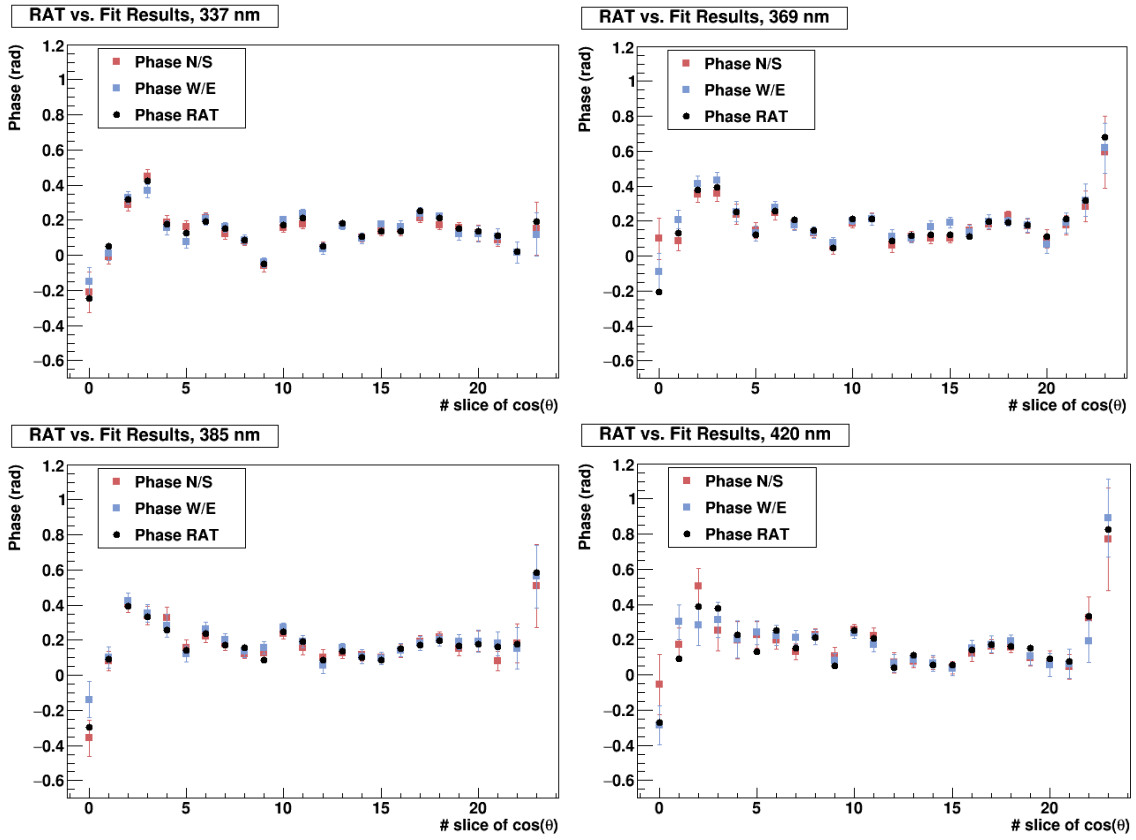

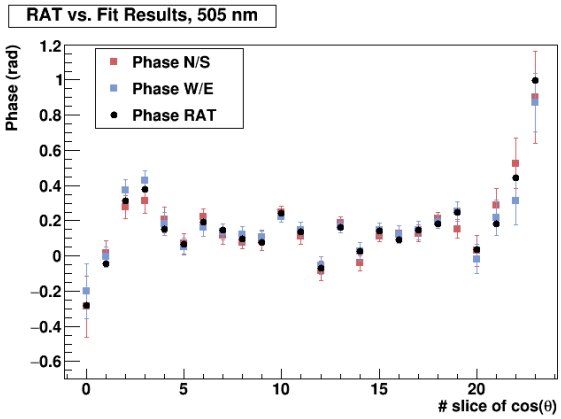

Figure B.3: Phases from the N/S (red) and W/E (blue) ratios and from the simulation input (black) for each slice of cos(θ).

Bibliography

[1] K.S. Krane. *Introductory Nuclear Physics*. John Wiley & Sons, 1987.

[2] W. Pauli. Open Letter to the Group of Radioactive People at the Gauverein meeting in Tubingen, Letter, December 1930.

[3] C. Cowan *et al.* Detection of the free neutrino: A Confirmation. *Science*, 124:103–104, 1956.

[4] Nobelprize.org. The Nobel Prize in Physics 1995. `http://www.nobelprize.org/nobel_prizes/physics/laureates/1995/`.

[5] R. Davis. A Review of the Homestake Solar Neutrino Experiment. *Progress in Particle and Nuclear Physics*, 32:13–32, 1994.

[6] Y. Fukuda *et al.* (Super-Kamiokande Collaboration). Evidence for oscillation of atmospheric neutrinos. *Physical Review Letters*, 81:1562–1567, 1998.

[7] Q. R. Ahmad *et al.* (SNO Collaboration). Measurement of the rate of $\nu_e + d \rightarrow p + p + e^-$ interactions produced by ^{8}B solar neutrinos at the Sudbury Neutrino Observatory. *Physical Review Letters*, 87:071301, 2001.

[8] B. Pontecorvo. Inverse Beta Processes and Nonconservation of Lepton Charge. *Journal of Experimental and Theoretical Physics (U.S.S.R.)*, 34:247–249, 1958.

[9] Z. Maki *et al.* Remarks on the Unified Model of Elementary Particles. *Progress of Theoretical Physics*, 28:870–880, 1962.

[10] S. Dell'Oro *et al.* Neutrinoless Double Beta Decay: 2015 Review. *Advances in High Energy Physics*, 2016, 2016.

[11] F. Capozzi *et al.* Global constraints on absolute neutrino masses and their ordering. *arXiv:1703.04471 [hep-ph]*, 2017.

[12] C. Patrignani *et al.* (Particle Data Group). The Review of Particle Physics. *Chinese Physics C*, 40, 2016.

[13] A. Gando *et al.* (KamLAND-Zen Collaboration). Search for Majorana Neutrinos near the Inverted Mass Hierarchy Region with KamLAND-Zen. *Physical Review Letters*, 117:082503, 2016.

[14] C. Kraus *et al.* (KATRIN Collaboration). Final results from phase II of the Mainz neutrino mass search in tritium beta decay. *The European Physical Journal C*, 40:447–468, 2005.

[15] C. Giunti and C. W. Kim. *Fundamentals of Neutrino Physics and Astrophysics*. Oxford University Press, 2007.

[16] E. Akhmedov. Majorana neutrinos and other Majorana particles: Theory and experiment. *arXiv:1412.3320 [hep-ph]*, 2014.

[17] S. Davidson *et al.* Leptogenesis. *Physics Reports*, 466:105–177, 2008.

[18] M. Goeppert-Mayer. Double Beta-Disintegration. *Physical Review*, 48:512, 1935.

[19] M. G. Inghram and J. H. Reynolds. Double Beta-Decay of ^{130}Te. *Physical Review*, 78:822, 1950.

[20] R. Arnold *et al.* (NEMO-3 Collaboration). Measurement of the double-beta decay half-life and search for the neutrinoless double-beta decay of ^{48}Ca with the NEMO-3 detector. *Physical Review D*, 93:112008, 2016.

[21] M. Agostini *et al.* (GERDA Collaboration). Results on $\beta\beta$ decay with emission of two neutrinos or Majorons in ^{76}Ge from GERDA Phase I. *The European Physical Journal C*, 75:416, 2015.

[22] Yu. M. Gavrilyuk *et al.* Indications of 2ν2K capture in ^{78}Kr. *Physical Review C*, 47:806, 1993.

[23] R. Arnold *et al.* (NEMO Collaboration). Limits on different Majoron decay modes of ^{100}Mo and ^{82}Se for neutrinoless double beta decays in the NEMO-3 experiment. *Nuclear Physics A*, 765:483–494, 2006.

[24] J. Argyriades *et al.* (NEMO Collaboration). Measurement of the two neutrino double beta decay half-life of Zr-96 with the NEMO-3 detector. *Nuclear Physics A*, 847:168–179, 2010.

[25] R. Arnold *et al.* (NEMO-3 Collaboration). Result of the search for neutrinoless double-β decay in ^{100}Mo with the NEMO-3 experiment. *Physical Review D*, 92:072011, 2015.

[26] R. Arnold *et al.* (NEMO-3 Collaboration). Measurement of the $2\nu\beta\beta$ Decay Half-Life and Search for the $0\nu\beta\beta$ Decay of ^{116}Cd with the NEMO-3 Detector. *Physical Review D*, 95:012007, 2017.

[27] T. Bernatowicz *et al.* Precise determination of relative and absolute $\beta\beta$-decay rates of ^{128}Te and ^{130}Te. *Physical Review C*, 47:806, 1993.

[28] C. Alduino *et al.* (CUORE Collaboration). Measurement of the Two-Neutrino Double Beta Decay Half-life of ^{130}Te with the CUORE-0 Experiment. *The European Physical Journal C*, 77:13, 2017.

[29] J. B. Albert *et al.* (EXO Collaboration). An improved measurement of the $2\nu\beta\beta$ half-life of Xe-136 with EXO-200. *Physical Review C*, 89:015502, 2014.

[30] R. Arnold *et al.* (NEMO-3 Collaboration). Measurement of the $2\nu\beta\beta$ decay half-life of ^{150}Nd and a search for $0\nu\beta\beta$ decay processes with the full exposure from the NEMO-3 detector. *Physical Review D*, 94:072003, 2016.

[31] A. L. Turkevich *et al.* Double-beta decay of ^{238}U. *Physical Review Letters*, 67:3211, 1991.

[32] M. Agostini *et al.* (GERDA Collaboration). Background free search for neutrinoless double beta decay with GERDA Phase II. *arXiv:1703.00570 [nucl-ex]*, 2017.

[33] C. Alduino *et al.* (CUORE Collaboration). Analysis Techniques for the Evaluation of the Neutrinoless Double-Beta Decay Lifetime in ^{130}Te with CUORE-0. *Physical Review C*, 93:045503, 2016.

[34] J. B. Albert *et al.* (EXO Collaboration). Search for Majorana neutrinos with the first two years of EXO-200 data. *Nature*, 510:229–234, 2014.

[35] S. Andringa *et al.* (SNO+ Collaboration). Current Status and Future Prospects of the SNO+ Experiment. *Advances in High Energy Physics*, 2016, 2016.

[36] E. W. Beier. NewNd $0\nu\beta\beta$ counting experiment. SNO Internal Note.

[37] S. Biller. Probing Majorana neutrinos in the regime of the normal mass hierarchy. *Physical Review D*, 87:071301, 2013.

[38] A.M. Bakalyarov *et al.* Results of the experiment on investigation of Germanium-76 double beta decay. Experimental data of Heidelberg–Moscow collaboration November 1995 – August 2001. *Physics of Particles and Nuclei Letters*, 2:77–81, 2005.

[39] C. Macolino *et al.* (GERDA Collaboration). Results on neutrinoless double beta decay from GERDA Phase I. *Modern Physics Letters A*, 29:1430001, 2014.

[40] C.E. Aalseth *et al.* (The IGEX Collaboration). The IGEX ^{76}Ge Neutrinoless Double-Beta Decay Experiment: Prospects for Next Generation Experiments. *Physical Review D*, 65:092007, 2002.

[41] S.N. Ahmed *et al.* (SNO Collaboration). Constraints on Nucleon Decay via "Invisible" Modes from the Sudbury Neutrino Observatory. *Physical Review Letters*, 92:102004, 2004.

[42] A.M. Serenelli *et al.* Solar Models with Accretion. I. Application to the Solar Abundance Problem. *The Astrophysical Journal*, 743(1), 2011.

[43] W. C. Haxton and A. M. Serenelli. CN Cycle Solar Neutrinos and the Sun's Primordial Core Metallicity. *The Astrophysical Journal*, 687:678–691, 2008.

[44] B. Aharmim *et al.* (SNO Collaboration). Measurement of the Cosmic Ray and Neutrino-Induced Muon Flux at the Sudbury Neutrino Observatory. *Physical Review D*, 80:012001, 2009.

[45] B. Aharmim *et al.* (SNO Collaboration). The Sudbury Neutrino Observatory. *Nuclear Instruments and Methods in Physics Research A*, 449(1–2):172–207, 2000.

[46] B.A. Moffat. *The Optical Calibration of the Sudbury Neutrino Observatory*. PhD Thesis, Queen's University, 2001.

[47] C. Jackson. Photographs of aged concentrators, 2016. SNO+ Document 3518-v1.

[48] B.A. Moffat *et al.* Optical calibration hardware for the Sudbury Neutrino Observatory. *Nuclear Instruments and Methods in Physics Research A*, 554:255–265, 2005.

[49] R. Alves *et al.* The calibration system for the photomultiplier array of the SNO+ experiment. *Journal of Instrumentation (JINST)*, 10(3):P03002, 2015.

[50] R. Stainforth. *Characterising the Optical Response of the SNO+ Detector*. PhD Thesis, Department of High Energy Particle Physics of the Faculty of Sciences and Engineering of the University of Liverpool, 2016.

[51] N. Barros. *Precision Measurement of Neutrino Oscillation Parameters: Combined Three-Phase Results of the Sudbury Neutrino Observatory*. PhD Thesis, Department of Physics of the Faculty of Sciences of the University of Lisbon, 2011.

[52] M. Kerker. *The Scattering of Light and Other Electromagnetic Radiation*. Acabemic Press, New York, 1969.

[53] O. Simard. A New Laserball Model for the Optics in the NCD Phase. SNO Internal Note.

[54] W. H. Press *et al. Numerical Recipes in C: The Art of Scientific Computing, Second Edition*. Cambridge University Press, 1992.

[55] H. O'Keeffe. Temperature dependent measurement of the density of LAB, 2009. SNO+ Internal Note 276-v1.

[56] S. Stoica and M. Mirea. New Calculations for Phase Space Factors Involved in Double Beta Decay. *Physical Review C*, 88:037303, 2013.

[57] J. Barea *et al.* Nuclear matrix elements for double-β decay. *Physical Review C*, 87:014315, 2013.

[58] J. Menéndez *et al.* Disassembling the Nuclear Matrix Elements of the Neutrinoless double beta Decay. *Nuclear Physics A*, 818:139–151, 2009.

[59] J. Hyvärinen and J. Suhonen. Nuclear matrix elements for $0\nu\beta\beta$ decays with light or heavy Majorana-neutrino exchange. *Physical Review C*, 91:024613, 2015.

[60] P. K. Rath *et al.* Neutrinoless $\beta\beta$ decay transition matrix elements within mechanisms involving light Majorana neutrinos, classical Majorons and sterile neutrinos. *Physical Review C*, 88:064322, 2013.

[61] T. R. Rodriguéz and G. Martinez-Pinedo. Energy density functional study of nuclear matrix elements for neutrinoless $\beta\beta$ decay. *Physical Review Letters*, 105:252503, 2010.

[62] T. Kaptanoglu. Te Diol 0.5% Loading Approved BB Sensitivity Plots and Documentation. SNO+ Internal Note.

[63] S. R. Elliott and P. Vogel. Double Beta Decay. *Annual Review of Nuclear and Particle Science*, 52:115–151, 2002.

[64] P. Jones. RAT SNO+ Geometry, 2014. SNO+ Internal Note 2192-v4.

[65] J. Maneira *et al.* SNO+ Standard for the Laserball angular coordinates. SNO+ Internal Note 3141-v1.